Small protonated molecular clusters of astrophysical interest

Denis Comte

THESE de DOCTORAT de

opérée en cotutelle entre
l'Université Claude Bernard Lyon 1
et l'University of Innsbruck

Ecole Doctorale N° 52
ED Physique et Astrophysique PHAST

Discipline : Physique

Soutenue publiquement le 03/11/2022, par :
Denis COMTE

Small protonated molecular clusters of astrophysical interest

---

Devant le jury composé de :

ASCENZI, Daniela	Associate Professor	University of Trento	Examinatrice
DANIEL, Isabelle	Professeure des Universités	Université Lyon 1	Présidente du jury
ECHT, Olof	Professor Emeritus	University of New Hampshire	Rapporteur
FARIZON, Michel	Professeur des Universités	Université Lyon 1	Directeur de thèse
GOBET, Franck	Professeur des Universités	Université de Bordeaux	Rapporteur
MÄRK, Tilmann D.	University Professor	University of Innsbruck	Directeur de thèse

Ph.D. thesis

under cotutelle agreement between
the Université Claude Bernard Lyon 1
and the University of Innsbruck

Submitted in partial fulfilment of the requirements for the degree of
Doctor of Philosophy
in
Physics

Publicly defended the 03/11/2022, by:
Denis COMTE

Small protonated molecular clusters of astrophysical interest

---

In front of the jury composed of:

ASCENZI, Daniela	Associate Professor	University of Trento	Examiner
DANIEL, Isabelle	Professeure des Universités	Université Lyon 1	Jury president
ECHT, Olof	Professor Emeritus	University of New Hampshire	External referee
FARIZON, Michel	Professeur des Universités	Université Lyon 1	Supervisor
GOBET, Franck	Professeur des Universités	Université de Bordeaux	External referee
MÄRK, Tilmann D.	University Professor	University of Innsbruck	Supervisor

Remerciements

Acknowledgement

Avant toute chose, je souhaite remercier mes superviseurs Michel Farizon, pour m'avoir transmis sa vision de la science et pour son soutien bienveillant, et Tilmann D. Märk, pour sa constante gentillesse et son aide toujours aussi précieuse.

First of all, I would like to thank my supervisors Michel Farizon, for having passed on to me his vision of science and for his benevolent support, and Tilmann D. Märk, for his constant kindness and his ever so precious help.

Je remercie également tout particulièrement Bernadette Farizon pour son aide sans faille, qui a permis la réalisation de ce travail dans une atmosphère sereine au sein du groupe Interaction Particule Matière.

I also particularly thank Bernadette Farizon for her unfailing help, which allowed the realization of this work in a serene atmosphere within the Particle Matter Interaction group.

Je remercie sincèrement Isabelle Daniel pour avoir accepté de présider ce jury de thèse. Je remercie également mes deux rapporteurs Olof Echt et Franck Gobet pour leurs remarques et leurs rapports. Je remercie aussi chaleureusement Daniela Ascenzi pour avoir accepté de faire partie de mon jury de thèse.

I sincerely thank Isabelle Daniel for having accepted to be president of this thesis jury. I also thank my two external referees Olof Echt and Franck Gobet for their remarks and their reports. I also warmly thank Daniela Ascenzi for having accepted to be part of my thesis jury.

Je tiens à remercier mes deux universités, l'université Claude Bernard Lyon 1 et l'université d'Innsbruck. Je remercie la présidence de l'université Claude Bernard Lyon 1 ainsi que l'ensemble des services administratifs, et particulièrement les différentes composantes du LabEx LIO. Je remercie chaleureusement Tilmann D. Märk en sa qualité de recteur de l'université d'Innsbruck, ainsi que les services administratifs de l'université d'Innsbruck pour leur gentillesse et leur compréhension.

I would like to thank my two universities, the Université Claude Bernard Lyon 1 and the University of Innsbruck. I thank the presidency of the Université Claude Bernard Lyon 1 as well as all the administrative services, and particularly the various components of the LabEx LIO. I warmly thank Tilmann D. Märk as rector of the University of Innsbruck, as well as the administrative services of the University of Innsbruck for their kindness and their understanding.

J'adresse aussi un remerciement particulier à Paul Scheier qui m'a accueilli, lors de ma visite à Innsbruck, dans son équipe de recherche, au sein de l'Institute for Ion Physics and Applied Physics de l'Université d'Innsbruck.

I would also like to thank Paul Scheier who welcomed me, during my visit to Innsbruck, in his research team at the Institute for Ion Physics and Applied Physics of the University of Innsbruck.

Je remercie chaleureusement Raphaël Fillol pour son aide sur DIAM, ses précieux conseils et sa joie de vivre. Je remercie également Peter Calabria pour sa gentillesse et son expertise qui ont accompagnés ce travail durant ces trois années, ainsi que Pascal Gauthier, Rodople Della Negra et Roger Genre. Je remercie plus largement tout le personnel de l'Institut de Physique des 2 Infinis de Lyon et notamment sa directrice, Anne Ealet. Je remercie sincèrement Corinne Augier et Jean-Michel Benoît pour m'avoir donné l'opportunité d'enseigner.

Je remercie sincèrement mes collègues, et pas moins amis, Paul, Laura et Hector, pour leur aide et leur sympathie. Je remercie toutes les personnes qui sont passés en stage par le groupe IPM et ont participé à ce travail : Louis, Zakaria, Louis, Maxime, Maxence, Quentin et Christophe. J'adresse aussi un remerciement amical et sincère à Linda Feketeová et Thibaud Salbaing.

Ces trois années n'auraient pas été les mêmes sans mon collègue de bureau, et ami, qui a rendu ce travail encore plus stimulant et qui a permis de décompresser quand cela était nécessaire ; Léo, merci ! Je remercie aussi Jean-Baptiste, Lucrezia et Philippe pour tous les moments qu'on a passé ensemble, au travail ou en dehors. Un merci tout particulier à Elisa pour sa présence et sa gentillesse.

Je remercie Clotilde, pour tout ! Je remercie aussi tous mes amis et toutes les personnes avec qui j'ai partagé des moments de joie au cours de ces trois années, particulièrement : Pierre, Maxence, Marco, Paul, Kévin, Corentin, Jimmy, Pauline et Bérengère.

Je remercie enfin mes parents pour m'avoir accompagné et aidé durant ces 28 dernières années. Je remercie ma famille et plus particulièrement ma grand-mère, Adèle, mais aussi : Caroline, Elisa, Ginette, Joëlle, Laurent, Nicolas, Odile, Patricia, René, Sylvie, et Natale.

Résumé

Les observations de molécules complexes dans des environnements très différents de l'espace, depuis les régions de formation d'étoiles aux comètes, interrogent quant aux mécanismes qui ont conduit à leur formation. L'utilisation combinée du dispositif d'irradiation d'agrégats moléculaires de Lyon et de plusieurs méthodes théoriques permet l'étude statistique des mécanismes de relaxation de dimères moléculaires protonés suite à une excitation sur un temps court (femtoseconde) d'une des deux molécules de l'agrégat. Lors d'une collision unique à haute vitesse avec un atome, l'agrégat est placé dans une situation très éloignée de l'équilibre thermique et plusieurs mécanismes de relaxation sont observés. Les mesures des rapports de branchement et celles de la distribution d'énergie cinétique libérée pour un canal de relaxation donné permettent une étude quantitative de la compétition entre l'évaporation d'une molécule, la fragmentation d'une des deux molécules, et la formation d'une molécule plus complexe. Les résultats sont comparés pour différents dimères moléculaires protonés : le dimère de pyridine, le dimère de méthanol, le dimère de glycine et un dimère mixte composé d'un dipeptide de glycine et d'une molécule de glycine. A la différence du dimère de pyridine, les résultats obtenus avec le dimère de méthanol mettent en évidence la réaction unimoléculaire d'élimination de l'eau par l'agrégat parent. Les caractéristiques énergétiques de l'état fondamental du dimère, des produits de réaction, et des états de transitions ont été calculées avec la théorie de la fonctionnelle de la densité et utilisées pour comparer quantitativement les résultats expérimentaux à ceux de la théorie de l'espace de phase. Cela montre, d'une part, que les mesures expérimentales contraignent quantitativement les modèles théoriques et, d'autre part, que les résultats expérimentaux ne peuvent être interprétés quantitativement avec l'hypothèse d'une redistribution complète de l'énergie interne sur tous les modes de l'agrégat parent avant la dissociation. Cela souligne l'importance du temps de transfert d'énergie entre les molécules dans la compétition entre les différents canaux de relaxation. Dans le cas de la glycine, la formation du dipeptide et l'allongement de la chaîne peptidique ont été mis en évidence dans une réaction unimoléculaire. La mesure de la distribution de vitesse de la molécule d'eau éliminée par la réaction de polymérisation montre la présence de différents chemins de réaction pour lesquels le rôle du proton a été exploré par des calculs de théorie de la fonctionnelle de la densité. L'ensemble des résultats mettent en évidence la réaction unimoléculaire comme une nouvelle voie abiotique pour la formation de molécules organiques en phase gazeuse, soulignant l'intérêt des dimères moléculaires protonés pour la formation de molécules complexes en conditions astrophysiques.

Abstract

Observations of complex molecules in very different environments in space, from star-forming regions to comets, raise questions about the mechanisms that led to their formation. The combined use of the Lyon molecular cluster irradiation device and several theoretical methods allows the statistical study of the relaxation mechanisms of protonated molecular dimers following a short time (femtosecond) excitation of one of the two molecules in the cluster. During a single collision at high-velocity with an atom, the cluster is placed in a situation far from thermal equilibrium and several relaxation mechanisms are observed. Measurements of the branching ratios and of the kinetic energy released distribution for a given relaxation channel allow a quantitative study of the competition between the evaporation of a molecule, the fragmentation of one of the two molecules, and the formation of a more complex molecule. The results are compared for different molecular protonated dimers: the pyridine dimer, the methanol dimer, the glycine dimer, and a mixed dimer composed of a glycine dipeptide and a glycine molecule. In contrast to the pyridine dimer, the results obtained with the methanol dimer show the unimolecular reaction with water elimination by the parent cluster. The energy characteristics of the dimer ground state, reaction products, and transition states were calculated with density functional theory and used to compare quantitatively the experimental results with those from phase space theory. This shows, on the one hand, that the experimental measurements quantitatively constrain the theoretical models and, on the other hand, that the experimental results cannot be quantitatively interpreted with the assumption of a complete redistribution of the internal energy over all modes of the parent cluster before dissociation. This highlights the importance of the energy-transfer time between molecules on the competition between the different relaxation channels. In the case of glycine, the formation of the dipeptide and the elongation of the peptide chain were demonstrated in a unimolecular reaction. The measurement of the velocity distribution of the water molecule eliminated by the polymerisation reaction shows the presence of different reaction paths for which the role of the proton has been explored by density functional theory calculations. All the results highlight the unimolecular reaction as a new abiotic pathway for the formation of organic molecules in the gas phase, underlining the interest of protonated molecular dimers for the formation of complex molecules under astrophysical conditions.

Introduction

The formation of complex molecules in space is a contemporary question prompted by the number of increasingly detailed observations that show the presence of these molecules in a wide variety of environments: from star-forming regions to meteorites. The abundance of hydrogen in star-forming regions may be of significant importance in the formation mechanisms of organic molecules. Indeed, the attachment of proton on this type of molecules facilitates the formation of very small clusters, which themselves can be a crucible for the reactivity between molecules. The dynamics of these small molecular clusters has both quantum and statistical aspects. The competition between the different ways of redistributing energy in these molecular nanosystems can promote reactivity between molecules and thus contribute to the formation of complex molecules under abiotic conditions.

The several clusters studied with DIAM (*Dispositif d'Irradiation d'Agrégats Moléculaires*), since its implementation, correspond to a specific sample of molecules. The choice of the molecules introduced in the source is led by several issues: the fundamental aspects associated with the characteristics of the molecules in terms of binding or reactivity, but also the importance of these molecular systems in the context of societal issues associated with the environment or the origin of life. Based on all the previous results obtained with protonated molecular clusters — water, methanol, mixed pyridine-water, methanol-water clusters — the introduction of glycine in the source highlights several aspects. The molecule itself is more complex than methanol, while remaining a relatively simple linear molecule compared to the ring structure of pyridine for example. From another point of view, the study of the reaction of formation of a peptide chain from amino acids under abiotic conditions is of relevant interest.

DIAM allows to study the post-collisional relaxation of energy- and mass-selected small protonated molecular clusters. A single high-velocity collision allows quantitative observation of the consequences of energy redistribution in small clusters and multiple dissociation channels are observed. The COINTOF VMI (COrrelated Ion and Neutral Time Of Flight, Velocity Map Imaging) method allows the measurement of branching ratios between different dissociation channels and the measurement of the velocity distribution of the neutral fragment produced in a given dissociation channel. Experimental results on the evaporation of a molecule from the cluster can be compared with statistical molecular dynamics results. The competition between several relaxation channels is studied with Monte-Carlo simulations based on Phase Space Theory results. The experimental results, obtained with the protonated methanol dimer, show the evaporation of a methanol molecule and the formation of a dimethyl ether molecule via the elimination of a water molecule. The Density Functional Theory allows the study of the reactants, the products of the reaction, and also the search for possible transition states in the reaction

paths. The statistical model based on the results of the Phase Space Theory is used to quantitatively relate the experimental results to those obtained by the Density Functional Theory.

The observation of the water elimination reaction in the protonated methanol dimer led to the study of post-collisional relaxation in pure glycine clusters $H^+(Gly)_2$ and mixed glycine clusters $H^+Gly_2(Gly)$. Comparison of the results with those obtained with methanol led to the survey of several mechanisms for the observed unimolecular reactions: the formation of the glycine dipeptide in the protonated glycine dimer and the elongation of the peptide chain in the mixed protonated dipeptide and glycine dimer.

This manuscript consists of three chapters. The first chapter is devoted to the current scientific context on the observation of complex molecules in the universe. The second chapter presents the experimental and theoretical methods used. The results obtained in the experiments carried out on DIAM and the links of the experimental results with the theoretical results are presented in the third chapter.

Table of contents

Chapter I

Molecular complexity in astrophysical context

1. Molecules in space

The number of molecules detected in space, currently more than 270 [1], is growing rapidly thanks to the technological development of astrophysical observation. This contributes to the understanding of the formation of the universe. The overall view of the evolution of the universe is based on the standard model. 13.8 billion years ago, 10^{-43} seconds after the Big Bang, the universe starts expanding and undergoes the phase transition that breaks the original symmetry. At this point, gravity is released and governs the formation of stars, galaxies, and other large structures. At the same time, the electronuclear interaction appears and subjugates the particles. At 10^{-36} seconds after the Big Bang, the strong interaction separates in its turn. The primordial particles split into quarks and electrons. At one hundred billionth of a second, the weak nuclear force separates from the electromagnetic interaction. At the first hundred thousandth of a second, protons and neutrons are formed and three minutes after the Big Bang, the formation of the first atomic nuclei begins. All visible matter in the cosmos dates back to this time.

Thus, after about 380,000 years, collisions between protons and neutrons lead to the formation of the isotopes of hydrogen, helium, and to a lesser extent lithium. Capturing electrons, helium atoms are formed first, at which time there is decoupling between matter and radiation. The universe becomes transparent to photons which can travel to us. The very first molecule of significant abundance is the helium hydride ion HeH^+. Predicted for decades, HeH^+ has been observed for the first time in 2019 [2], in the planetary nebula NGC 7027, which is part of the Cygnus constellation where high temperatures and energies take place reminding of the early universe.

Astrochemistry takes into account the fundamental properties of molecules, in order to understand particularly how long molecules can remain intact and why some chemical species are more common than others. Models of chemical reactions indicate that the formation of HeH^+ favours the formation of H_2^+, followed by the formation of the neutral atomic hydrogen H, and the dihydrogen H_2 allowing the whole chemical tree to unfold. Then comes H_3^+, which generates CH^+, which generates CH_2^+ and a cascade of other molecules. Finally, this chain led to water H_2O, methanol CH_3OH, and more complex species. Astrochemistry aims to clarify which molecules are present in space, how they form and what their evolution means for observational and theoretical astrophysics. Many of the known astromolecules, including water H_2O, ammonia NH_3, or formaldehyde CH_2O, are common on Earth. Others are clearly different: molecules containing so-called inert noble gases such as ArH^+ and HeH^+, or hydrochloric acid with an extra proton $HClH^+$, for example. Space presents environments very alien to Earth with temperatures, pressures, and available ingredients very different from those we are used to. Therefore, we can find molecules challenging for the conventional notions of how atoms interact. A crucial issue is

the formation of the building blocks of life in the planets of our solar system that led to the appearance of living systems [3]. In the question of the origins of life on Earth, two assumptions currently dominate: life has an exogenous origin and it was meteorites and comets that brought to Earth the materials that formed the first cells, or it has a terrestrial origin where amino acids were formed from a primitive "chemical soup" [4]. The Earth's crust and hydrothermal environments [5] [6] may also provide the ideal conditions and all the necessary ingredients for prebiotic organic chemistry.

In this work we study two particular molecules, methanol CH_3OH, the smallest alcohol, and glycine NH_2CH_2COOH, the smallest amino acid. Two glycine molecules can form a dipeptide by eliminating a water molecule and creating a peptide bond. The formation of peptide bonds is a key element for the formation of the building blocks of life. In a similar way with two methanol molecules, an elimination reaction of a water molecule leading to the formation of dimethyl ether.

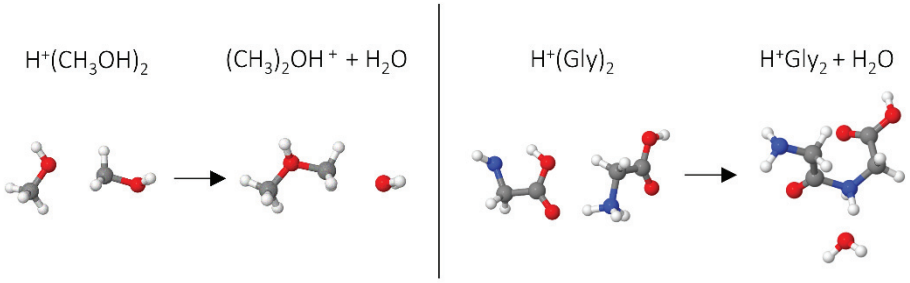

Figure 1: Left: formation of dimethyl ether from two methanol molecules. Right: two glycine molecules can form a dipeptide by removing a water molecule and creating a peptide bond.

From an observational point of view, methanol is observed in varying abundance in various regions of space. The observation of glycine is the subject of numerous studies. In the article, titled "Aspects of Astrophysically Observed Extraterrestrial Methanol, Hydrocarbon Derivatives, and Ions", Olah and co-workers wrote [7]:

> *"The relationship between extraterrestrially observed molecules and ions with our hydrocarbon chemistry raised interest whether studied terrestrial chemistry could also offer insight into the formation and the persistence of the large interstellar clouds of methanol. Astronomers, in 1995, have discovered a cloud (named Sagittarius B2 cloud) of methanol spanning around a stellar nursery in our Milky Way Galaxy. The very large cloud (288 billion miles wide) was calculated to hold more than 10 trillion trillions (10^{25}) tons of methanol! Numerous other methanol clouds have also been since observed, always close to nascent young stars [4-8]. Formation of extraterrestrial*

hydrocarbons, derivatives and their ions must have taken place under abiological conditions as until now no extraterrestrial biological life is observed outside our planet earth."

Differently from the methanol, glycine has been observed so far in the comets, most notably in 67P/Churyumov-Gerasimenko and in its environment.

Spectroscopy is the main source of information to signal the presence of molecules in different regions of space. A spectrum recorded in the corresponding frequency range will contain the rotational and ro-vibrational spectral characteristics of the molecules at the source of the emitted radiation. The spectra shown in Figure 2 measured recently with the ALMA ("Atacama Large Millimeter Array") telescopes are an example.

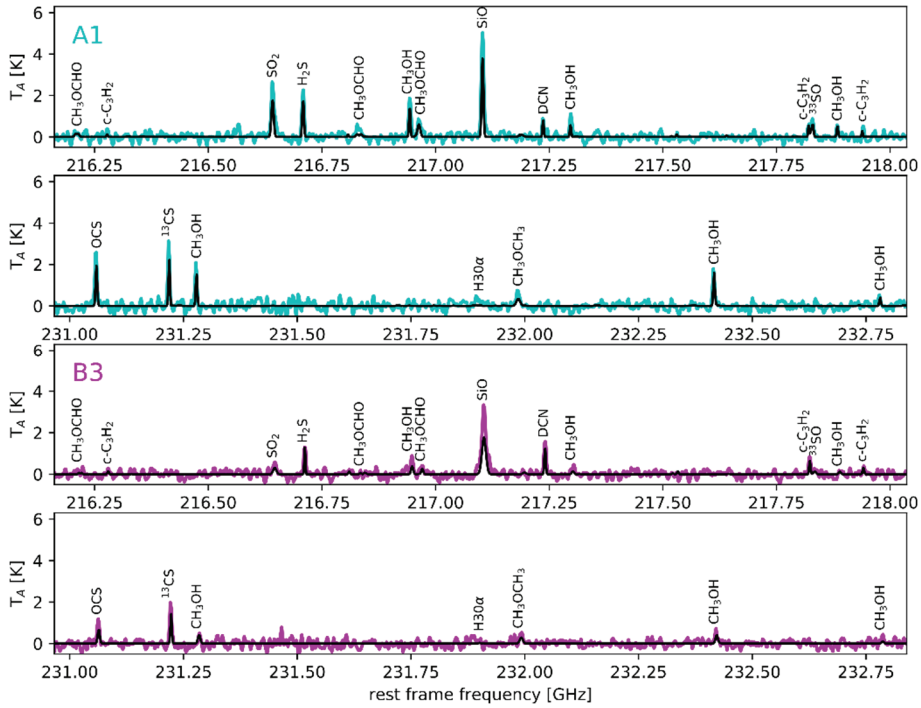

Figure 2: Spectra of the radiation measured by ALMA from the two hot cores (A1 and B3) located in the LHA 120-N 113 star-forming region. The four panels show the brightness temperature T_A, in Kelvin, as a function of the frequency in the rest frame of reference ν, in gigahertz. The top two panels contain the spectra associated with A1 (cyan curves) and the bottom two panels contain the spectra associated with B3 (purple curves). The black lines represent the synthetic spectra. The peaks are associated with the different molecular species identified. From M. Sewilo *et al.*, "The detection of Hot Cores and Complex Organic Molecules in the Large Magellanic Cloud", *ApJ*, vol. 853, p. 5, 2018 [8].

These spectra correspond to the observation of two young extragalactic stars [8]. They are located in the star-forming region LHA 120-N 113 (abbreviated N113), which is close to our galaxy (50 kpc) and located in the Large Magellanic Cloud. Young stars or protostellar systems — future high-mass stars for hot cores or low-mass stars for hot corinos [9] — are compact ($D < 0.1$ pc), hot ($T_{kin} > 100$ K), and dense ($n_H > 10^{6\text{-}7}$ cm^{-3}) sources [10] where ice mantles have been recently removed from dust grains, either by evaporation or sputtering in shock waves. For

each of the two hot cores, A1 and B3, two spectra are presented corresponding to the frequency ranges 216-218 GHz and 231-233 GHz. The y-axis of Figure 2 of the ALMA frequency spectra correspond to the brightness temperature, which is derived from the intensity measured at that frequency by the telescope. The line identification is performed with a software providing theoretical synthetic spectra (plotted in black in Figure 2) of the different molecules under conditions of local thermodynamic equilibrium (LTE), using databases of molecular lines and taking into account the individual opacity of each line. For the two hot cores studied, the spectra reveal the presence of methanol CH_3OH and dimethyl ether CH_3OCH_3. The presence of methyl formate CH_3OCHO and sulfur-bearing molecules (sulfur dioxide SO_2, hydrogen sulphide H_2S, carbonyl sulphide OCS, carbon monosulfide ^{13}CS, sulfur monoxide ^{33}SO) are also observed. Note the presence of cyclopropenylidene c-C_3H_2, which is a highly reactive organic radical classified as carbene. The deuterated form of hydrogen cyanide DCN is also observed. Methanol and dimethyl ether have also been observed in other star-forming regions. In our galaxy, the PEACHES ("PErseus ALMA CHEmistry Survey") project using ALMA has shown the presence of methanol in 56% of the protostellar systems located in the Perseus molecular clouds, and dimethyl ether is also observed [11].

To our knowledge, the detection of glycine, the simplest amino acid, has not yet been confirmed via spectroscopic observations. ALMA observations have allowed the detection of nitrogen-bearing molecules,for example, in the hot core G10.47+0.03 located in our galaxy. This hot core contains methanol and dimethyl ether [12]. Furthermore, for the same hot core, Mana and Pal [13] reported the presence of amino acetonitrile NH_2CH_2CN, a precursor of glycine and Gorai *et al.* [14] detected the presence of isocyanic acid HNCO, formamide NH_2CHO and methyl isocyanate CH_3NCO, three molecules that contain the same atoms as glycine NH_2CH_2COOH.

Methanol and nitrogen-bearing molecules are also observed in hot corinos associated with low-mass star formation. ALMA observations have also made it possible to study the molecular composition of the SVS13-A protostellar system, which corresponds to a binary system of two hot corinos (VLA4A and VLA4B) located in the Milky Way. Bianchi *et al.* detected the presence of methanol and dimethyl ether in both components of this binary system [15]. Bianchi *et al.* also observed the presence of a molecule containing an amine function, in this case formamide NH_2CHO, in both components of SVS13-A.

The GUAPOS ("G31 Unbiased ALMA sPectral Observational Survey") project aims to study the relative abundance of different complex molecules containing a nitrogen atom (nitrogen-bearing molecules). Figure 3 below presents the molecular abundances observed in different objects located in our galaxy [16]: the hot corino IRAS 16293 B which has a mass close to that of the Sun, the hot core G31, the hot core G10.47, two hot cores which are located in the Sagittarius B2 cloud, Sgr B2(N2), Sgr B2(N5), the protostellar system G328.2551, and the cloud

G+0693. G328.2551 is a binary system of two colliding hot cores, in which three measurements are considered, in the two components (A) and (B) of the binary system and in the surrounding envelope (env). G+0693 is a dense molecular cloud close to the center of our galaxy, which is distinguished from diffuse or translucent clouds [17]. G+0693 is a starless core, there is no star embryos but the density allows the formation of molecular hydrogen and complex molecules.

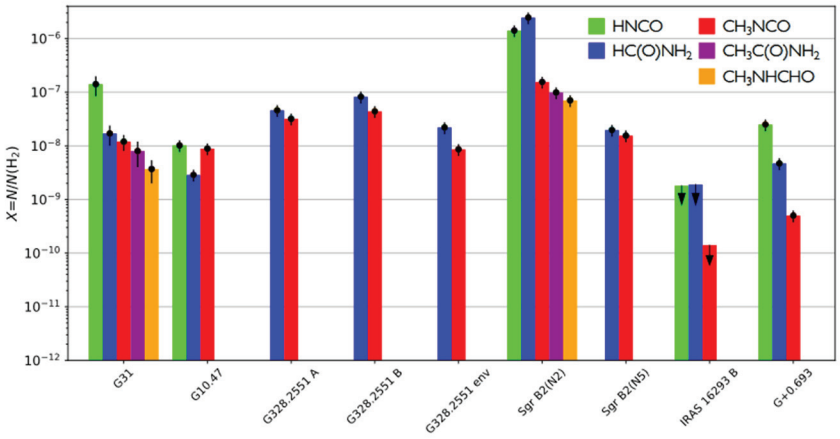

Figure 3: Abundances of different nitrogen-bearing molecules, identified by colour, observed in hot cores, hot corinos, and a dense molecular cloud. Abundances are given relative to that of molecular hydrogen H_2. From L. Colzi *et al.*, "The GUAPOS project II. A comprehensive study of peptide-like bond molecules", *ApJ*, vol. 653, p. 16, 2018 [16].

The hot cores G31 and Sgr B2(N2) have a similar molecular composition. In these two sources, five organic molecules are detected, isocyanic acid HNCO, formamide $HC(O)NH_2$, methyl isocyanate CH_3NCO, acetamide $CH_3C(O)NH_2$, and N-Methylformamide CH_3NHCHO. The relative abundances between the detected molecules are close, except for formamide which shows the highest abundance in the hot core Sgr B2(N2). Differently, only two molecules, methyl isocyanate CH_3NCO and formamide $HC(O)NH_2$, are observed in the hot core Sgr B2(N5) and in the binary system of two colliding hot cores G328.2551. The abundances are similar, the formamide abundance being always higher. Note that in the binary system, the abundances are of the same order of magnitude for both nuclei and their surroundings. In the dense molecular cloud G+0.693, isocyanic acid HNCO is observed, in addition to methyl isocyanate and formamide. This group of three molecules is also observed in the hot core G10.47 and in the hot corino IRAS 16293 B. Furthermore, the starless core TMC-1 (Taurus Molecular Cloud 1) is another example where a wide variety of complex molecules is observed, notably methanol CH_3OH [18] and dimethyl ether CH_3OCH_3 [19]. Such observations indicate that complex organic species can already be formed at the beginning of the starless core evolutionary phase.

Comets are small celestial objects orbiting a star and consisting of an icy nucleus and dust. Their relative proximity and the recent technological advances allow for different and complementary in-situ measurements of spectroscopy. The pioneering Giotto mission around

comet 1P/Halley has paved the way for the detection of complex molecules around comets [20]. The PICCA ("Positive Ion Cluster Composition Analyser") mass spectrometer, on board the Giotto probe, allows the analysis of positively charged ions [20]. It is designed to measure the abundance of ions in the 10 to 200 amu range along the flight path of the Giotto spacecraft. Using the relatively high speed of the probe and the fact that the ions are mainly monocharged due to the low temperature in the comet tail, the energy over charge ratio can be directly related to the mass distribution of the ions. The presence of several positively charged ions such as the hydronium ion H_3O^+ and the carbon monoxide ion CO^+ has been demonstrated around comet 1P/Halley [21]. Measurements also show the presence of higher mass positive ions (at least 100 amu) [20]. Furthermore, the Stardust mission found glycine in samples returned to Earth after a flyby of comet 81P/Wild 2 [22]. More recently, the Rosetta mission allowed a detailed in-situ study of the molecular composition of the comet 67P/Churyumov-Gerasimenko (abbreviated 67P) [23]. In particular, the mass spectrometer ROSINA ("Rosetta Orbiter Spectrometer for Ion and Neutral Analysis"), on board the Rosetta spacecraft, has detected the presence of glycine originating from the dust and water ice particles around the comet, but also directly from the comet nucleus [24] [25]. The ROSINA measurements also revealed the presence of several other complex molecules such as acetonitrile CH_3CN, ethylamine C_2H_7N and acetone C_3H_6O [23]. As in the case of star-forming regions, CHO-containing molecules have been detected, such as methanol CH_3OH, ethanol CH_3CH_2OH or dimethyl ether CH_3OCH_3 [23]. The presence of molecules with N, S, P, or Cl atoms is also observed [23] [26].

Meteorites are extraterrestrial objects, which impact the Earth after passing through the Earth's atmosphere. One of the best known is the Murchison meteorite, a chondrite classified as CM2.5 [27], which fell on Earth in 1969. Meteorites can be analysed by a variety of analytical techniques. The original material is extraterrestrial of origin, but it may be contaminated and modified by the passage through the Earth's atmosphere and the impact conditions on Earth. Numerous studies have been presented on the Murchison meteorite, highlighting the great molecular diversity of the chondrite [28] [29]. In particular, Engel and Nagy [28] detected the presence of amino acids in the Murchison meteorite such as glycine Gly, alanine Ala, and glutamic acid Glu. In 1970, Kvenvolden *et al.* also reported the presence of amino acids in the Murchison meteorite [30]. Many other chondrites have been studied, such as the GRA 95229 meteorite, which shows a great molecular complexity [31]. Cyclic molecules are also observed in meteorites and pyridine C_5H_5N, for example, has been observed in several of them [32]. Recently, Oba and colleagues identified the presence of purine and pyrimidine nucleobases in carbonaceous meteorites [33]. Figure 4 shows the comparison of the abundances of the main functional groups observed in the two meteorites, Murchison and GRA 95229 [31]. The same molecular species are observed but with very different abundances.

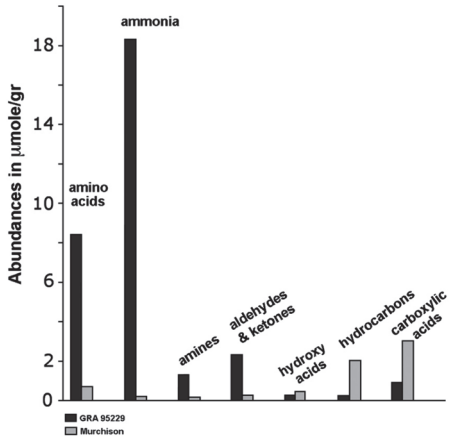

Figure 4: Abundances of the main groups of soluble compounds observed in the Murchison meteorite (black) and in the GRA 95229 meteorite (grey). Abundances are given in µmol.g^{-1}. From S. Pizzarello *et al.*, "Abundant ammonia in primitive asteroids and the case for a possible exobiology", *PNAS*, vol. 108, p. 4303, 2011 [31].

Relatively accessible to in-situ observation, the planets of the solar system, their moons, and their atmospheres also present a wide field of investigation. Mars is the object of many challenges. Indeed, the Curiosity rover deployed on Mars in 2012 has made many discoveries. The SAM ("Sample Analysis at Mars") instrument [34], on board of the rover, detected the presence of organic molecules on the surface of the planet in 2015, reinforcing the hypothesis of abundant organic matter on Mars [35]. The Cassini/Huygens mission has provided new information on the chemistry of the upper atmosphere of Titan, a moon of Saturn. The INMS ("Ion Neutral Mass Spectrometer") analyser, on board of Cassini, detected the presence of various hydrocarbons and nitrile compounds during a flyby of Titan [36]. The GCMS ("Gas Chromatograph Mass Spectrometer") analyser, on board of Cassini spacecraft, also detected the presence of organic species, such as cyanogen C_2N_2 or ethane C_2H_6 on the surface [37]. Measurements made during this mission also indicate the presence of aromatic species in the atmosphere of Titan [38]. The CIRS ("Composite Infrared Spectrometer") analyser, on board of Cassini, allowed the detection of several organic compounds, in particular the detection of benzene C_6H_6 [39]. Another important aspect is the presence of positive ions in Titan's atmosphere. Indeed, the Cassini INMS ("Ion and Neutral Mass Spectrometer") spectrometer has detected protonated methane CH_5^+ and protonated hydrogen isocyanide $HCNH^+$ in the ionosphere of this moon of Saturn [40]. In parallel to the in-situ missions, new generation telescopes have been used to characterise Titan. ALMA has enabled the mapping of the presence of several chemical compounds on Titan, complementing the measurements obtained by the Cassini mission. The emission map of acetonitrile CH_3CN around Titan measured by ALMA is shown in Figure 5 as an example [41].

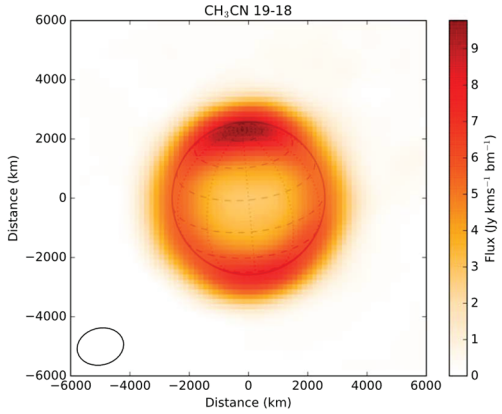

Figure 5: Integrated emission map produced by ALMA for the observation of acetonitrile CH_3CN on Titan. The flux is obtained by analysing the peaks associated with CH_3CN measured by the radio telescope. The ellipse at the bottom left indicates the spatial resolution. From M. A. Cordiner *et al.*, "ALMA Spectral Imaging of Titan Contemporaneous with *Cassini*'s Grand Finale", *AJ*, vol. 158, p. 4, 2019 [41].

The possibility of correlating spectroscopic data with the telescope's observing direction has also been implemented on ALMA data, for example for the two hot cores of the Large Magellanic Cloud, N113 A1 and N113 B3, whose spectra, extracted from [8], were presented previously in Figure 2. Figure 6 presents the integrated intensity images for methanol CH_3OH and dimethyl ether CH_3OCH_3 measured in the two hot cores A1 and B3 [42]. A1 and B3 are compact (diameter D≈0.17 pc) and are associated with H_2O (A1 and B3) and OH (A1) masers. Integrated intensity images for CH_3OH (top panel; made using the channels corresponding to all CH_3OH transitions in the 216.9 GHz spectral window), for CH_3OCH_3 (bottom panel; using $13_{0,13}$-$12_{1,12}$ transition), for the hot cores A1 (left column) and B3 (right column) in the N113 star-forming region are presented in this figure. For one telescope viewing direction, i.e. each point on the map, the spectral irradiance in Jy.beam^{-1}.km.s^{-1} is represented by a colour scale from blue to yellow. The Jansky (symbol Jy) is a non-SI unit of spectral irradiance, used especially in radio astronomy and equivalent to 10^{-26} W per square meter per hertz. Irradiance (W.m^{-2}) is the flux received by a surface per unit area. The spectral irradiance is given in Jy.km^{-1} and the amplitude of the peak in the spectrum is reported without normalization by its width. The spectral irradiance is given per beam, where beam is a nominal area over which the brightness is defined [43]. The size of the ALMA beam is indicated in the lower left corner of each image. The B3 maps correspond to a larger region of observation than those presented for A1. The white contours correspond to the 1.3 mm continuum emission. The red contours in the top right panel correspond to the CH_3OH emission with contour levels of (3, 5, 7) × 21 mJy.beam^{-1}, 21 mJy.beam^{-1} being the rms noise level of the CH_3OH integrated intensity image. The image shows the CH_3OH detection in other spots in a region where no other complex organic molecules (abbreviated COMs) are detected.

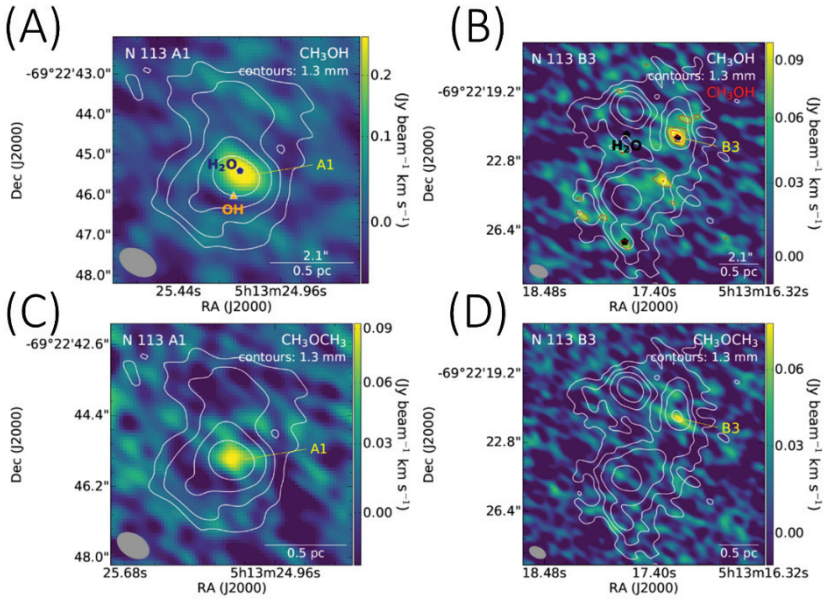

Figure 6: Integrated intensity images for CH_3OH (top panel; made using the channels corresponding to all CH_3OH transitions in the 216.9 GHz spectral window (see Figure 2), CH_3OCH_3 (bottom panel; 130.13-121.12 transition), for the A1 (left column) and B3 (right column) hot cores in the N113 star-forming region. The ALMA beam size is shown in the lower left corner of each image. The white contours correspond to the 1.3 mm continuum emission. The red contours in the top right panel correspond to the CH_3OH emission with contour levels of (3, 5, 7) × 21 mJy beam^{-1}, the rms noise level of the CH_3OH integrated intensity image. The image shows the CH_3OH detection in other spots in a region where no other COMs are detected. H_2O and OH masers are indicated, in blue and orange, respectively. From M. Sewilo *et al.*, "Complex Organic Molecules in Star-Forming Regions of the Magellanic Clouds", *ACS Earth Space Chem.*, vol. 3, p. 2097, 2019 [42].

In their article "Complex Organic Molecules in Star-Forming Regions of the Magellanic Clouds" [42], from which the Figure 6 comes from, Sewilo *et al.* compared the observations with theoretical model predictions. Theoretical models accounting for the physical conditions and metallicity of hot molecular cores in the Magellanic Clouds have been able to broadly account for the existing observations, but they fail to reproduce the dimethyl ether abundance by more than an order of magnitude [42]. The metallicity of the Magellanic Clouds is similar to that of galaxies in the earlier epochs of the universe; thus, the presence of COMs in the Large Magellanic Cloud (LMC) and Small Magellanic Cloud (SMC) indicates that a similar prebiotic chemistry leading to the emergence of life, as it happened on Earth, is possible in low-metallicity systems in the earlier universe.

The column density measures the amount of intermediate matter between an observer and the observed object. According to the work of Sewilo *et al.* [42], column densities for H_2 of $(8.0 \pm 1.2) \times 10^{23}$ and $(7.0 \pm 0.9) \times 10^{23}$ cm^{-2} and number densities for H_2 of $\sim 1.6 \times 10^6$ and $\sim 1.4 \times 10^6$ cm^{-3} for A1 and B3, respectively, were estimated using the 1.3 mm continuum data. Local thermodynamic equilibrium (LTE) analysis of six CH_3OH transitions yielded to rotational

temperatures and total column densities (T_{rot}, N_{tot}) of (134 ± 6 K, (1.6 ± 0.1) × 10^{16} cm^{-2}) and (131 ± 15 K, (6.4 ± 0.8) × 10^{15} cm^{-2}) for A1 and B3, respectively. These numbers and column densities, as well as the temperatures of A1 and B3 outside the Galaxy, are consistent with the classical hot cores observed in the Galaxy. The emission of COMs and the association with masers are also among the main characteristics of hot cores. The column densities of (CH_3OH, CH_3OCH_3) are (16 ± 1, 1.8 ± 0.5) × 10^{15} cm^{-2} for A1 and (6.4 ± 0.8, 1.2 ± 0.4) × 10^{15} cm^{-2} for B3. The column density for CH_3OCH_3 was estimated using the same T_{rot} as for CH_3OH, assuming that these molecular species are located in the same region as CH_3OH in A1 and B3. The fractional abundances (CH_3OH, CH_3OCH_3) relative to H_2 are (20 ± 3, 2.2 ± 0.7) × 10^{-9} for A1 and (9.1 ± 1.7, 1.7 ± 0.7) × 10^{-9} for B3. When scaled by a factor of 2.5 to account for the lower metallicity in the LMC, the COMs abundances detected in N113 are comparable to the lowest values found for Galactic hot nuclei. This result contrasts with previous observational and theoretical studies indicating a very low CH_3OH abundance in LMC. Thus, the COMs observed in N113 hot cores could originate either from the surface chemistry of the grains or from the post-desorption gas chemistry.

The PEACHES ("Perseus ALMA Chemistry Survey") project aims to characterise the COMs' chemistry in protostellar systems located in the Perseus molecular cloud, in the Milky Way. As part of this project, eleven hot corinos, located in the Perseus cloud, have been studied by Yang *et al.*, using the ALMA observations [11]. In their work, Yang *et al.* concluded that the correlation observed between the presence of COMs is insensitive to the protostellar system properties. The abundance of larger COMs (CH_3OCHO and CH_3OCH_3) relative to that of smaller COMs (CH_3OH and CH_3CN) increases with the inferred gas column density, hinting at an efficient production of complex species in denser envelopes.

The results of the molecular abundance measurements obtained in the star-forming environments can be compared to the molecular abundances measured by ROSINA during the Rosetta mission, around the comet 67P. Drozdovskaya *et al.* [26] found a linear correlation between the abundances of different molecules measured in the comet and those measured with ALMA in the hot corino IRAS 16293-2422 B. Figure 7 shows the correlation diagram between the two abundance measurements. The abundances are normalized to that of methanol. Note the specific case of glycine; its abundance is measured for the comet and the current detection limit in IRAS 16293-2422 is shown. Note that this limit is compatible with the observed correlation line.

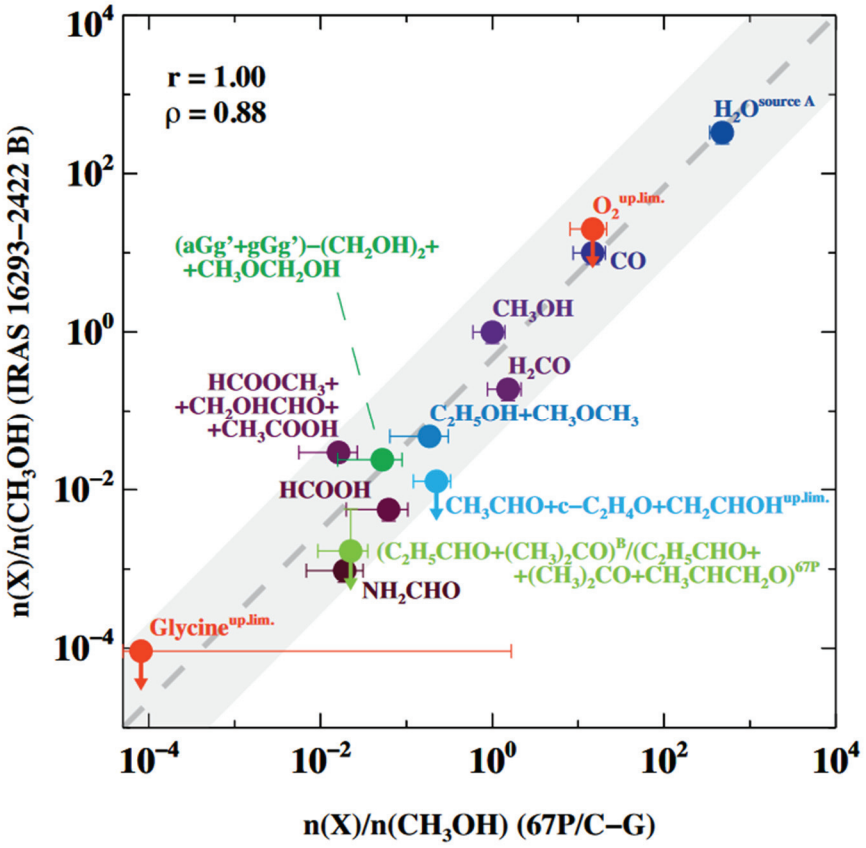

Figure 7: Correlation diagram of abundances measured with the ALMA telescope on IRAS 16293-2422 (vertical axis) and those measured around comet 67P/ChuryumovGerasimenko with the ROSINA spectrometer (horizontal axis). Each molecule is associated with a given colour. Molecular abundances are normalized to that of methanol. The grey dotted line represents a linear fit and the grey region corresponds to an order of magnitude around the linear fit. The correlation coefficients, Pearson (r) and Spearman (ρ) are shown in the upper left corner. From M. N. Drozdovskaya *et al.*, "Ingredients for solar-like systems: protostar IRAS 16293-2422 B versus comet 67P/Churyumov-Gerasimenko", *MNRAS*, vol. 490, p. 52, 2019 [26].

Altwegg, Balsiger and Fuselier [23] stressed the importance of the evidence for such correlations between the protostellar system and the comet, which seems to show that most of the molecular complexity observed in the comet may have arisen during the protostellar phase.

2. Mechanisms of molecules formation in space

The formation and survival of any molecule in space has long been considered incompatible with the physical conditions in interstellar space (very low gas density, very low temperatures, UV radiation). A first key is the presence of ejected dust which, concentrated in clouds, effectively absorbs the UV radiation emitted by distant stars and protects the molecules already formed from rapid destruction by photodissociation. Space presents a great diversity in terms of density range and temperature range, nevertheless one could underline, by analogy, the presence in the first 100 km of the Earth's atmosphere of a great diversity of aerosol sizes, fine

particles ranging from molecular clusters (nm) to solid size particles of the order of a hundred microns [44]. These fine particles act as catalysts [45], by providing a kind of molecular crucible in which atoms and/or molecules can attach, meet, and react [46] [47]. On the surface of these fine particles, molecular hydrogen and many more complex molecules such as formaldehyde H_2CO or methanol CH_3OH are formed. Time is the second key. The lifetimes of most astronomical objects, especially interstellar clouds, are in the hundreds of thousands or even millions of years. Such lifetimes allow even rare atoms and molecules to react with each other in these environments associated to a very low density. On the other hand, the very low density considerably prolongs the life span of the molecules formed. In addition, many ions and free radicals can be observed in space that would not survive in terrestrial conditions. These ions and radicals react more rapidly with other molecules than do stable neutral species. Finally, it should be noted that the atmospheres of stars such as the Sun, Betelgeuse, or CW Leonis are sufficiently dense and hot for ternary reactions to occur very rapidly and form, directly from atoms, a range of physically stable molecules in proportions defined by thermodynamic equilibrium: CO, CS, C_2H_2, HCN, SiC, SiO, SiS, etc. The molecules thus formed are ejected into the cold interstellar medium. A large proportion of them condenses in the form of dust grains. The others will constitute the seeds of the formation of more complex molecules either by migrating on the surface of the grains or moving freely in the gas phase, by means of binary reactions, as in the case of ion-molecule, neutral-neutral reactions, etc. Thus, a wide variety of gas phase processes could explain the formation of complex molecules in these extreme regions. For example, the gas-phase reaction between protonated methanol and methanol is considered an efficient way to explain the production of dimethyl ether in such environments [7].

The low temperatures and density conditions observed in interstellar environments can lead to the aggregation of molecules to form a molecular cluster. The stability of such a cluster is higher in the presence of a proton species. Moreover, the formation of these small clusters increases the interaction time between the molecules. Thus, small protonated molecular clusters may appear to be a promising route for the formation of more complex molecules in space [7], as intermolecular bonding can increase the interaction times between molecules and thus the formation of new molecules by a unimolecular reaction within the cluster.

The presence of a proton facilitates the formation of small molecular clusters. The proton is undeniably involved in a wide range of physicochemical phenomena on earth. In the context of this work, one can mention the proton transfer reaction on neutral molecules to be analysed used in PTR-MS ("Proton-Transfer-Reaction Mass Spectrometry") technology in mass spectrometry [48] [49], or the influence of protons on aerosols formation in the atmosphere [45]. In space, the proton comes into play with the formation of the first molecule HeH^+ and will promote the formation of the observed diversity of molecules. In 1996, Geballe and Oka reported the first detection of H_3^+ in the interstellar medium, in the two protostellar systems GL-2136 and

W33A [50]. Since then, H_3^+ has been widely observed in space. The H_3^+ ion plays a central role in the evolution of chemistry, especially in star-forming regions. The initial formation mechanism of H_3^+ is described by the following equation:

$$H_2 + H_2^+ \rightarrow H_3^+ + H \quad (1)$$

This reaction is strongly exothermic, giving off about 1.7 eV, and has a high Langevin rate constant, about 2×10^{-9} $cm^3.s^{-1}$ [51]. The high efficiency of this reaction has been observed in small clusters of hydrogen isolated in the gas phase under irradiation [52] [53]. In regions of excess hydrogen, H_3^+ becomes the most abundant ion. Once formed, the H_3^+ ion acts upon interaction with a neutral molecule as a remarkable proton donor. The proton affinity of H_2, 4.4 eV [51], is lower than that of most atoms and molecules, leading to the formation of protonated species, as shown in the following equation:

$$H_3^+ + X \rightarrow HX^+ + H_2 \quad (2)$$

The presence of H_3^+ in the interstellar medium leads to the presence of protonated species in interstellar locations such as molecular clouds. These protonated molecular ions have large reaction rate constants with other molecules, thereby favouring the formation of more complex molecules [54]. Figure 8 presents a schematic view of ion-molecule reactions highlighting the crucial role of H_3^+ in the astrophysical context, especially in the formation of protonated species such as the protonated methanol H^+CH_3OH, hydronium ion H_3O^+ and the protonated dimer of water $H_5O_2^+$ which can also be denoted $(H_3O)^+H_2O$.

The presence of molecular ions in the interstellar medium is crucial as allows for increased reaction rates. These reactions, which are considered to be fast, typically occur at the 'maximum' Langevin rate (2.10^{-9} $cm^3.s^{-1}$). The reaction times are long when the gas density in interstellar clouds is low and the gas temperature is low. The reactants are very low in abundance, since the concentration of CO, the most abundant molecule after H_2, is about 10^4 times lower than that of H_2 and is only one particle per cm^3 in the so-called 'dense' clouds. The characteristic time for the transformation of an H_3^+ ion into HCO^+ by collision of H^+ with a CO molecule, a very favourable case, is then of the order of 400 years. Similar with the formation of H_3^+ in hydrogen clusters or the formation of small protonated water clusters $H^+(H_2O)_n$, more complex molecules such as methanol can also be found as protonated molecular clusters $H^+(CH_3OH)_n$. Thus, the production of protonated species leads to the formation of protonated molecular clusters [7] whose presence promotes reactivity between molecules.

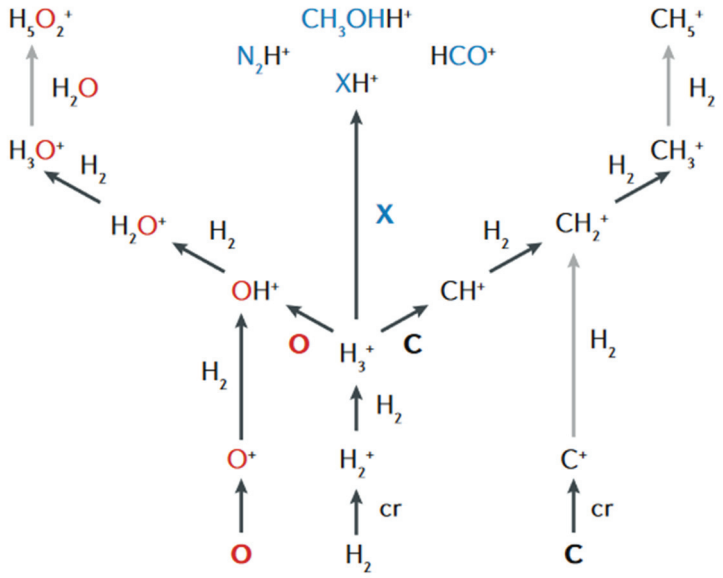

Figure 8: Ion-molecule reactions leading to the formation of protonated methanol, protonated water clusters and other protonated species. The shape and colour of the arrows are associated with the type of reaction, depending on the interstellar medium. From B. A. McGuire *et al.*, "Laboratory spectroscopy techniques to enable observations of interstellar ion chemistry", *Nat. Rev. Phys.*, vol. 2, p. 2, 2020 [54].

The observation of protonated species in space is linked to the determination of their spectroscopic signature and thus knowledge about these characteristics. Infrared signatures of primary alcohol cations have been explored in the cryogenic ion trap beam line at the FELIX free-electron laser laboratory by Jusko *et al.* [55]. Using infrared vibrational predissociation (IR-PD) the authors studied the simple alcohol cations of methanol and ethanol as well as their protonated forms. Spectra are taken by tagging the cold molecular ions with He atoms. The infrared spectrum of protonated methanol was thus recorded for the first time, and the wavelength coverage for all other species is substantially extended. Laboratory rest frequencies for rotational transitions of protonated methylamine $CH_3NH_3^+$, have also been measured recently in a cryogenic 22-pole ion trap machine by Schlemmer and coworkers [56]. For this prolate symmetric top molecule thirteen transitions between 80 and 240 GHz were detected in the ground vibrational state. The $CH_3NH_3^+$ spectral line transitions have frequencies >40 GHz and therefore constitute for instance good targets to be searched for with facilities like ALMA.

Bibliography

[1] C.D.M.S. classic documentation Koeln Universität, "Molecules in Space". [Online]. https://cdms.astro.uni-koeln.de/classic/molecules

[2] R. Güsten et al., "Astrophysical detection of the helium hydride ion HeH+," *Nature*, vol. 568, pp. 357–359, April 2019.

[3] Académie Européenne Interdisciplinaire des Sciences, *Formation des systèmes stellaires et planétaires: Conditions d'apparition de la vie*, G. Belaubre et al., Eds.: EDP Sciences, 2016.

[4] B. K. D. Pearce, R. E. Pudritz, D. A. Semenov, and T. K. Henning, "Origin of the RNA world: The fate of nucleobases in warm little ponds," *PNAS*, vol. 114, pp. 11327–11332, October 2017.

[5] U. Pedreira-Segade, J. Hao, G. Montagnac, H. Cardon, and I. Daniel, "Spontaneous Polymerization of Glycine under Hydrothermal Conditions," *ACS Earth Space Chem.*, vol. 3, pp. 1669–1677, July 2019.

[6] I. Daniel, P. Oger, and R. Winter, "Origins of life and biochemistry under high-pressure conditions," *Chem. Soc. Rev.*, vol. 35, p. 858, 2006.

[7] G. A. Olah, T. Mathew, G. K. Surya Prakash, and G. Rasul, "Chemical Aspects of Astrophysically Observed Extraterrestrial Methanol, Hydrocarbon Derivatives, and Ions," *J. Am. Chem. Soc.*, vol. 138, pp. 1717–1722, January 2016.

[8] M. Sewiło et al., "The Detection of Hot Cores and Complex Organic Molecules in the Large Magellanic Cloud," *ApJ*, vol. 853, January 2018.

[9] E. Herbst and E. F. van Dishoeck, "Complex Organic Interstellar Molecules," *ARA&A*, vol. 47, pp. 427–480, September 2009.

[10] S. E. Kurtz et al., "The potential for a K-band receiver on the Large Millimeter Telescope," December 2020.

[11] Y. Yang et al., "The Perseus ALMA Chemistry Survey (PEACHES). I. The Complex Organic Molecules in Perseus Embedded Protostars," *ApJ*, vol. 910, p. 20, March 2021.

[12] S. K. Mondal et al., "Is There Any Linkage between Interstellar Aldehyde and Alcohol?," *ApJ*, vol. 922, p. 194, November 2021.

[13] A. Manna and S. Pal, "Identification of interstellar amino acetonitrile in the hot molecular core G10.47+0.03: Possible glycine survey candidate for the future," *Life Sci. Space Res.*, vol. 34, pp. 9–15, August 2022.

[14] P. Gorai et al., "Identification of Prebiotic Molecules Containing Peptide-like Bonds in a Hot Molecular Core, G10.47+0.03," *ApJ*, vol. 895, p. 86, May 2020.

[15] E. Bianchi et al., "The Two Hot Corinos of the SVS13-A Protostellar Binary System: Counterposed Siblings," *Astrophys. J. Lett.*, vol. 928, p. L3, March 2022.

[16] L. Colzi et al., "The GUAPOS project: II. A comprehensive study of peptide-like bond molecules," *A&A*, vol. 653, p. A129, September 2021.

[17] B. J. McCall, "Spectroscopy of H3+ in laboratory and astrophysical plasmas," University of Chigago, Ph.D. dissertation 2001. [Online]. bjm.scs.illinois.edu/miscpubs/McCall2001.pdf

[18] T. Soma, N. Sakai, Y. Watanabe, and S. Yamamoto, "Complex Organic Molecules in Taurus Molecular Cloud-1," *ApJ*, vol. 854, p. 116, February 2018.

[19] M. Agúndez et al., "O-bearing complex organic molecules at the cyanopolyyne peak of TMC-1: Detection of C2H3CHO, C2H3OH, HCOOCH3, and CH3OCH3," *A&A*, vol. 649, p. L4, May 2021.

[20] A. Korth et al., "Mass spectra of heavy ions near comet Halley," *Nature*, vol. 321, pp. 335–336, May 1986.

[21] A. Wootten et al., "A search for interstellar H3O+," *A&A*, vol. 166, pp. L15-L18, September 1986.

[22] J. E. Elsila, D. P. Glavin, and J. P. Dworkin, "Cometary glycine detected in samples returned by Stardust," *Meteorit. Planet. Sci.*, vol. 44, pp. 1323–1330, September 2009.

[23] K. Altwegg, H. Balsiger, and S. A. Fuselier, "Cometary Chemistry and the Origin of Icy Solar System Bodies: The View After Rosetta," *ARA&A*, vol. 57, pp. 113–155, August 2019.

[24] K. Hadraoui et al., "Distributed glycine in comet 67P/Churyumov-Gerasimenko," *A&A*, vol. 630, p. A32, September 2019.

[25] K. Altwegg et al., "Prebiotic chemicals—amino acid and phosphorus—in the coma of comet 67P/Churyumov-Gerasimenko," *Sci. Adv.*, vol. 2, May 2016.

[26] M. N. Drozdovskaya, E. F. van Dishoeck, M. Rubin, J. K. Jørgensen, and K. Altwegg, "Ingredients for solar-like systems: protostar IRAS 16293-2422 B versus comet 67P/Churyumov–Gerasimenko," *MNRAS*, vol. 490, pp. 50–79, September 2019.

[27] A. E. Rubin, J. M. Trigo-Rodrìguez, H. Huber, and J. T. Wasson, "Progressive aqueous alteration of CM carbonaceous chondrites," *Geochim. Cosmochim. Acta*, vol. 71, pp. 2361–2382, May 2007.

[28] M. H. Engel and B. Nagy, "Distribution and enantiomeric composition of amino acids in the Murchison meteorite," *Nature*, vol. 296, pp. 837–840, April 1982.

[29] P. Schmitt-Kopplin et al., "High molecular diversity of extraterrestrial organic matter in Murchison meteorite revealed 40 years after its fall," *PNAS*, vol. 107, pp. 2763–2768, February 2010.

[30] K. Kvenvolden et al., "Evidence for Extraterrestrial Amino-acids and Hydrocarbons in the Murchison Meteorite," *Nature*, vol. 228, pp. 923–926, December 1970.

[31] S. Pizzarello, L. B. Williams, J. Lehman, G. P. Holland, and J. L. Yarger, "Abundant ammonia in primitive asteroids and the case for a possible exobiology," *PNAS*, vol. 108, pp. 4303–4306, February 2011.

[32] Z. Martins, "The Nitrogen Heterocycle Content of Meteorites and Their Significance for the Origin of Life," *Life*, vol. 8, p. 28, July 2018.

[33] Y. Oba et al., "Identifying the wide diversity of extraterrestrial purine and pyrimidine nucleobases in carbonaceous meteorites," *Nat. Commun.*, vol. 13, April 2022.

[34] P. R. Mahaffy et al., "The Sample Analysis at Mars Investigation and Instrument Suite," *Space Sci. Rev.*, vol. 170, pp. 401–478, April 2012.

[35] J. L. Eigenbrode et al., "Organic matter preserved in 3-billion-year-old mudstones at Gale crater, Mars," *Science*, vol. 360, pp. 1096–1101, June 2018.

[36] J. H. Waite et al., "Ion Neutral Mass Spectrometer Results from the First Flyby of Titan," *Science*, vol. 308, pp. 982–986, May 2005.

[37] H. B. Niemann et al., "The abundances of constituents of Titan's atmosphere from the GCMS instrument on the Huygens probe," *Nature*, vol. 438, pp. 779–784, November 2005.

[38] C. Mathé, T. Gautier, M. G. Trainer, and N. Carrasco, "Detection Opportunity for Aromatic Signature in Titan's Aerosols in the 4.1 to 5.3 micron range," *ApJ*, vol. 861, p. L25, July 2018.

[39] A. Coustenis et al., "The composition of Titan's stratosphere from Cassini/CIRS mid-infrared spectra," *Icarus*, vol. 189, pp. 35–62, July 2007.

[40] T. E. Cravens et al., "Composition of Titan's ionosphere," *Geophys. Res. Lett.*, vol. 33, 2006.

[41] M. A. Cordiner et al., "ALMA Spectral Imaging of Titan Contemporaneous with Cassini's Grand Finale," *AJ*, vol. 158, p. 76, July 2019.

[42] M. Sewiło et al., "Complex Organic Molecules in Star-Forming Regions of the Magellanic Clouds," *ACS Earth and Space Chem.*, vol. 3, pp. 2088–2109, August 2019.

[43] ALMA INAF [Online]. https://www.alma.inaf.it/images/Mignano_liuzzo.pdf

[44] M. Kulmala et al., "Chemistry of Atmospheric Nucleation: On the Recent Advances on Precursor Characterization and Atmospheric Cluster Composition in Connection with Atmospheric New Particle Formation," *Annu. Rev. Phys. Chem.*, vol. 65, pp. 21–37, April 2014.

[45] L. Feketeová et al., "Impact of a hydrophobic ion on the early stage of atmospheric aerosol formation," *PNAS*, vol. 116, pp. 22540–22544, October 2019.

[46] T. I. Hasegawa and E. Herbst, "New gas–grain chemical models of quiescent dense interstellar clouds: the effects of H2 tunnelling reactions and cosmic ray induced desorption," *MNRAS*, vol. 261, pp. 83–102, March 1993.

[47] Y. Lu, Q. Chang, and Y. Aikawa, "The Chemical Evolution from Prestellar to Protostellar Cores: A New Multiphase Model with Bulk Diffusion and Photon Penetration," *ApJ*, vol. 869, p. 165, December 2018.

[48] F. Biasioli et al., "Coupling Proton Transfer Reaction-Mass Spectrometry with Linear Discriminant Analysis: a Case Study," *Journal of Agricultural and Food Chemistry*, vol. 51, pp. 7227–7233, November 2003.

[49] IONICON Company [Online]. https://www.ionicon.com/

[50] T. R. Geballe and T. Oka, "Detection of H3+ in interstellar space," *Nature*, vol. 384, pp. 334–335, November 1996.

[51] T. Oka, "Interstellar H3+," *PNAS*, vol. 103, pp. 12235–12242, August 2006.

[52] B. Farizon, M. Farizon, M. J. Gaillard, E. Gerlic, and Ouaskit, "Multiple H3+ fragment production in single collision of fast Hn clusters with He atoms," *Zeitschrift für Physik D Atoms, Molecules and Clusters*, vol. 33, pp. 53–57, March 1995.

[53] B. Farizon et al., "Direct observation of multi-ionization and multi-fragmentation in a high-velocity cluster-atom collision," *Chem. Phys. Lett.*, vol. 252, pp. 147–152, April 1996.

[54] B. A. McGuire, O. Asvany, S. Brünken, and S. Schlemmer, "Laboratory spectroscopy techniques to enable observations of interstellar ion chemistry," *Nat. Rev. Phys*, vol. 2, pp. 402–410, July 2020.

[55] P. Jusko et al., "The FELion cryogenic ion trap beam line at the FELIX free-electron laser laboratory: infrared signatures of primary alcohol cations," *Faraday Discuss.*, vol. 217, pp. 172–202, 2019.

[56] P. C. Schmid et al., "Rotational Rest Frequencies and First Astronomical Search of Protonated Methylamine," *Front. Astron. Space Sci.*, vol. 8, February 2022.

Chapter II

Study of the relaxation of small protonated molecular clusters induced by a single collision

This chapter presents the tools and methods used to study single collision induced relaxation of small protonated molecular clusters. The first section presents the "Molecular Cluster Irradiation Device" (Dispositif d'Irradiation d'Agrégats Moléculaires, DIAM). In this setup, a beam of protonated molecular clusters, energy- and mass-selected, passes through an argon gas jet under single collision conditions. In the second section, the COINTOF-VMI (COrrelated Ion and Neutral Time Of Flight – Velocity Map Imaging) method is described. This method is used to detect the fragments resulting from the post-collisional relaxation of each parent cluster ion, and to obtain multiparametric data for each collision event. The next sections are devoted to identification of the relaxation channels, measurements of the detection efficiency of the neutral fragments, and the determination of the branching ratio values between the several observed relaxation channels. The last section presents the theoretical methods that are used in combination with the experimental technique.

1. Molecular Cluster Irradiation Device

The "Molecular Cluster Irradiation Device", abbreviated DIAM (*Dispositif d'Irradiation d'Agrégats Moléculaires*), developed by the "Particle-Matter Interactions", abbreviated IPM (*Interactions Particule Matière*), team of the Institut de Physique des 2 Infinis (IP2I) in Lyon, allows to study the relaxation of protonated molecular cluster ions, excited by a collision in a crossed beam setup. DIAM produces high intensity beams of protonated cluster ions energy- and mass-selected [1] [2]. After passing through a noble gas atom jet in the collision chamber, the beam is analysed with a detection system based on the "COrrelated Ion and Neutral Time Of Flight – Velocity Map Imaging" (COINTOF-VMI) method [3]. Figure 9 shows a schematic view of the experimental setup, from the cluster source to the detection system.

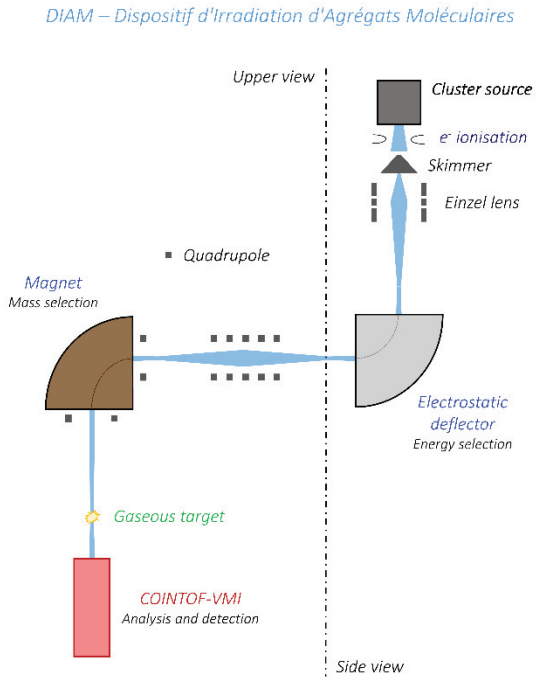

Figure 9: Schematic view of the DIAM device.

In summary, the neutral clusters are formed by the adiabatic expansion of a carrier gas spiked with a vapour of the molecular species of interest. The temperature and pressure are kept constant during the measurements. Neutral clusters are ionised by electron impact and the resulting protonated clusters are accelerated by a given voltage (8 kV in the present work). The resulting cluster ion beam is successively selected in energy and mass, respectively with the electrostatic sector and the magnetic one. The delay between the formation of the protonated clusters and the mass selection is typically 1 ms. This delay is long enough to strongly reduce spontaneous evaporation in the experiment, the relaxation time of the metastable states is typically few µs. The ion beam passes through a jet of atomic gas (argon in this work) and the

target density is controlled to ensure single collision conditions. The energy deposition resulting from this single collision occurs in a very short time (fs) compared to the typical time of the dynamics of nuclei in the molecular cluster. Post-collisional relaxation of the parent cluster ion can reveal various dissociation channels. The resulting charged fragment and the neutral one(s) are analysed and detected, event by event, using the COINTOF-VMI method.

2. The COINTOF-VMI method

2.1. The production of correlated multiparametric data sets

A scan over the magnetic field values records the mass spectrum of the molecular ions produced for given working parameters of the cluster source. After this measurement, the protonated clusters of interest are selected and, during an experiment, the energy and the mass of the parent cluster ion are kept fixed. A single collision, between a cluster and an atom, can induce dissociation of the parent cluster ion and the fragments are detected and analysed with the COINTOF method, developed by the IPM team [3]. The COINTOF method is based on the correlated measurement of the arrival times associated to the different fragments resulting from the fragmentation of a single parent cluster ion on the detector. Figure 10 shows a schematic view of the COINTOF method. The analyser consists of an acceleration zone, a field-free time of flight (TOF) zone, and a microchannel plate (MCP) detector equipped with a delay line anode (DLA).

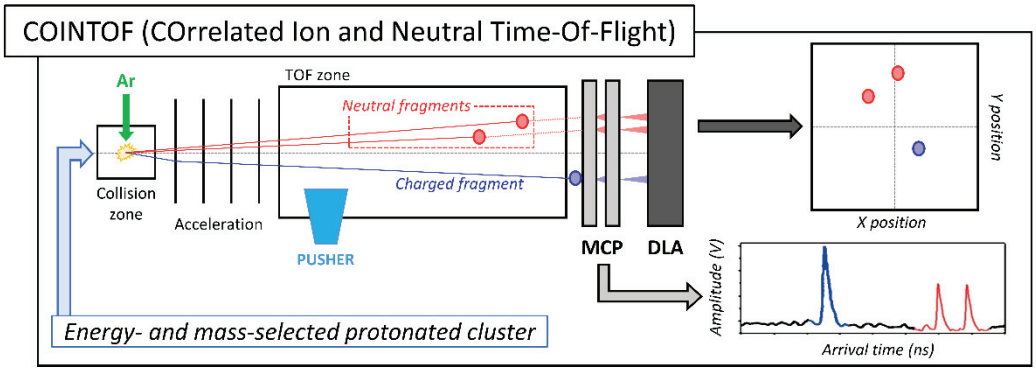

Figure 10: Schematic view of the COINTOF method.

After passing through the gas target, the beam contains excited clusters that fly towards the analyser. Before entering the analyser, there is a free flight distance where the excited clusters may dissociate. This distance corresponds to a given relaxation time window which depends on the fixed velocity of the parent cluster ions. Upon entering the acceleration zone, the charged fragments are accelerated with a selected voltage (-1700 V). The neutral fragments are not

accelerated. After the acceleration zone, the fragments enter a field-free TOF zone where velocity differences between the fragments are converted into arrival time differences at the detector.

For each dissociated and analysed parent ion, the arrival time on the detector of each fragment is recorded, and labelled as corresponding to a fragment of that given dissociated parent cluster ion. Such labelling of measurements, based on each individual parent ion, leads to the production of a multiparametric data set, in which a dissociation event is linked to a single dissociated parent ion. The analysis of this multiparametric data set allows to calculate the arrival time differences between fragments for each dissociation event.

In addition to the correlated arrival times measurement, for the charged and the neutral fragments, the COINTOF method allows the measurement of the multiplicity of each dissociation event. Indeed, among the post collisional relaxation channels, the production of several neutral fragments, associated with a given daughter ion, is observed. The number of fragments resulting from the relaxation of a given parent ion, during the relaxation time window of the experiment, after a single collision, is called the dissociation event multiplicity. Due to a detection efficiency lower than 100%, the raw multiplicity (m_d) of an event, corresponding to the number of fragments that are detected for a single parent cluster ion, is less or equal to the dissociation event multiplicity. In addition, several strategies have been developed to measure the detection efficiency of the different fragments, thus allowing the measurement of branching ratios for the several observed relaxation channels.

The detector consists of a pair of Hamamatsu MCPs, with a diameter of 20 mm, for the effective area, and containing single channels, with a diameter of 12 µm. The two MCPs are mounted in a *chevron* configuration. The electronic pulse, taken from the front of the first MCP, gives the arrival time of the detected particles. A DLA is used to measure the impact position of each individual particle on the detector. The burst of electrons, extracted from the back of the second MCP, produces signals at the ends of each wire of the two perpendicular delay lines. Using a time-to-digital converter, the arrival time and impact position are recorded for each detected particle, and labelled for each individual parent cluster ion. Measurements are made for a large number of dissociated parent cluster ions, previously selected according to their mass and energy. Several tools have been developed to perform the analysis of the multiparametric data set obtained after a given experiment.

2.2. The COINTOF spectra

The COINTOF mass spectrum of the daughter ions is given by the histogram of the arrival time difference between the fragments resulting from the relaxation of each parent cluster ion. Indeed, for a single parent ion, due to the acceleration, the first fragment on the detector is

the daughter ion and the next ones are neutral fragments. For each dissociation event, the labelling of the fragments, in order of arrival time, allows to calculate the arrival time difference Δt_{12} between the first impact (hit #1), associated to the daughter ion, and the second one (hit #2), associated to a neutral fragment. For each parent ion that dissociates, the time difference Δt_{12} is characteristic of the mass-to-charge ratio of the daughter ion. Thus, the COINTOF mass spectrum of the charged fragments is constructed from successive measurements of arrival time differences, for a large number of parent cluster ion dissociation events.

The identification of individual daughter ions from the Δt measurements is performed using a Monte Carlo simulation of the COINTOF analyser. This simulation calculates the trajectory of the neutral and charged fragments as they fly towards the detector after the collision. For each fragment, the kinetic energy release (KER) can be considered by adding an additional velocity to each fragment. The total KER released during the dissociation is distributed among the fragments respecting the momentum conservation. The simulation includes all the different zones of the COINTOF analyser. The arrival time and the impact position on the detector are recorded for all fragments of each cluster. The calculation is performed for the different relaxation channels, for at least 10^5 parent cluster ions. The information is stored in a ROOT tree object allowing histograms to be plotted. The peak positions in the calculated COINTOF spectrum allows the association between the time difference and the mass of the charged fragment. The width of the peak in the COINTOF spectrum is related to the additional velocity distribution due to the KER. A detailed description of the simulation is presented in the reference [3], applied to the evaporation of one to several H_2O molecules from protonated water clusters.

Figure 11 shows the measured COINTOF mass spectra of the charged fragments associated with the relaxation of the protonated pyridine dimer $H^+(Pyr)_2$. In the upper part of Figure 11, six peaks are observed. According to the Monte Carlo simulation, the first peak, with a maximum at Δt of 0.40 µs, corresponds to a mass to charge ratio of 80 amu and is associated with the protonated pyridine H^+Pyr. This first peak is related to the evaporation process described as follows:

$$H^+(Pyr)_2 \rightarrow H^+Pyr + Pyr \quad (1)$$

The maximum of the second peak occurs at a Δt value of 0.56 µs, corresponding to a charged fragment with a mass of 53 amu, associated with the $C_4H_4H^+$ ion. The detection of this daughter ion is related to a relaxation channel that involves the breaking of the initial proton bond but also the breaking of covalent bonds. The presence of the $C_4H_4H^+$ daughter ion can be linked to the following dissociation channel:

$$H^+(Pyr)_2 \rightarrow C_4H_4H^+ + HCN + Pyr \quad (2)$$

The third peak in the upper plot of Figure 11 corresponds to a Δt value of 0.68 µs, corresponding to a charged fragment with a mass of 39 amu, associated with the daughter ion $C_3H_3^+$. This charged fragment results again from the breaking of the initial proton bond and covalent bonds. The presence of the $C_3H_3^+$ daughter ion can be linked to the following dissociation channel:

$$H^+(Pyr)_2 \rightarrow C_3H_3^+ + C_2H_2N + Pyr \quad (3)$$

The fourth peak is associated with a Δt value of 0.86 µs which corresponds to a charged fragment with a mass of 28 amu. This mass is associated with the daughter ion $HCNH^+$. The presence of the daughter ion $HCNH^+$ can be linked to the following dissociation channel:

$$H^+(Pyr)_2 \rightarrow HNCH^+ + C_4H_4 + Pyr \quad (4)$$

The fifth peak is at a Δt value of 1.21 µs which corresponds to a daughter ion mass of 13 amu, associated with CH^+. The presence of the CH^+ daughter ion can be related to the following dissociation channel:

$$H^+(Pyr)_2 \rightarrow CH^+ + C_4H_5N + Pyr \quad (5)$$

The last peak identified in the COINTOF mass spectrum of $H^+(Pyr)_2$, is associated with a Δt value of 2.26 µs. According to the Monte Carlo simulation, such Δt value is related to a charged fragment with a mass of 1 amu, which corresponds to H^+. The presence of the daughter ion H^+ can be related to the following dissociation channel:

$$H^+(Pyr)_2 \rightarrow H^+ + Pyr + Pyr \quad (6)$$

In the different relaxation channels proposed in Equations (1-6), the neutral fragments can also be excited and can therefore also be expected to dissociate, when the energy deposition, induced by the collision, is large.

In the upper part of Figure 11, the histogram is constructed with a selection of dissociation events with a raw multiplicity, m_d, of 2, i.e. for these dissociation events only two fragments were detected, the charged one and a neutral one. The data set also contains dissociation events with a raw multiplicity, m_d, of 3, i.e. for these dissociation events three fragments were detected, the charged one and the two neutral ones. The histogram in the lower part of Figure 11 is constructed with these events. For each dissociation event, two distinct arrival time differences can be calculated: the arrival time difference Δt_{12}, between the second impact (hit #2) and the first one (hit #1), and the arrival time difference Δt_{13}, between the third impact (hit #3) and the first one (hit #1).

As in the case of a raw multiplicity of 2, the first impact is associated with the charged fragment, while the second and third impacts correspond to the two neutral fragments. For the events with a raw multiplicity of 3, the mean histogram of the arrival time differences, denoted $<\Delta t>$ is calculated and it is also plotted in Figure 11.

As expected, the histograms of Δt_{12} (pink curve) and Δt_{13} (yellow curve) show a systematic shift, Δt_{12} being by definition larger than Δt_{13}. More interesting is the position of the peak given by the histogram of the mean arrival time difference $<\Delta t>$ (grey curve) which corresponds to the peaks observed in the upper part of Figure 11. The position of the peaks in the $<\Delta t>$ histogram, constructed with events with a raw multiplicity of 3, coincides with the position of the peaks in the Δt_{12} spectrum constructed considering events with a raw multiplicity of 2.

The same charged fragments are observed in the two plots in Figure 11. However, the ratios between the peaks are not the same in the case of a raw multiplicity of 2 and 3. The most striking feature is the presence of the first peak at Δt value of 0.4 µs, even for a raw multiplicity of 3. Indeed, the detection of two neutral fragments in correlation with the pyridinium ion H^+Pyr, indicates that fragmentation of the neutral molecule Pyr is occurring. Such behaviour has also been observed with protonated methanol clusters studied with DIAM [4].

The second peak, which is related to Equation (2), is associated with the production of two neutral fragments, HCN and Pyr, in addition to the daughter ion $C_4H_4H^+$. In the experiment, either one of the neutral fragments is detected, HCN or Pyr, or both neutral fragments are detected, HCN and Pyr, in correlation with the daughter ion. This behaviour is related to the detection efficiencies of the corresponding neutral fragments, and it will be used in the following section to measure the detection efficiencies of these neutral fragments.

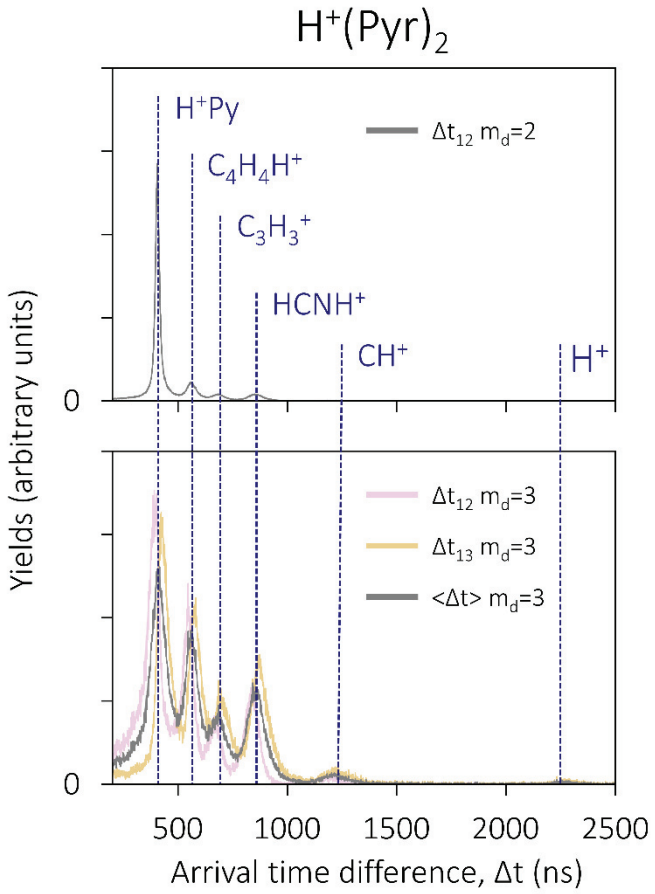

Figure 11: COINTOF mass spectra of charged fragments for the dissociation of protonated pyridine dimer $H^+(Pyr)_2$ (accelerated to 8 keV) induced by a single collision with an argon atom. Upper plot: histogram of the arrival time difference between the charged fragment and the neutral fragment Δt_{12} (grey curve). In this case, dissociation events selected to construct the histogram correspond to the detection of 2 fragments (m_d=2). Lower plot: histogram of the arrival time difference between the charged fragment and neutral ones, associated with the detection of two neutral fragments. In this case, dissociation events which have been selected correspond to the detection of 3 fragments (m_d=3). The pink curve corresponds to the arrival time difference Δt_{12} between the first fragment, i.e., the charged one (hit #1), and the first neutral fragment (hit #2). The yellow curve corresponds to the histogram of the arrival time difference Δt_{13} between the first (charged) fragment and the second neutral one (hit #3). The grey curve corresponds to the mean histogram, named $<\Delta t>$. The blue dotted lines correspond to the simulated positions of the identified charged fragments.

2.3. Measurement of the branching ratios between the different relaxation channels

2.3.1. Measurement of the detection efficiency of neutral fragments

Different relaxation channels correspond to different peaks in the COINTOF mass spectra. In principle, branching ratios can be extracted from the ratios between the number of events in

the different peaks of the spectrum. However, the detection efficiency, i.e. the probability to detect or not the fragment, must be considered. Two different methods have been developed to measure the detection efficiency of neutral fragments.

The first method is related to the spatial separation between the charged fragments resulting from the relaxation of the parent cluster ion, and has been explained in detail in Thibaud Salbaing's PhD thesis, especially in the first chapter [4]. Such separation is achieved by applying a pusher voltage to the charged fragments resulting from the relaxation. This leads to a spatial separation of these charged fragments. The magnitude of the deflection is related to the mass of the charged fragment, the lighter it is the more it is deflected. The key point of this method is to compare, for a given charged fragment, the number of events for which the considered charged fragment is detected in correlation with the neutral fragment, to the total number of events in which the charged fragment has been detected. This method leads to the following measurements of detection efficiency: depending on their speed in the laboratory frame, the detection efficiency of the neutral methanol molecule CH_3OH ranges from 3.3% for 77.10^3m.s^{-1} to 31.8% for 154.10^3 m.s^{-1}, while that of neutral water molecules H_2O ranges from 3.4% for 92.10^3m.s^{-1} to 34.7% for 204.10^3 m.s^{-1}. Depending on the MCP detector, these detection efficiencies can vary up to $\pm$10% [4]. For the same velocity, the methanol molecule has a higher detection efficiency than the water molecule, and this is related to the mass difference between the two neutral fragments.

A distinct method, based on measured raw multiplicities, is proposed here and demonstrated with a data set associated with the relaxation of the protonated methanol dimer $H^+(CH_3OH)_2$. Unlike the pusher method, this method does not require additional data sets. Figure 12 shows parts of the COINTOF mass spectra associated with the relaxation of the protonated methanol dimer $H^+(CH_3OH)_2$. The mass spectra shown here are zoomed into the Δt range between 1150 ns to 1400 ns, associated with the daughter ion H^+. The upper plot corresponds to events with a raw multiplicity of 2 while the lower plot corresponds to events with a raw multiplicity of 3. The detection of H^+, resulting from the relaxation of $H^+(CH_3OH)_2$, can be related to the following dissociation process:

$$H^+(CH_3OH)_2 \rightarrow H^+ + CH_3OH + CH_3OH \quad (7)$$

The fit of the two experimental histograms is shown in Figure 12. A χ^2 minimisation is used to represent each histogram by a sum of Gaussian functions. The Gaussian functions, weighted by a proportionality factor, are given by the following equation:

$$f(\Delta t) = A \times \frac{1}{\sigma\sqrt{2\pi}} \times \exp\left(-\frac{1}{2}\frac{(\Delta t - \mu)^2}{\sigma^2}\right) \tag{8}$$

with A the proportionality factor, σ the variance, and μ the expected value.

The integral over the fit, for a given peak Δt, corresponds to the raw number of events, i.e. the number of events that have been detected. In the case of H^+ detection, $N_{d,2}^{H^+}$ corresponds to the raw number of events associated with a raw multiplicity of 2, and $N_{d,3}^{H^+}$ to the raw number of events associated with a raw multiplicity of 3. The ratio between the two raw number of events, $N_{d,2}^{H^+}$ and $N_{d,3}^{H^+}$, is related to the detection efficiency of the neutral fragments, $\epsilon_0^{H^+}$, detected in correlation with H^+. After a large number of successive measurements, the raw numbers of events are then related to a product of the probabilities of detecting some fragments and not detecting others. These probabilities are related to the detection efficiencies of the fragments. Equations (9) and (10) give the raw numbers of events as a function of the number of events that occurred during the experiment, the detection efficiencies, and the number of neutral fragments associated with the relaxation channel considered.

$$N_{d,2}^{H^+} = N_r^{H^+} \times \epsilon_c \times \epsilon_0^{H^+} \times \left(1\text{-}\epsilon_0^{H^+}\right)^{n-1} \tag{9}$$

$$N_{d,3}^{H^+} = N_r^{H^+} \times \epsilon_c \times \epsilon_0^{H^+} \times \epsilon_0^{H^+} \times \left(1\text{-}\epsilon_0^{H^+}\right)^{n-2} \tag{10}$$

with $N_{d,j}^{H^+}$ the raw number of events associated with the detection of the H^+ fragment with a raw multiplicity equal to j, $N_r^{H^+}$ the number of events that occurred during the experiment, ϵ_c the detection efficiency of the charged fragment H^+, $\epsilon_0^{H^+}$ the detection efficiency of the neutral fragments produced in correlation with the fragment H^+ i.e. the probability to detect one of these neutral fragments, and n the number of neutral fragments produced in correlation with the fragment H^+.

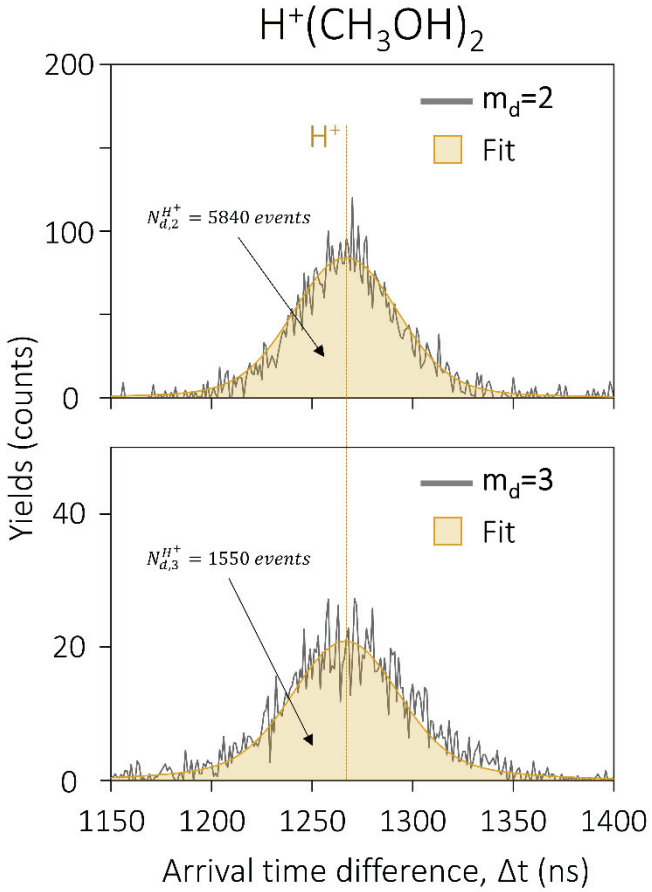

Figure 12: COINTOF mass spectra of the protonated methanol dimer $H^+(CH_3OH)_2$, accelerated to 8 keV, showing in detail the H^+ fragment area. Upper plot: histogram of the arrival time difference between a neutral fragment and the charged fragment Δt_{12} (grey curve) associated with the detection of a single neutral fragment. The fit of the H^+ peak is also plotted (yellow line), and the number of detected events corresponding to the integral of the fit is specified as 5840 events. Lower plot: mean histogram arrival time difference between the neutral fragments and the charged fragment, $<\Delta t>$, associated with the detection of two neutral fragments. The fit of the H^+ peak is also drawn (yellow line), and the number of detected events corresponding to the integral of the fit is specified as 1550 events.

The two raw numbers of event, described by Equations (9) and (10), can be combined to give an expression for the detection efficiency of the neutral fragments produced in correlation with the H^+ daughter ion. Equation (11) gives the expression of $\epsilon_0^{H^+}$ as a function of only the two raw event numbers, $N_{d,2}^{H^+}$ and $N_{d,3}^{H^+}$, independently of the detection efficiency of the charged fragment.

$$\epsilon_0^{H^+} = \left(1 + \frac{N_{d,2}^{H^+}}{N_{d,3}^{H^+}}\right)^{-1} \tag{11}$$

In the example presented in this section, the raw number of events with a raw multiplicity of 2 is about 5840 events, while the one associated with a raw multiplicity of 3 is about 1550 events, which leads to a detection efficiency of 21%. This value corresponds to the detection efficiency of the neutral fragments produced in correlation with the charged fragment H^+, during the experiment. This additional method is applied for the other neutral fragments of interest and the results are consistent with those obtained by other data set using the method presented previously, based on spatial separation. This earlier method, implemented in DIAM, is based on additional measurements using the pusher voltage. This requires additional specific data collection. The method developed here can be used directly on each data set without any additional measurements.

2.3.2. Measurement of branching ratios

A branching ratio is the probability of observing one specific relaxation channels among a group of observed channels. The value of a branching ratio is determined using the numbers of events that occurred during the experiment; for a given relaxation channel (i), it is denoted $N_r^{(i)}$. The calculation of $N_r^{(i)}$ is performed using the number of events associated with the channel (i) and with a raw multiplicity of 2, $N_{d,2}^{(i)}$, according to Equation (12):

$$\begin{aligned} N_{d,2}^{(i)} &= N_r^{(i)} \times \epsilon_c \times \epsilon_0^{(i)} \times \left(1\text{-}\epsilon_0^{(i)}\right)^{n-1} \\ \leftrightarrow N_r^{(i)} &= \frac{N_{d,2}^{(i)}}{\epsilon_c \times \epsilon_0^{(i)} \times \left(1\text{-}\epsilon_0^{(i)}\right)^{n-1}} \end{aligned} \tag{12}$$

with $N_{d,2}^{(i)}$ the raw number of events associated with the relaxation channel (i) and a raw multiplicity of 2, $N_r^{(i)}$ the number of events that occurred during the experiment, associated with the relaxation channel (i), ϵ_c the detection efficiency of the charged fragment of the relaxation channel (i), $\epsilon_0^{(i)}$ the detection efficiency of the neutral fragments of the channel (i), and n the number of neutral fragments associated with the relaxation channel (i).

The raw numbers of events, associated with a given relaxation channel, are calculated with the COINTOF spectra. The values of the detection efficiency can also be extracted from these spectra, as described above. The detection efficiency of the charged fragments does not depend on their mass, it is about 60%, which corresponds to the geometric detection efficiency of the MCP [5].

Considering all the different channels identified in a COINTOF mass spectrum, for the experiments that are presented in the following chapter, three groups of processes can be

identified: unimolecular reactions, evaporation processes, and fragmentation processes. Each of these groups may in addition contain several relaxation channels. A given group, denoted by (A), is associated with $N^{(A)}$, the number of events that occurred during the experiment associated to the group (A). $N^{(A)}$ is calculated by summing up the number of events associated with each relaxation channel which composes the group (A). The branching ratios are then determined according to the following equation:

$$BR^{(A)} = \frac{N^{(A)}}{\sum_{k=\{A,B,C,\ \ldots\}} N^{(k)}} \tag{13}$$

with $BR^{(A)}$ the value of the branching ratios associated with the process (A), $N^{(k)}$, the number of events that occurred during the experiment, associated with the process (k), and {A,B,C,…} all processes considered for this calculation of branching ratios.

The branching ratios (A), (B), and (C) are key quantities for discussing the relative contributions of these three groups in the context of the formation of large molecules under astrophysical conditions. Unimolecular reactions lead to the formation of larger, non-pre-existing molecules. The fragmentation group leads to the destruction of existing molecules, while the evaporation group leaves pre-existing molecules intact. Furthermore, the measured branching ratios, combined with the velocity distribution measurements, provide a framework for the quantitative description of the competition between relaxation channels.

2.4. Measurement of velocity distributions

The COINTOF-VMI method also allows to measure the velocity distribution of the neutral fragments for a selected relaxation channel. The velocity is determined from the spatial position of the neutral fragments on the detector. These impact positions of the fragments are measured via the delay line anode (DLA). Figure 13shows a schematic view of the principle of the DLA measurements. Each fragment detected on the MCP produces a cascade of electrons which is collected by the DLA and produces five electrical signals, one associated with the MCP and four with the DLA. The line associated with the vertical position is shown in red in Figure 13, while the one associated with the horizontal position is shown in blue. The arrival time difference between the two electrical signals at the two ends of a given line gives a measure of the horizontal (and vertical) position of the impact. The length of the lines and the propagation speed of the signal in the lines, v_s, are fixed [5]. This technique can detect the impact position of the fragment, x and y, with an accuracy of less than 0.1 mm. Equations (14) and (15) describe

the reconstruction of the impact position using the measured arrival time differences for each line in the DLA.

$$x = v_s\,(t_{DLA\_1} - t_{DLA\_2}) \tag{14}$$

$$y = v_s\,(t_{DLA\_3} - t_{DLA\_4}) \tag{15}$$

with t_{DLA_1}, t_{DLA_2}, t_{DLA_3} and t_{DLA_4} the propagation times of the electrical signals to the ends of each line. Endpoints 1 and 2 are associated with the x-position, while 3 and 4 with the y-position.

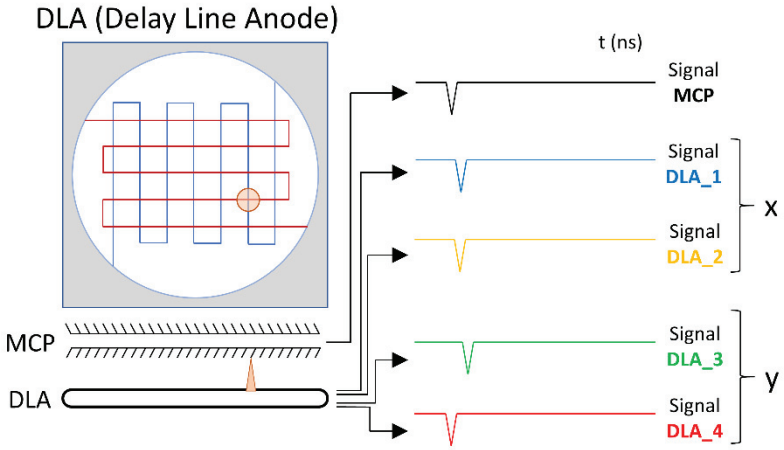

Figure 13: Measurement of the impact position from the DLA signals. The orange circle represents the impact of a fragment on the MCP. The impact causes a cascade of electrons, the orange cone, towards the DLA. The DLA is composed of 2 lines, the red line corresponds to the vertical position, y, and the blue line corresponds to the horizontal position, x. A well reconstructed impact corresponds to 5 measured times, induced by 5 electrical signals, 1 associated with the MCP, 2 with the horizontal position, and 2 with the vertical position.

Each fragment impact is associated with five electrical signals, and the multiparametric data set described above is used to select the neutral fragments. Measurements are performed for a large number of parent cluster ions, typically 10^6, leading to a position distribution of neutral fragments. This distribution is radially symmetric and can be reduced to a 1-dimensional distribution by introducing the variable R, the distance of a given impact from the centre of the neutral fragment distribution. The variable R is described by the following equation:

$$R = \sqrt{(x\text{-}x_0)^2 + (y\text{-}y_0)^2} \tag{16}$$

with x and y, the coordinates of the impact position and x_0 and y_0, the centre of the impact position distribution of the neutral fragments.

The impact position R of a neutral molecule on the detector is a direct consequence of the additional velocity of the neutral molecule obtained after dissociation of the parent cluster ion. Indeed, during dissociation, the kinetic energy release (KER) is distributed between the fragments due to the conservation of momentum. By this, the neutral fragment obtains an additional velocity, which is randomly oriented relative to the reference frame of the centre of mass associated with the parent ion. The position of the neutral fragment R is directly related to this additional velocity, V, gained during dissociation by the neutral fragment.

Determining the velocity distribution is an inverse problem, i.e. finding the causes of the observed consequences. The method developed here is based on Bayes' probability theorem. This allows the probability distribution of the causes to be measured as a function of the probability distribution of the effects, which in our case are, respectively, V and R. The unfolding method used here works iteratively to find the velocity distribution associated with the impact position distribution, measured on the detector. For each iteration, the probability of each velocity is adjusted, using a χ^2 minimisation method, between the simulated position distribution and the measured position distribution. A schematic view of the unfolding process is presented in Figure 14.

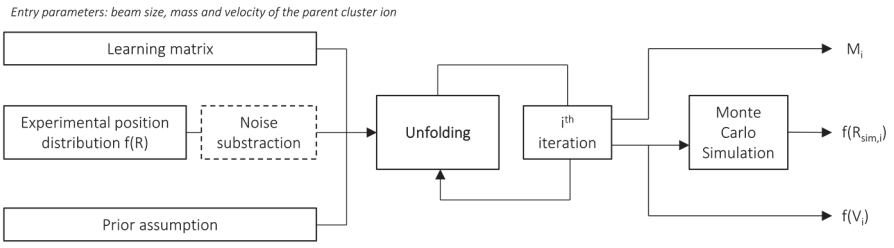

Figure 14: Schematic view of the velocity distribution reconstructed from the impact distribution of the neutral molecules. f(R) corresponds to the measured position distribution, $f(R_{sim,\,i})$ corresponds to the simulated position distribution obtained with the velocity distribution of iteration n°i, $f(V_i)$ corresponds to the velocity distribution of iteration n°i, and M_i corresponds to the matrix of iteration n°i.

Figure 14 shows that the unfolding algorithm starts with the construction of the learning matrix, which is performed using the Monte Carlo simulation of the experimental device. Each column of the learning matrix is associated with a bin of the velocity distribution and each row with a bin of the position distribution. The resolution of the position bin is fixed at 0.1 mm. This matrix depends on the velocity of the parent cluster ions. For each iteration, a new simulated position distribution is obtained, $f(R_{sim,i})$ and compared to the measured distribution. If the simulated distribution reproduces the measured distribution well, then the velocity distribution $f(V_i)$ is a good estimatation of the velocity distribution that induced the measured position distribution. Figure 15 shows the measured velocity distribution (yellow curve) of the neutral methanol molecule evaporated from the protonated methanol dimer $H^+(CH_3OH)_2$, after a collision

at 8 keV with an argon atom. In the insert, the measured position distribution (grey curve) and the simulated position distribution (yellow curve), associated with the velocity distribution plotted in the main plot, are drawn.

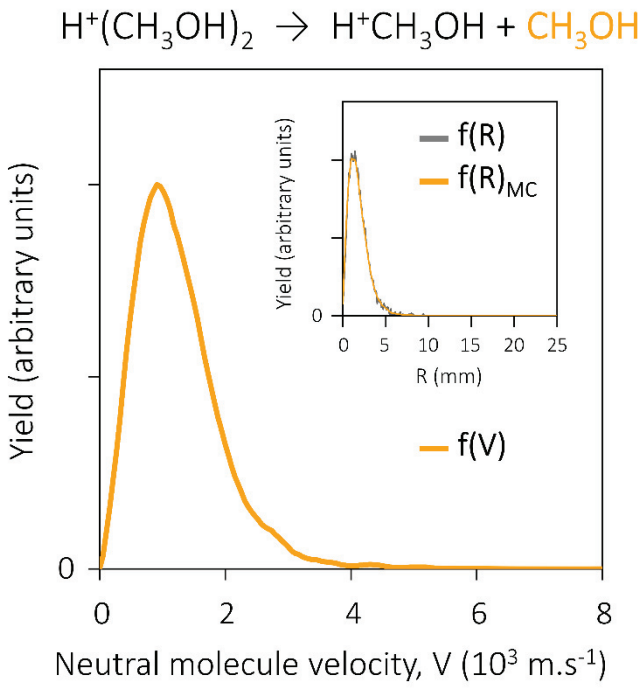

Figure 15: Velocity distribution of the methanol molecule evaporated from the protonated methanol dimer. The velocity distribution (yellow curve) is obtained from the impact distribution of the neutral molecule on the detector using an unfolding method. The insert shows the experimental impact distribution (grey curve) and the impact distribution calculated by Monte Carlo simulation from the velocity distribution extracted by the unfolding method (yellow curve).

The good agreement between the simulated position distribution $f(R)_{MC}$ and the measured position distribution f(R) validates the velocity distribution f(V) obtained by the unfolding process. The velocity distributions presented in this manuscript have successfully passed this validation process.

3. Theoretical tools

3.1. DFT calculations

Over the last few decades, density functional theory (DFT) calculations have been developed in many ways for many kinds of applications. DFT methods are used by quantum chemists, condensed matter physicists, and materials scientists to calculate material properties such as equilibrium geometry, quantum energy levels, vibrational properties, IR spectrum, etc.

DFT can be used for both molecular systems (of finite size) and extended periodic systems such as solids. In this thesis, we have studied a molecular system of finite size. However, the experimental conditions address truly dynamic situations as opposed to equilibrium properties that can be described quantitatively by DFT calculations. Nevertheless, such quantitative calculations are an essential reference point for a statistical description of the post-collisional relaxation of protonated molecular clusters.

The calculations are performed with the Gaussian 09D01 software [6]. The basis of these quantum chemical calculations is the solution of the Schrödinger equation in the Born-Oppenheimer approximation. This approximation consists of decoupling the motion of the nuclei from the motion of the electrons which are lighter and faster than the nuclei. The resulting system of many electrons moves in a fixed static potential associated with the given relative position of the nuclei. In DFT methods, the (many-body) problem of interacting electrons in a static potential is transformed into a solution of the problem of non-interacting electrons moving in an effective potential. At each major step of a Hartree-Fock calculation, a numerical integration of the functional (or different derivatives of the functional) is added by DFT. In DFT methods, the problem of finding the minimum electron energy is posed in terms of electron density. Analytical gradient methods allow the exploration of the resulting potential energy surface.

In this work, three methods were used: the Hartree-Fock (HF) level of theory and two DFT methods (B3 LYP [7] and M06 2X [8]). The basis set mainly used in this work is 6 311++G(2df,p). The structure and energetics of small molecular clusters in relation to the experimental work have been studied here. The products of the post-collision relaxation are also studied at the same level of theory. By exploring the potential energy surface, transition states (TS) between reactants and products have been revealed and reaction pathways have been obtained using the intrinsic reaction coordinates (IRC) method implemented in Gaussian09.

3.2. Statistical methods

Among the various relaxation processes observed in the DIAM experiments for the different protonated molecular clusters, the evaporation of a molecule is the main relaxation pathway. The statistical molecular dynamics (SMD) model, developed by Florent Calvo [9] [10], was used in addition to the experimental results for the velocity distribution of the evaporated molecules [11] [12]. Briefly, SMD simulations are performed using a flexible and polarisable potential [9] [13], but neglecting intermolecular proton transfer. In the simulations, the parent cluster ions are initially thermalised using molecular dynamics (MD) coupled to a Nosé-Hoover thermostat at 100 K. These configurations are used as starting points for constant energy MD trajectories. At the initial time, a random internal excitation energy, obtained from a flat

distribution in the range 2-8 eV, is converted into atomic kinetic energy. In doing so, a complete conversion of the excitation energy into vibration is assumed, as well as a complete statistical redistribution between all vibrational modes. All MD trajectories use a time step of 0.25 fs. After 1 ns, possible fragments are identified on the basis of distance criteria, and their kinetic energies are calculated. The events are sorted according to the number of evaporated molecules. By repeating the analysis on 10^5 independent trajectories for each parent protonated cluster, velocity distributions are obtained which can be compared with experimental results, assuming a complete redistribution of excitation energy. Note that the time window of the experiment (200 ns) is large compared to the time step needed to simulate the dynamics of the cluster (0.25 fs), so the simulations were done with a time window of 1 ns. Furthermore, SMD does not allow, in the simulation, the presence of chemical reactivity. This motivates the development of simple statistical models that can capture the essence of the phenomenon, without considering all the details of the dynamics and thus reducing the calculation time.

For a given amount of energy in the system, several trajectories are possible, each trajectory being associated with a particular evolution of the system. The phenomenon thus has a statistical behaviour and statistical methods can be used to study it. Several statistical models such as the phase space theory (PST) or the Rice Ramsperger Kassel Marcus (RRKM) theory have been developed earlier. These methods allow to calculate the relaxation time of a system and to calculate the KER distribution during the dissociation of the cluster. Their main feature is to study the isolated system with a given internal energy from the associated phase space, and the assumption of energy redistribution in this space. These models have been used for the evaporation of rare gas atom clusters to describe the kinetics of unimolecular reactions and the evaporation of atoms from fullerenes [14] [15] [16].

The PST theory used in this work is based on the redistribution of the internal energy of the reactant among its available phase space. Assuming reversibility between microscopic processes, equal probability is assumed for the given reaction and its corresponding inverse process. Therefore, the method does not require detailed knowledge of the microscopic processes, but requires that the internal dynamics of the reactant is fast enough to achieve a complete redistribution of energy in all internal degrees of freedom. The PST model leads to the Weisskopf formula:

$$k\,(E_T;\varepsilon)\,d\varepsilon = g\,\frac{m}{\pi^2\hbar^3}\,\sigma(\varepsilon)\,\varepsilon\,\frac{\rho_t\,(E_T\text{-}E_0\text{-}\varepsilon)}{\rho_r\,(E_T)}\,d\varepsilon \tag{17}$$

with $k\,(E_T;\varepsilon)$ the rate constant associated with the reaction for a value of the internal energy of the reactant E_T and a value of KER noted ε; E_0 the energy barrier associated with the reaction; $\rho_t(E_T\text{-}E_0\text{-}\varepsilon)$ the density of state of the products, for given values of E_T, ε and E_0; $\rho_r(E_T)$ the density of state of the reactant, for a given value of E_T; $\sigma(\varepsilon)$ is the effective

collision area between the products for a given value of ε; g a degeneracy factor characteristic of the reaction; m the reduced mass of the product system, and $\hbar$, the reduced Planck constant.

The reaction products consist of several atoms and therefore have internal degrees of freedom. The density of states associated with the two fragments is the convolution of the densities of states of the two products A and B:

$$\rho_t(E)=\int_0^E \rho_A(E-E_B)\rho_B(E_B)dE_B \tag{18}$$

In the framework of the Langevin's theory [17], the effective cross-section for such a system, with the approximation that the interaction is spherically symmetric, is defined by:

$$\sigma(\varepsilon)=\pi\left(\frac{2\alpha e^2}{\varepsilon}\right)^{\frac{1}{2}} \tag{19}$$

with α the isotropic polarizability of the neutral species and e the elementary charge.

This formula was originally developed for neutron evaporation from a nucleus by Weisskopf [18] and has been used to describe the evaporation process for atomic and molecular clusters recently. In particular, the KER distributions calculated with PST have been compared with those obtained by statistical molecular dynamics for the evaporation of atoms by argon clusters [16]. From Equation 17, by integration over all possible KER values, we obtain an expression for the reaction constant, and therefore the time constant, for a given internal energy. Integration over the distribution of internal energies of the reactant, while considering the energy barrier due to the transition state, gives the KER distribution. Thus, a model using the PST results for the rate constant and the KER distribution was developed to quantify the consequence of the internal energy redistribution assumption on the competition between the different relaxation pathways observed in the experiment. The model is constructed as a Monte Carlo simulation for a large number of parent cluster ions. The Beyer-Swinehart algorithm [19] is used to quickly calculate the density of state of a molecular system using the vibrational frequencies obtained by DFT calculations. The simulation considers several relaxation channels, the experimental time window, and the wide range of energy deposition characteristic of DIAM experiments. The model gives access, for each dissociation channel, to the KER distribution, the energy distribution of each fragment resulting from the relaxation of the parent cluster ion, as well as the branching ratios between the considered relaxation channels.

Conclusion

The DIAM device, described in this chapter, is used to study the statistical behaviour of the post-collisional relaxation of small protonated molecular clusters, after a single high energy collision with an argon atom. The short time scale of energy deposition and the wide range of the amount of energy deposited allow the observation of several relaxation channels. The COINTOF-VMI method allows the characterisation of these channels with measurements of the branching ratios between the dissociation channels and the velocity distribution of the neutral product. Several theoretical methods, density functional theory, statistical molecular dynamics, and phase space theory are used in combination with the different tools developed to analyse the multiparametric data sets of the experiments.

Bibliography

[1] G. Bruny et al., "A new experimental setup designed for the investigation of irradiation of nanosystems in the gas phase: A high intensity mass-and-energy selected cluster beam," *Rev. Sci. Instrum.*, vol. 83, p. 013305, January 2012.

[2] G. Bruny, "Production et caractérisation d'agrégats moléculaires protonés contenant un nombre donné de molécules d'eau auprès de dispositif DIAM," Université Claude Bernard Lyon 1, Ph.D. dissertation 2010. theses.fr/2010LYO10270

[3] F. Berthias et al., "Measurement of the velocity of neutral fragments by the "correlated ion and neutral time of flight" method combined with "velocity-map imaging"," *Rev. Sci. Instrum.*, vol. 88, p. 083101, August 2017.

[4] T. Salbaing, "Thermalisation dans une nanogoutte : évaporation versus réactivité," Université Claude Bernard Lyon 1, Ph.D. dissertation 2019. theses.fr/2019LYSE1163

[5] RoentDek, "MCP Delay Line Detector Manual version 11.0.1607.2,". roentdek.com/manuals/MCP Delay Line manual.pdf

[6] M. J. Frisch et al., "Gaussian 09 (Revision D.01)," 2009. rsc.org/suppdata/c5/sc/c5sc02423d/c5sc02423d1.pdf

[7] A. D. Becke, "A new mixing of Hartree-Fock and local density-functional theories," *J. Chem. Phys.*, vol. 98, pp. 1372–1377, January 1993.

[8] Y. Zhao and D. G. Truhlar, "The M06 suite of density functionals for main group thermochemistry, thermochemical kinetics, noncovalent interactions, excited states, and transition elements: two new functionals and systematic testing of four M06-class functionals and 12 other functionals," *Theor. Chem. Acc.*, vol. 120, pp. 215–241, July 2007.

[9] M. Marciante and F. Calvo, "Modelling infrared action spectra of protonated water clusters," *Mol. Simul.*, vol. 40, pp. 176–184, December 2013.

[10] Florent Calvo et al., "Collision-induced evaporation of water clusters and contribution of momentum transfer," *Eur. Phys. J. D*, vol. 71, May 2017.

[11] F. Berthias, "Thermalisation dans une nanogoutte d'eau," Université Claude Bernard Lyon 1, Ph.D. dissertation 2016. theses.fr/2016LYSE1164

[12] H. Abdoul-Carime et al., "Velocity of a Molecule Evaporated from a Water Nanodroplet: Maxwell-Boltzmann Statistics versus Non-Ergodic Events," *Angew. Chem. Int. Ed.*, vol. 127, pp. 14898–14902, October 2015.

[13] G. Brancato and M. E. Tuckerman, "A polarizable multistate empirical valence bond model for proton transport in aqueous solution," *Chem. Phys.*, vol. 122, p. 224507, June 2005.

[14] K. Hansen, *Statistical Physics of Nanoparticles in the Gas Phase*, Springer, Ed., 2013.

[15] T. Baer and W. L. Hase, *Unimolecular Reaction Dynamics: Theory and Experiments*, Oxford University Press, Ed., 1996.

[16] S. Weerasinghe and F. G. Amar, "Absolute classical densities of states for very anharmonic systems and applications to the evaporation of rare gas clusters," *Chem. Phys.*, vol. 98, pp. 4967–4983, March 1993.

[17] Brian R. Eichelberger, Theodore P. Snow, and Veronica M. Bierbaum, "Collision rate constants for polarizable ions," *J. Am. Soc. Mass Spectrom.*, vol. 14, pp. 501–505, May 2003.

[18] V. Weisskopf, "Statistics and Nuclear Reactions," *Phys. Rev.*, vol. 52, pp. 295–303, August 1937.

[19] T. Beyer and D. F. Swinehart, "Algorithm 448: number of multiply-restricted partitions," *Commun. ACM*, vol. 16, p. 379, June 1973.

Chapter III

Competition between post-collisional relaxation pathways of protonated molecular dimers and clusters

This chapter is dedicated to the experimental results obtained with DIAM, on the post-collisional relaxation of small protonated molecular clusters, and in particular, the competition between several processes. The chapter is divided into three main parts, the first one concerns the study of the protonated pyridine dimer, the second one the study of the protonated methanol dimer, and the last one the study of protonated glycine clusters.

1. The protonated pyridine dimer: evaporation without fragmentation or with fragmentation

1.1. Analysis of the COINTOF spectra of charged fragments

As described in Chapter II, the DIAM device allows the production of pyridine clusters and in particular the protonated pyridine dimer $H^+(Pyr)_2$. The results presented below were obtained with a beam of protonated pyridine dimers accelerated to 8 keV, and considering the mass of the cluster, 159 amu, this corresponds to a velocity in the laboratory frame of 98.5×10^3 m.s^{-1}.

Figure 16 shows the COINTOF mass spectra of the charged fragments induced by the relaxation of the protonated pyridine dimer after a collision with an argon atom. The upper plot shows events with a raw multiplicity, m_d, of 2 and the lower plot events with a raw multiplicity of 3. The COINTOF mass spectra are plotted as a function of the arrival time difference between the charged fragment and the detected neutral fragment, for events with m_d=2, or between the charged fragments and the two detected neutral fragments, for events with m_d=3. These arrival time differences are characteristic of the mass of the charged fragments (see Chapter II). In the case of the protonated pyridine dimer $H^+(Pyr)_2$, 6 charged fragments are identified corresponding to the 6 peaks in the COINTOF mass spectra. The first peak is associated with the detection of the protonated pyridine H^+Pyr (cyan and dark blue area), and the peak maximum lies at an arrival time difference of 405 ns. In addition, five other daughter ions were detected, $C_4H_4H^+$ (magenta area), $C_3H_3^+$ (orange area), $HCNH^+$ (green area), CH^+ (light blue area), and H^+ (gold area), associated with arrival time differences of 562, 680, 860 and 2260 ns, respectively.

In the upper plot, associated with a raw multiplicity, m_d, of 2, a distinction is made between events corresponding to the evaporation process without fragmentation (dark blue area) and events corresponding to the evaporation of the pyridine molecule with fragmentation (cyan area). The evaporation process of a pyridine molecule is the dominant process. In the two COINTOF mass spectra (upper and lower plot), distinguished by the raw multiplicity of events (m_d=2 or m_d=3), 5 other peaks are also observed, corresponding to the fragmentation of the molecular ion H^+Pyr. In the following, a distinction will be made between evaporation events without fragmentation (dark blue area, only upper plot of Figure 16) and fragmentation events of one of the two pyridine dimer molecules (all the area except dark blue area, upper and lower plot of Figure 16).

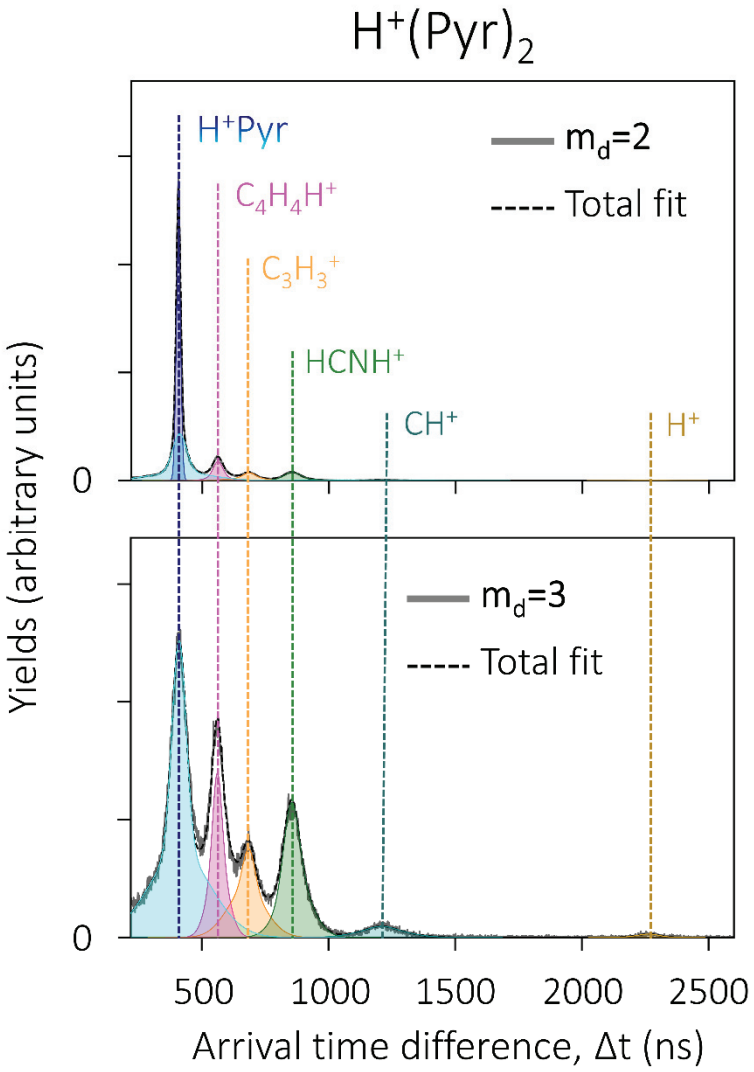

Figure 16: COINTOF mass spectra of the protonated pyridine dimer $H^+(Pyr)_2$ (accelerated to 8 keV), corresponding to $H^+(C_5H_5N)_2$, induced by a single collision with an argon atom. Upper plot: histogram of the arrival time difference between the charged fragment and the neutral fragment Δt_{12} (grey curve). In this case, dissociation events selected to construct the histogram correspond to the detection of 2 fragments (m_d=2). The fit of the histogram is also drawn (black dotted line), and it consists of 7 contributions (filled coloured curves), each of them described by a sum of Gaussian functions. The first peak groups the evaporation events without fragmentation (dark blue area) and with fragmentation (cyan area) of the neutral pyridine molecule. Lower plot: histogram of the arrival time difference between the charged fragment and neutral ones, $<\Delta t>$. In this case, dissociation events which have been selected correspond to the detection of 3 fragments (m_d=3). The fit of the histogram is also drawn (black dotted line), and it consists of 6 contributions (filled coloured curves), each of them described by a sum of Gaussian functions. The coloured dotted lines correspond to the simulated positions of the identified charged fragments.

1.2. Evaporation without fragmentation versus fragmentations of one of the two pyridine molecules

1.2.1. The detection of H^+Pyr

The COINTOF mass spectra obtained, according to the raw multiplicity of events, allows us to distinguish the relaxation channels. Thus, the detection of the molecular ion H^+Pyr is associated with the evaporation of one of the two molecules of the dimer, but its detection for a raw multiplicity equal to 3 shows that the evaporated molecule can be fragmented in the observation time window. Thus, two types of relaxation channels, associated to the detection of H^+Pyr, can be distinguished. The first relaxation channel corresponds to the evaporation without fragmentation of the evaporated molecule (dark blue area) as described by the following equation:

$$H^+(Pyr)_2 \rightarrow H^+Pyr + Pyr \quad (1)$$

This channel leads to events with a multiplicity of 2, i.e. to the production of 2 fragments, and cannot contribute to the second COINTOF mass spectrum associated with a raw multiplicity of 3. Then, the second type of relaxation channels corresponds to the detection of 2 neutral fragments, correlated with the detection of H^+Pyr. Here, the proton remained on the molecule which does not fragment.

Figure 17 shows a zoom of Figure 16, and it details the contributions associated with the detection of H^+Pyr. The fit of the experimental histogram highlights the presence of three contributions in this peak, evaporation without fragmentation of the evaporated molecule (dark blue area), and with fragmentation of the evaporated molecule (cyan area). The evaporation with fragmentation of the neutral molecule is composed of 2 contributions (dotted cyan curves).

As shown in Chapter II, the comparison between the evolution of these 2 contributions between (m_d=2) and (m_d=3) gives information about the observed neutral fragments. Considering the existence of two contributions, one larger than the other, and the associated detection efficiency measurements, the H^+Pyr contribution, present in the (m_d=2) and (m_d=3) spectra, is mainly associated with the presence of two types of neutral fragments that are different, in term of mass. Considering the experimental results on the fragmentation of neutral and protonated pyridine [1] [2], the COINTOF mass spectra, presented above, show that the fragmentation of neutral pyridine can be related to the formation of neutral fragments C_4H_4 (52 amu) and HCN (27 amu). The relaxation channel associated with the evaporation with fragmentation of the molecule can be written according to the following equation:

$$H^+(Pyr)_2 \rightarrow H^+Pyr + C_4H_4 + HCN \quad (2)$$

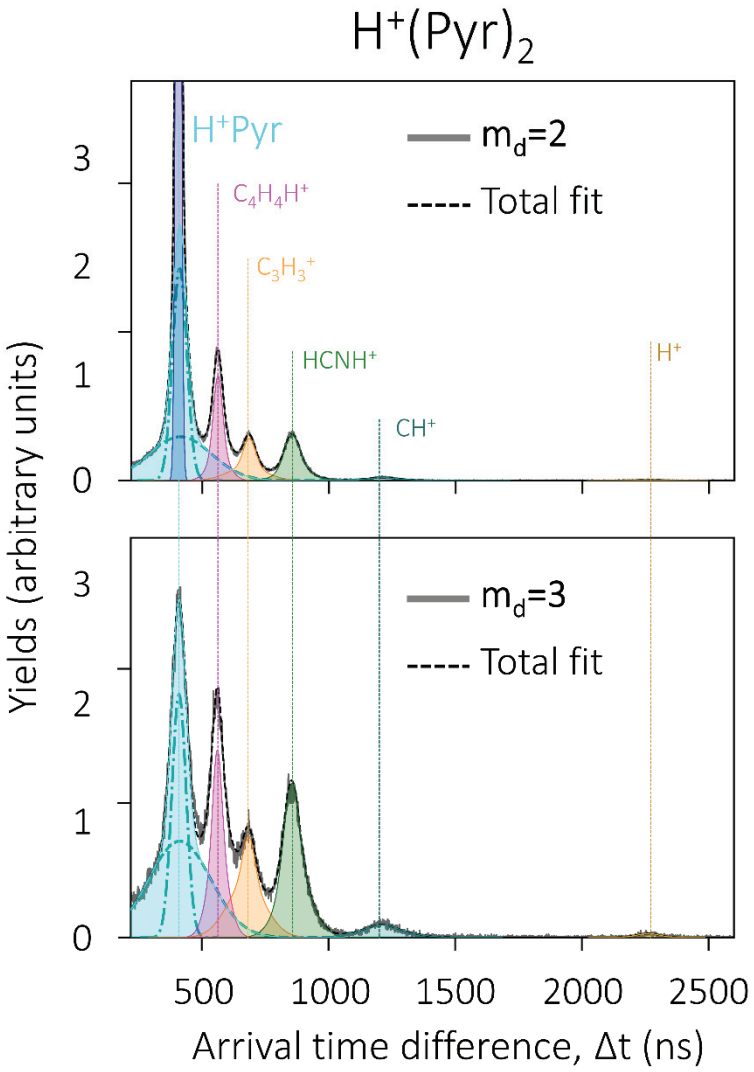

Figure 17: Zoom of Figure 16: COINTOF mass spectra of the protonated pyridine dimer (accelerated to 8 keV) showing the two contributions in the H^+Pyr peak with fragmentation of the neutral pyridine. Upper plot: histogram of the arrival time difference between the charged fragment and the neutral fragment Δt_{12} (grey curve). In this case, dissociation events selected to construct the histogram correspond to the detection of 2 fragments (m_d=2). The fit of the histogram is also drawn (black dotted line), and it consists of 7 contributions (filled coloured curves), each of them described by a sum of Gaussian functions. The first peak groups the evaporation events without fragmentation (dark blue area) and with fragmentation (cyan area) of the neutral pyridine molecule. Lower plot: histogram of the arrival time difference between the charged fragment and neutral ones, $<\Delta t>$. In this case, dissociation events which have been selected correspond to the detection of 3 fragments (m_d=3). The fit of the histogram is also drawn (black dotted line), and it consists of 6 contributions (filled coloured curves), each of them described by a sum of Gaussian functions. The coloured dotted lines correspond to the simulated positions of the identified charged fragments. In both graphs, the two Gaussian functions that represent the contribution associated with the detection of H^+Pyr correlated to the fragmentation of the evaporated molecule are drawn (dashed and dotted cyan curves).

1.2.2. The fragmentation of H^+Pyr without fragmentation of the neutral pyridine molecule

The fragmentation of H^+Pyr groups together all the events where a charged fragment with a mass lower than that of pyridinium is observed. Two neutral fragments are usually associated with these charged fragments. Consequently, one of the two neutral molecules, is not fragmented.

In addition to the detection of H^+, the charged fragments observed are associated to the 4 peaks in the COINTOF mass spectrum in Figure 16. They correspond to $C_4H_4H^+$, $C_3H_3^+$, $HCNH^+$ and CH^+ ions. Figure 18 shows a zoom of Figure 16, detailing the contribution associated with the detection of $HCNH^+$. The fitting of the experimental histogram shows the presence of 2 contributions in this peak (green dashed curves).

The shape of the peak in the COINTOF mass spectra brings us information about the neutral fragments. Indeed, the width of a given contribution, i.e. a Gaussian function in this case, is related to the mass of the neutral fragment associated with this contribution. The existence of two different contributions, with two distinct widths, shows that the charged $HCNH^+$ fragment (green peak in the spectra) is detected in correlation with at least two different neutral fragments, in term of mass.

Another impact of the mass difference between the neutral fragments is a difference in term of detection efficiency. As described in Chapter II, the proportionality factor between the contribution (m_d=3) and the contribution (m_d=2) is related to the detection efficiency. The two contributions associated with $HCNH^+$, correspond to detection efficiencies of 20% for the larger one, consistent with the pyridine molecule, and 11% for the smaller one, consistent with a lower mass fragment than the Pyr molecule.

Thus, the results show that the charged $HCNH^+$ fragment is produced in correlation with at least two different neutral fragments, as a pyridine molecule and a neutral molecule resulting from the fragmentation of H^+Pyr. The presence of the daughter ion $HCNH^+$ can be linked to the dissociation process described by the following equation:

$$H^+(Pyr)_2 \rightarrow HCNH^+ + C_4H_4 + Pyr \quad (2)$$

The same analysis was done for the other peaks associated with H^+Pyr fragmentation. On the one hand, the detection efficiency of the largest neutral fragment, detected in correlation with the charged fragment, for each of these peaks is 12%, 15% and 21%, for $C_4H_4H^+$, $C_3H_3^+$ and CH^+, respectively. On the other hand, the detection efficiency of the smallest neutral fragment,

detected in correlation with the charged fragment, for each of these peaks is 6%, 7% and 9% for $C_4H_4H^+$, $C_3H_3^+$ and CH^+, respectively.

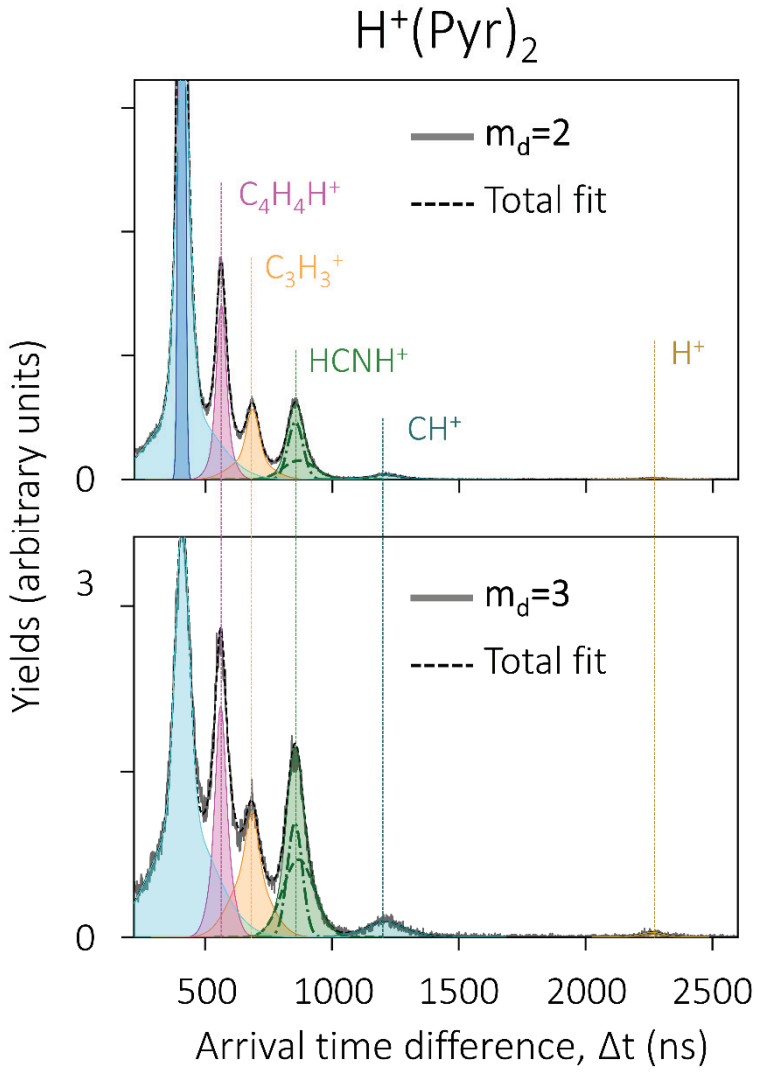

Figure 18: Zoom of Figure 16: COINTOF mass spectra of the protonated pyridine dimer (accelerated to 8 keV) showing the two contributions in the $HCNH^+$ peak with fragmentation of the neutral pyridine. Upper plot: histogram of the arrival time difference between the charged fragment and the neutral fragment Δt_{12} (grey curve). In this case, dissociation events selected to construct the histogram correspond to the detection of 2 fragments (m_d=2). The fit of the histogram is also drawn (black dotted line), and it consists of 7 contributions (filled coloured curves), each of them described by a sum of Gaussian functions. The first peak groups the evaporation events without fragmentation (dark blue area) and with fragmentation (cyan area) of the neutral pyridine molecule. Lower plot: histogram of the arrival time difference between the charged fragment and neutral ones, $<\Delta t>$. In this case, dissociation events which have been selected correspond to the detection of 3 fragments (m_d=3). The fit of the histogram is also drawn (black dotted line), and it consists of 6 contributions (filled coloured curves), each of them described by a sum of Gaussian functions. The coloured dotted lines correspond to the simulated positions of the identified charged fragments. In both graphs, the two Gaussian functions that represent the contribution associated with the detection of $HCNH^+$ and neutral fragments are drawn (dashed and dotted green curves).

1.3. The branching ratios between relaxation channels

The combined analysis of the multiparametric data set led to the determination of branching ratios between the three relaxation processes presented previously, namely: evaporation without fragmentation, fragmentation of the pyridinium ion, and fragmentation of the neutral molecule. Table 1 gives the branching ratios between these three relaxation channels, induced by the single collision between a protonated pyridine dimer and an argon atom. These branching ratios are extracted according to the method detailed in Chapter II.

$H^+(Pyr)_2$

Relaxation channel	Evaporation without fragmentation	Fragmentation of pyridinium ion	Fragmentation of the neutral molecule (pyridinium ion intact)
Branching Ratio	0.14 ± 0.04	0.30 ± 0.05	0.56 ± 0.06

Table 1: Branching ratios between the relaxation channels of the protonated pyridine dimer.

After a single collision with an argon atom, at high velocity, the relaxation of the protonated pyridine dimer led to evaporation without fragmentation of the neutral pyridine molecule in 14% of the observed events, fragmentation of the pyridinium molecular ion in 30% of the observed events, and fragmentation of the neutral molecule in 56% of the events. In the case of fragmentation of the H^+Pyr molecular ion, $C_4H_4H^+$ represents 46% of the events, $CH_3H_3^+$ corresponds to 31% of the events, $HCNH^+$ to 20%, CH^+ to 3% and H^+ to less than 1%.

1.4. The detection of H^+

The COINTOF method allows us to detect the smallest possible charged fragment, an H^+ proton, resulting from the relaxation of the parent cluster ion. Figure 19 shows a zoom of Figure 16, showing the region corresponding to the detection of the proton H^+ as charged fragment. In this figure, two peaks are visible, the one associated with the detection of CH^+ and the one associated with the detection of H^+.

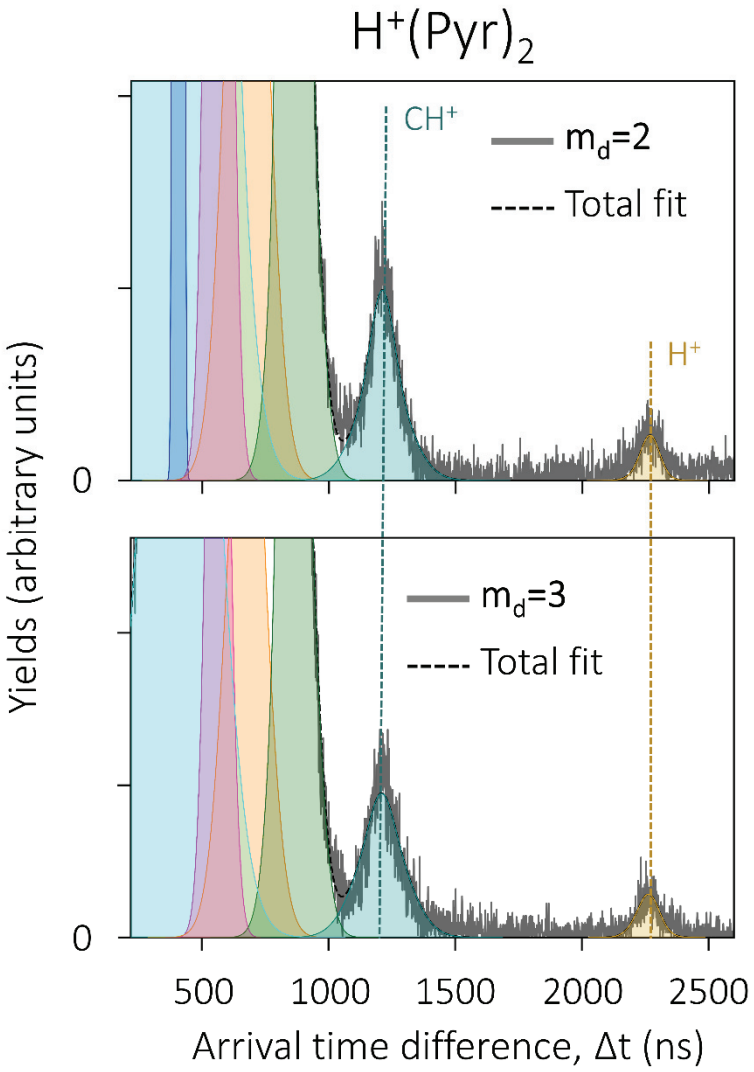

Figure 19: Zoom of Figure 16: COINTOF mass spectra of the protonated pyridine dimer accelerated to 8 keV. In both plots, only the peaks associated with the detection of H^+ (gold filled curve) and CH^+ (light blue filled curve) are fully visible. Upper plot: histogram of the arrival time difference between the charged fragment and the neutral fragment Δt_{12} (grey curve). In this case, dissociation events selected to construct the histogram correspond to the detection of 2 fragments (m_d=2). Lower plot: histogram of the arrival time difference between the charged fragment and neutral ones, $<\Delta t>$. In this case, dissociation events which have been selected correspond to the detection of 3 fragments (m_d=3). The coloured dotted lines correspond to the simulated positions of the identified charged fragments.

The presence of the charged fragment H^+, at a raw multiplicity of 2 and at a raw multiplicity of 3, shows that H^+ is associated with events exhibiting a multiplicity of at least 3. The similarities in term of shape, between the peak at (m_d=2) and (m_d=3) show that, in majority, the two neutral fragments are close, in term of mass. The measured detection efficiency of the neutral fragments, detected in correlation with H^+, is about 21.6%. This value is consistent with the expected detection efficiency of a neutral pyridine accelerated to 98.5×10^3 m.s^{-1}. This means

that H^+ is mainly detected in correlation with two neutral fragments of the same mass, with a detection efficiency consistent with a neutral pyridine. In other words, H^+ seems to be mainly detected in correlation with two pyridine molecules. The presence of the daughter ion H^+ is then related to the dissociation process described by the following equation:

$$H^+(Pyr)_2 \rightarrow H^+ + Pyr + Pyr \quad (3)$$

The results obtained for the protonated pyridine dimer have been presented here as an example with no reactivity. In the following, we present the results for methanol and glycine protonated dimers for their astrophysical interest, as presented in Chapter I.

2. The protonated methanol dimer: evaporation versus water elimination reaction

2.1. The post-collisional relaxation channels

Methanol CH_3OH is the simplest alcohol and the protonated methanol dimer consists of one proton and two molecules with a binding energy of 1.51 eV [3]. Beams of protonated methanol dimers, $H^+(CH_3OH)_2$, are produced by DIAM, at an acceleration energy of 8 keV. Given the mass of the cluster, 65 amu, it corresponds to a velocity in the laboratory frame of 15.4×10^4 m.s^{-1}. Figure 20 shows the COINTOF mass spectra of the charged fragments induced by the relaxation of the protonated methanol dimer after a single collision with an argon atom. The upper plot is associated to events with a raw multiplicity of 2 and the lower plot, to events with a raw multiplicity of 3. The COINTOF mass spectra correspond to the arrival time difference between the charged fragment and the detected neutral fragment, for events with (m_d=2), or between the charged fragments and the two detected neutral fragments, for events with (m_d=3). These differences in arrival times are characteristic of the mass of the charged fragments. In the case of the protonated methanol dimer $H^+(CH_3OH)_2$, 4 charged fragments are identified corresponding to the 4 peaks in the COINTOF mass spectra. The first peak is associated with the detection of protonated methanol H^+CH_3OH, and the maximum of the peak corresponds to a time difference of arrival of 252 ns. In addition, three other daughter ions were detected, $(CH_3)_2OH^+$ (red area), CH_3^+ (magenta area) and H^+ (gold area), associated with arrival time differences of 192, 455, and 1267 ns, respectively.

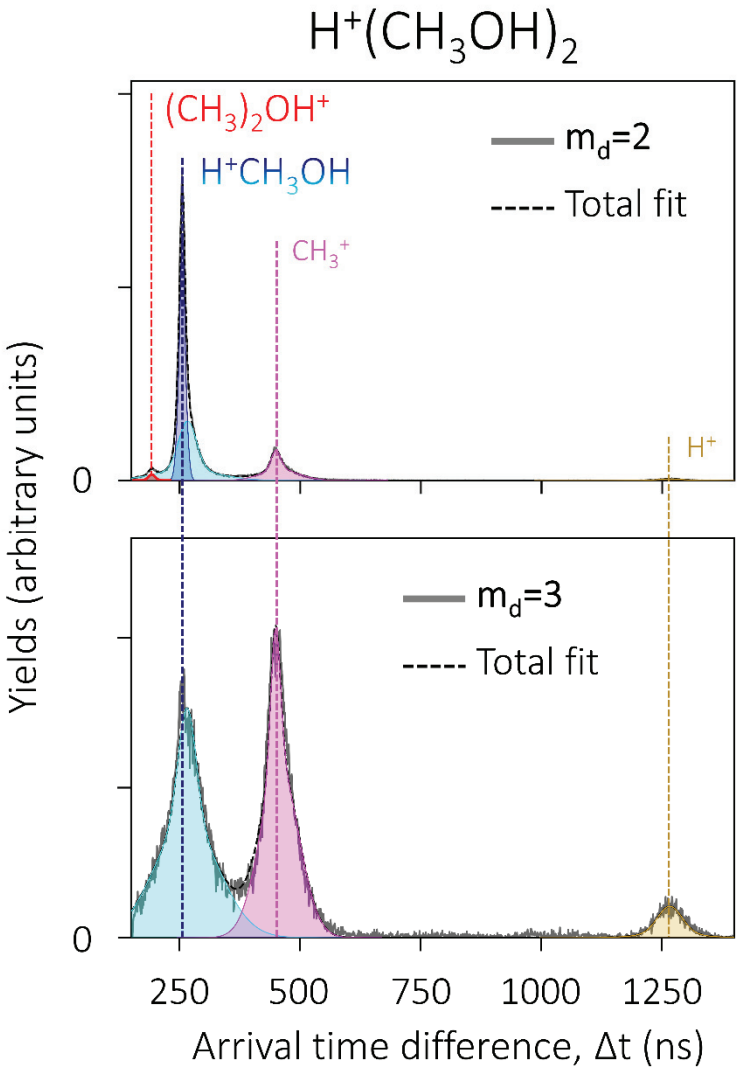

Figure 20: COINTOF mass spectra of the protonated methanol dimer $H^+(CH_3OH)_2$ (accelerated at 8 keV), induced by a single collision with an argon atom. Upper plot: histogram of the arrival time difference between the charged fragment and the neutral fragment Δt_{12} (grey curve). In this case, dissociation events selected to construct the histogram correspond to the detection of 2 fragments (m_d=2). The histogram fit is also drawn (black dotted line), and it consists of 4 contributions (coloured areas), each of them described by a sum of Gaussian functions. Lower plot: histogram of the arrival time difference between the charged fragment and neutral ones, $<\Delta t>$. In this case, dissociation events which have been selected correspond to the detection of 3 fragments (m_d=3). The fit of the histogram is also drawn (black dotted line), and it consists of 3 contributions (coloured areas), each of them described by a sum of Gaussian functions. The coloured dotted lines correspond to the simulated positions of the identified charged fragments.

The main contribution is associated with the evaporation process, without fragmentation (dark blue area) or with fragmentation (light blue area) of the evaporated methanol molecule. In the COINTOF mass spectra associated to a raw multiplicity of 2, three other peaks were also detected. One of these three peaks, corresponds to the fragmentation of the protonated methanol leading to the detection of CH_3^+, a charged fragment with a lower mass than the protonated methanol. A second peak of lower abundance, represented in red, corresponds to the detection of

a charged fragment of greater mass than the protonated methanol. It is associated to the reaction process between the two initial components of the parent cluster ion leading to the formation of the protonated dimethyl ether $(CH_3)_2OH^+$ via the elimination of a water molecule.

As in the case of $H^+(Pyr)_2$, the COINTOF method allows us to detect the smallest possible charged fragment, the H^+ ion, resulting from the relaxation of the parent cluster ion. The presence of this charged fragment is clear in the two mass spectra in Figure 20. The presence of this peak, in the spectrum associated with a raw multiplicity of 2 and in the spectrum associated with a raw multiplicity of 3, shows that H^+ is associated to events with a multiplicity of at least 3. The similarities, in term of shape, between the peak at (m_d=2) and (m_d=3) support the fact that, in the majority of cases, the two neutral fragments are close, in term of mass. The calculated detection efficiency of the neutral fragments detected in correlation with H^+ is about 22.9%. This value is consistent with the expected detection efficiency of a neutral methanol accelerated to 15.4×10^4 m.s^{-1}. This means that H^+ is mainly detected in correlation with two neutral fragments of the same mass, with a detection efficiency consistent with neutral methanol. The presence of the daughter ion H^+ is then mainly related to the dissociation process described by the following equation:

$$H^+(CH_3OH)_2 \rightarrow H^+ + CH_3OH + CH_3OH \quad (4)$$

2.2. The water elimination reaction

2.2.1. The velocity distribution of the eliminated water molecule

Unlike the protonated pyridine dimer, one of the relaxation channels of the protonated methanol dimer $H^+(CH_3OH)_2$, after a single collision with an argon atom, is the reaction leading to the formation of protonated dimethyl ether $(CH_3)_2OH^+$. The COINTOF-VMI method, described in Chapter II, allows us to characterise this reaction, by measuring the velocity distribution of the eliminated water molecule.

The events corresponding to the elimination reaction of a water molecule are represented in red in the COINTOF mass spectrum associated to events with a raw multiplicity of 2 in Figure 20. The contribution of this reaction was only observed for a raw multiplicity of 2. Indeed, the water loss reaction is described by the following equation:

$$H^+(CH_3OH)_2 \rightarrow (CH_3)_2OH^+ + H_2O \quad (5)$$

The COINTOF-VMI method allows the velocity distribution of neutral fragments to be measured. In the case of the elimination reaction of a water molecule, the velocity distribution of the eliminated water molecule can be measured. Figure 21 shows the measured velocity

distribution of the eliminated water molecule (solid red curve, upper plot in Figure 21). The lower plot shows the velocity distribution of the unfragmented evaporated methanol molecule (solid orange curve, lower plot in Figure 21).

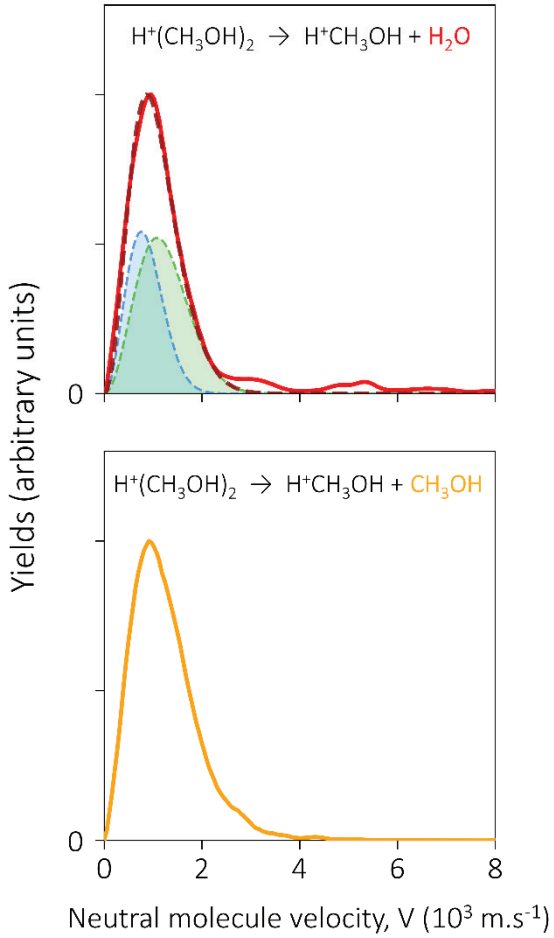

Figure 21: Upper plot: experimental velocity distribution (red solid line) of the water molecule eliminated by the protonated methanol dimer (accelerated at 8 keV), after a collision with an argon atom. The fit of the experimental distribution is also drawn (red dotted line) and consists of two Maxwell-Boltzmann distributions (blue and green dotted lines). Lower plot: experimental velocity distribution (orange solid line) of the unfragmented methanol molecule evaporated by the protonated methanol dimer.

The velocity distribution of the eliminated water molecule is mainly composed of a contribution between 0 and 2×10^3 m.s^{-1}. The maximum of this contribution is located at about 9.5×10^2 m.s^{-1}. The experimental distribution of the water molecule is composed of two Maxwell Boltzmann distributions (blue area and green area, upper plot). The presence of these two Maxwell Boltzmann contributions in the experimental velocity distribution led to the development of theoretical calculations based on density functional theory, in order to determine the reaction pathways for the formation of the protonated dimethyl ether $(CH_3)_2OH^+$, from the protonated methanol dimer $H^+(CH_3OH)_2$.

2.2.2. Identification of two transition states associated with the water elimination reaction

Previous calculations on this system have shown the presence of a transition state associated with this reaction. This transition state was proposed by Graul *et al.* [4] and calculated by Bouchoux and Choret [5]. However, the existence of this transition state alone is not sufficient to explain the two Maxwell-Boltzmann contributions in the experimental velocity distribution. Calculations have been carried out in the IPM team to explore the presence of other possible transition states. Figure 22 shows the calculated energy diagram for the $H^+(CH_3OH)_2$ elimination reaction. The DFT calculations were performed at the M062x level, using the 6 311++G(2df,p) basis set. The structures shown in Figure 22 are optimised to their lowest potential energy level. The reference (0.0 eV) corresponds to the lowest energy structure of the protonated methanol dimer. The other energy levels are given relative to this reference.

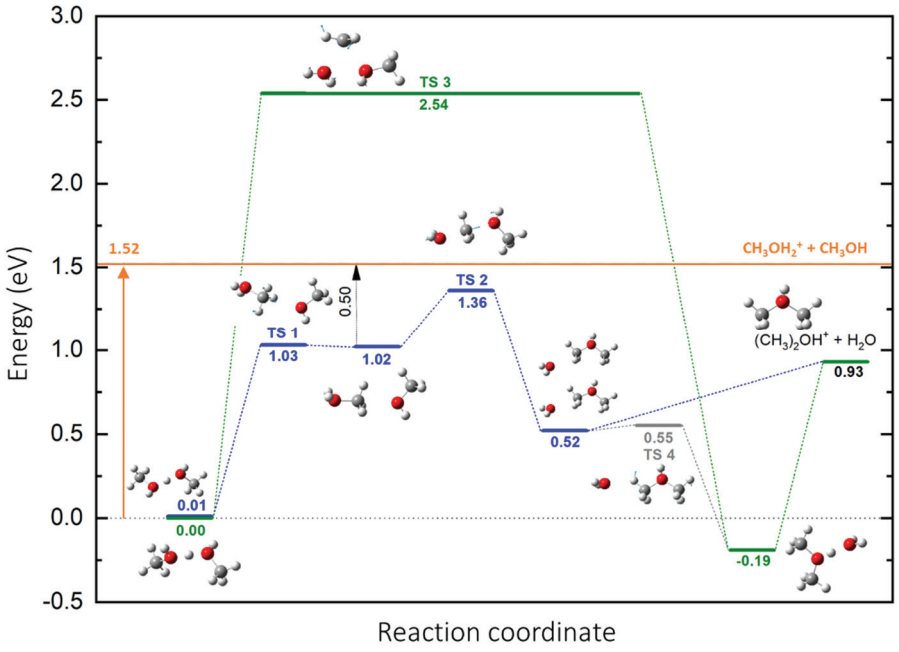

Figure 22: Energy diagram calculated by DFT (M06-2X/6-311G++(2df,p)) for the formation of protonated dimethyl ether $(CH_3)_2OH^+$ from a protonated methanol dimer $H^+(CH_3OH)_2$. The energy calculations consider the zero point energy. The structures associated with the energies are shown in the figure. The energy reference corresponds to the ground state of the $H^+(CH_3OH)_2$ cluster. The orange vertical arrow represents the evaporation process of a methanol molecule from the cluster.

The transition state highlighted by Bouchoux and Choret [5] has been confirmed and is shown in blue in the diagram (TS2). The associated energy level is 1.36 eV. The final state corresponds to an energy of 0.93 eV. In comparison, evaporation requires an energy of 1.52 eV to occur (orange arrow and orange line in Figure 22). Thus, TS2 requires 0.59 eV less than the evaporation process of a methanol molecule.

Calculations carried out in the IPM team have revealed the presence of another transition state (TS3). This transition state is represented in green in the energy diagram and is located at 2.54 eV. The presence of this second transition state could explain the presence of both Maxwell-Boltzmann contributions in the experimentally measured velocity distribution. In addition, TS3 is 1.18 eV above TS2. In the case of the green pathway, the energy barrier to be overcome is higher than that associated with the blue pathway. The excitation energy must be higher to pass through TS3.

2.3. Evaporation with or without fragmentation of the molecules

2.3.1. The detection of H^+CH_3OH

The detection of H^+CH_3OH is associated with an evaporation process of a methanol molecule. This process leads to the observation of two types of events. The first type corresponds to the evaporation without fragmentation of the evaporated molecule during the time left for relaxation before analysis of the fragments. The second type corresponds to the detection of pyridinium with fragmentation of the neutral molecule, CH_3OH. The COINTOF mass spectra make it possible to distinguish between these two types of event. Figure 23 presents a zoom of Figure 20, showing the contributions associated with the detection of H^+CH_3OH. The fitting of the experimental histogram highlights the presence of three contributions in this peak, evaporation without fragmentation of the evaporated molecule (dark blue area) and with fragmentation of the evaporated molecule (cyan area). The evaporation with fragmentation of the neutral molecule is composed of 2 contributions (dotted cyan curves).

The dark blue contribution shown in Figure 23 is only present in the mass spectrum associated with a raw multiplicity of 2. The evaporation without fragmentation leads to events with a multiplicity of 2, thus it is consistent that this contribution is not present in the second COINTOF mass spectrum associated with a raw multiplicity of 3. The relaxation of $H^+(CH_3OH)_2$ observed with DIAM led to evaporation events without fragmentation of the neutral molecule, as described by the following equation:

$$H^+(CH_3OH)_2 \rightarrow H^+CH_3OH + CH_3OH \quad (7)$$

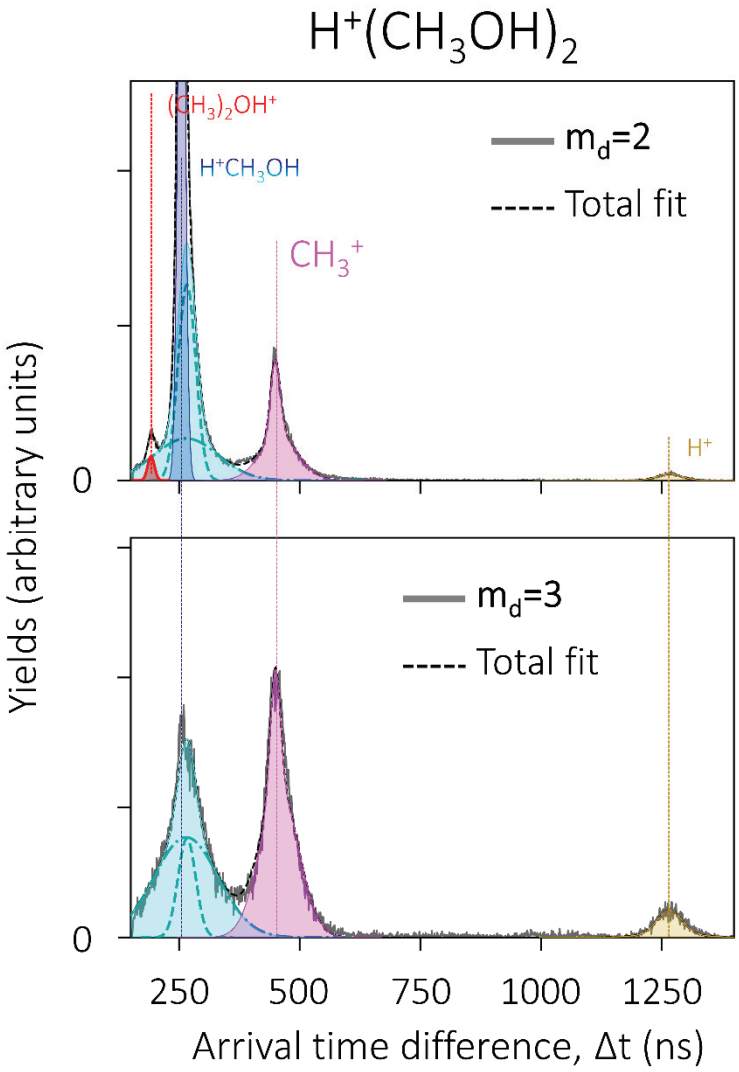

Figure 23: Zoom of Figure 20: COINTOF mass spectra of the protonated methanol dimer (accelerated to 8 keV) showing the two contributions in the H^+CH_3OH peak with fragmentation of the neutral methanol. Upper plot: histogram of the arrival time difference between the charged fragment and the neutral fragment Δt_{12} (grey curve). In this case, dissociation events selected to construct the histogram correspond to the detection of 2 fragments (m_d=2). The fit of the histogram is also drawn (black dotted line), and it consists of 7 contributions (filled coloured curves), each of them described by a sum of Gaussian functions. The first peak groups the evaporation events without fragmentation (dark blue area) and with fragmentation (cyan area) of the neutral pyridine molecule. Lower plot: histogram of the arrival time difference between the charged fragment and neutral ones, $<\Delta t>$. In this case, dissociation events which have been selected correspond to the detection of 3 fragments (m_d=3). The fit of the histogram is also drawn (black dotted line), and it consists of 6 contributions (filled coloured curves), each of them described by a sum of Gaussian functions. The coloured dotted lines correspond to the simulated positions of the identified charged fragments. In both graphs, the two Gaussian functions that represent the contribution associated with the detection of H^+CH_3OH, correlated with the fragmentation of the evaporated molecule are drawn (dashed and dotted cyan curves).

It should be noted that the COINTOF-VMI method has made it possible to measure the velocity distribution of the evaporated neutral methanol molecule, present in the relaxation

channel of Equation (7). This velocity distribution is presented in the lower plot of Figure 21 (orange solid line). The maximum of the velocity distribution of the methanol molecule is associated with a velocity value of 1.0×10^3 m.s^{-1}.

In addition to this contribution associated with the detection of a neutral fragment, a contribution associated with the detection of at least 2 neutral fragments, correlated with the detection of H^+CH_3OH, was observed. The presence of the H^+CH_3OH peak, even for (m_d=3), underlines the fact that evaporated methanol can be dissociated, after the energy deposition.

The COINTOF mass spectra show that the fragmentation of the evaporated molecule is composed of 2 contributions (dashed and dotted cyan curves). The comparison between the evolution of these 2 contributions between (m_d=2) and (m_d=3), gives information about the observed neutral fragments. Considering the existence of 2 contributions, one larger than the other, and the associated detection efficiency measurements, the H^+CH_3OH contribution (cyan curve in the COINTOF spectra), that is present for both the (m_d=2) case and the (m_d=3) case, is associated with the presence of two or more neutral fragments that are different, in term of mass. Indeed, by fitting the data, we can extract the detection efficiencies of the detected neutral fragments in correlation with H^+CH_3OH, for the fragmentation of the evaporated molecule. The large neutral fragments are associated to a detection efficiency value of 12%, while the small neutral fragments to 3%. This can be understood using the fragmentation channels. Considering the previous experimental results obtained with DIAM [3], the main fragmentation channels of neutral methanol lead to the formation of three groups of neutral fragments, classified by their masses: (i) CH_3O and CH_2OH (31 amu). (ii) CH_3 and OH (15 and 17 amu). (iii) H (1 amu). The associated processes are described by Equations (8-10).

$$CH_3OH \rightarrow CH_3O + H \tag{8}$$

$$CH_3OH \rightarrow CH_2OH + H \tag{9}$$

$$CH_3OH \rightarrow CH_3 + OH \tag{10}$$

2.3.2. The fragmentation of H^+CH_3OH

As already observed with the protonated pyridine dimer $H^+(Pyr)_2$ in the first section of this chapter, the study of the protonated methanol dimer $H^+(CH_3OH)_2$ revealed the existence of a relaxation channel characterised by the fragmentation of the protonated methanol ion and associated with the detection of a lower mass charged fragment, the CH_3^+ ion. Figure 24 shows a zoom of Figure 20, focusing on the contribution associated with the detection of CH_3^+. The fit

of the experimental histogram shows the presence of 2 contributions in this peak (green dashed and dotted curves).

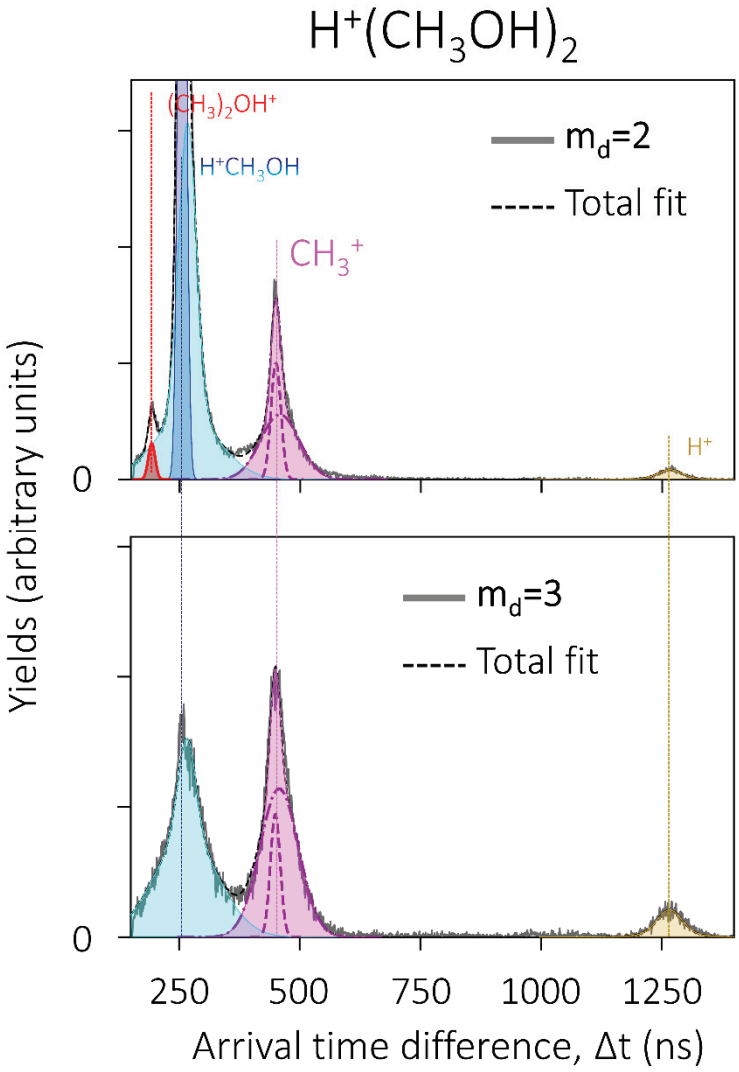

Figure 24: Zoom of Figure 20. COINTOF mass spectra of the protonated methanol dimer (accelerated to 8 keV) showing the two contributions in the H^+CH_3OH peak with fragmentation of the protonated methanol. Upper plot: histogram of the arrival time difference between the charged fragment and the neutral fragment Δt_{12} (grey curve). In this case, dissociation events selected to construct the histogram correspond to the detection of 2 fragments (m_d=2). The fit of the histogram is also drawn (black dotted line), and it consists of 7 contributions (filled coloured curves), each of them described by a sum of Gaussian functions. The first peak groups the evaporation events without fragmentation (dark blue area) and with fragmentation (cyan area) of the neutral pyridine molecule. Lower plot: histogram of the arrival time difference between the charged fragment and neutral ones, $<\Delta t>$. In this case, dissociation events which have been selected correspond to the detection of 3 fragments (m_d=3). The fit of the histogram is also drawn (black dotted line), and it consists of 6 contributions (filled coloured curves), each of them described by a sum of Gaussian functions. The coloured dotted lines correspond to the simulated positions of the identified charged fragments. In both graphs, the two Gaussian functions constituting the contribution associated with the detection of CH_3^+ and neutral fragments are drawn (magenta dotted and dashed curves).

The shape of the peak in the COINTOF mass spectra indicates the characteristics of the neutral fragments. Indeed, the width of a given contribution, is related to the mass of the neutral fragment associated with this contribution. The existence of two different Gaussian functions, with two distinct widths, shows that the charged CH_3^+ fragment (magenta peak in the spectra) is produced in correlation with at least two different neutral fragments, in term of mass.

The difference in term of mass also influences the difference in term of detection efficiency. As explained in Chapter II, the proportionality factor between the contribution (m_d=3) and the contribution (m_d=2) is related to the detection efficiency of the neutral fragments. The two contributions of the peaks associated with CH_3^+, correspond to detection efficiencies of 17% for the narrower contribution, consistent with CH_3OH, and 9% for the wider contribution, consistent with a fragment smaller than CH_3OH.

According to the measurements, the CH_3^+ daughter ion is detected in correlation with at least two different neutral fragments resulting from the fragmentation of H^+CH_3OH into CH_3^+. The presence of the CH_3^+ daughter ion can be related to the following dissociation process:

$$H^+(CH_3OH)_2 \rightarrow CH_3^+ + H_2O + CH_3OH \tag{11}$$

The process described by Equation (11), can be compared to the channel corresponding to evaporation with fragmentation of evaporated neutral methanol and the formation of CH_3 and OH. This channel is described by the following equation:

$$H^+(CH_3OH)_2 \rightarrow H^+CH_3OH + CH_3 + OH \tag{12}$$

The two channels, described by Equations (11) and (12) are both related to the fragmentation of the C-O bond, in the first case in the protonated methanol, and in the second case in the evaporated neutral methanol. Considering the detection efficiencies of the neutral fragments, the COINTOF mass spectra show that the events leading to C-O bond fragmentation in protonated methanol are observed in the same proportion as those leading to C-O bond fragmentation in the neutral methanol molecule.

2.4. The branching ratios between relaxation channels

Three relaxation channels of the protonated methanol dimer $H^+(CH_3OH)_2$ have been identified in the case of the protonated methanol dimer: the water elimination reaction, the evaporation without fragmentation of the neutral methanol molecule, and the fragmentation of

the methanol molecules. The multiparametric analysis allows us to deduce the branching ratios of these different relaxation channels (Table 2). The evaporation process without fragmentation of the neutral CH_3OH molecule represents 10% of the events, the fragmentation of the molecular ion or the neutral molecule represents 89%. Among these fragmentation events, the channel associated with the detection of CH_3^+, linked to the fragmentation of protonated methanol, represents about 17% of the events and the fragmentation of the neutral molecule without fragmentation of the molecular ion represents 83% of these events. Note that the relaxation channel leading to the detection of H^+ represents about 0.3% of the events. The elimination reaction of a water molecule leading to the formation of protonated dimethyl ether represents 0.6% of the events. The latter ratio may be relevant in understanding the abundances of dimethyl ether in the interstellar medium compared to that of methanol [6].

$H^+(CH_3OH)_2$

Relaxation channel	Water loss reaction	Evaporation without fragmentation	Fragmentation
Branching Ratio	0,01 ± 0,002	0,10 ± 0,05	0,89 ± 0,07

Table 2: Branching ratios between the three relaxation channels of the protonated methanol dimer after a single collision with an argon atom: the water loss reaction, evaporation without fragmentation and fragmentation of the molecules.

2.5. Study of the competition between the relaxation channels based on a statistical model

2.5.1. Post-collisional relaxation of $H^+(CH_3OH)_2$

The study of the post-collisional relaxation of the protonated methanol dimer $H^+(CH_3OH)_2$ in DIAM highlights the competition between the evaporation of a methanol molecule and the unimolecular reaction to form the dimethyl ether. The measurement of the velocity distribution of the water molecule eliminated during the formation of dimethyl ether revealed the presence of two Maxwell-Boltzmann type components. The presence of these two components led to the search for a second transition state for this reaction by DFT calculations. The two transition states and their associated reaction path are noted here as TS2 and TS3 and were described in detail in the previous section. The experiment allowed the measurement of the

branching ratios between the three processes: the evaporation of a methanol molecule, the water removal reaction via the TS2 path and this same reaction via the TS3 path.

The experimental results are presented in Figure 25. The velocity distributions are presented here as the distribution of the total kinetic energy release (KER) in the reference frame of the centre of mass of the cluster by the dissociation process. The branching ratios are presented in logarithmic scale in the insert. Note that the processes presented here correspond to relaxation mechanisms without fragmentation of the molecules. The wide range of deposited energy, opened by the high velocity collision, also allows the observation of fragmentation of molecules and in particular fragmentation after evaporation or fragmentation of dimethyl ether.

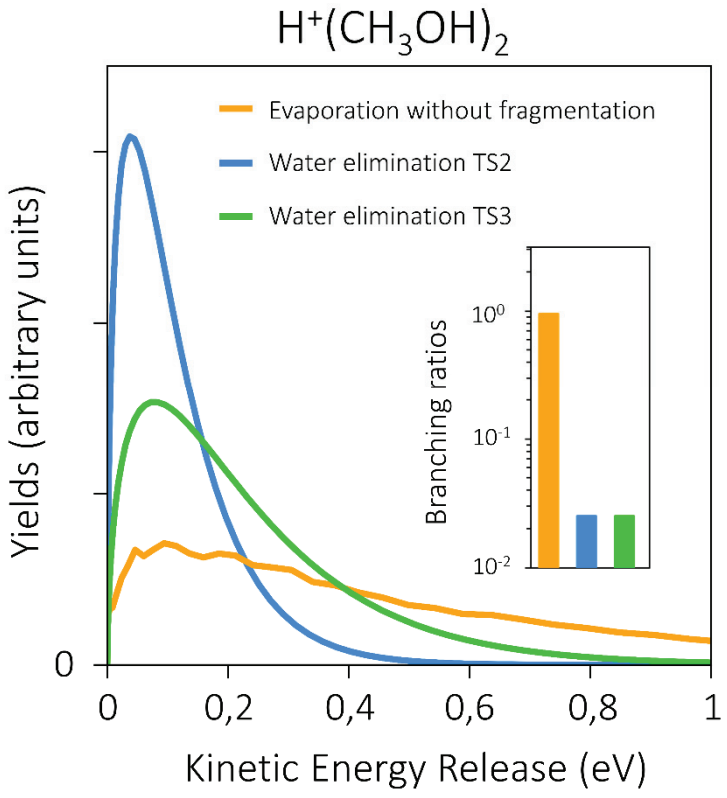

Figure 25: Distributions of kinetic energy released measured experimentally and normalised to the sum of the events of each dissociation channel. The blue and green curves correspond to two reaction paths leading to the formation of dimethyl ether via the elimination of a water molecule. The orange curve corresponds to the evaporation of a methanol molecule without fragmentation.

In Figure 25, it can be seen that the KER rarely exceeds 1 eV. When water is eliminated, the KER distribution shows a maximum at 0.1 eV. It can be seen that the kinetic energy released during the evaporation of methanol is greater than for the water elimination. The branching ratios show that 5% of the events are equally distributed between the two paths leading to the

formation of dimethyl ether via the elimination of a water molecule, and 95% of the events are evaporation processes without fragmentation. Indeed, after evaporation, either the molecule or the protonated methanol ion can fragment, both possibilities being observed in equal proportions.

The different relaxation processes of the protonated methanol dimer are schematically presented in Figure 26. The energetic aspects have been studied with DFT at the M06-2X/6-311++G(2df,p) level of theory.

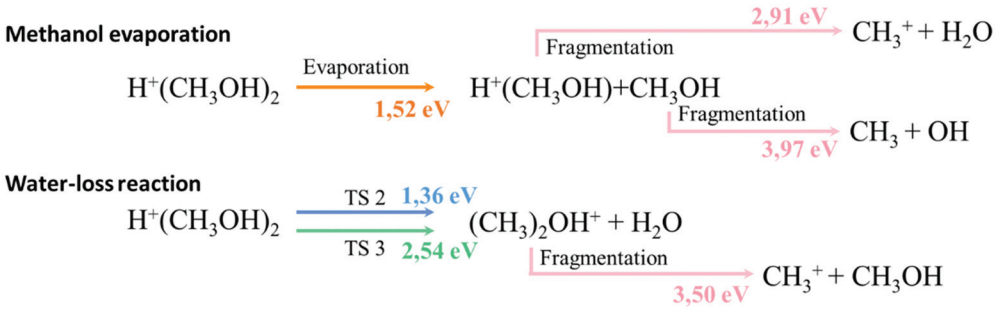

Figure 26: Relaxation channels and energetics associated to the unimolecular reactions observed within DIAM with the protonated methanol dimer. The energy values are determined by DFT calculations (M06-2X/6-311G++(2df,p)). The reactions presented in this schematic view are the ones used in the statistical models.

The energy threshold for forming dimethyl ether via TS2 is calculated to be 1.36 eV, which is slightly lower than the threshold for evaporating a methanol molecule (1.52 eV). The threshold for forming dimethyl ether via TS3 is significantly higher (2.54 eV). Fragmentation of molecules and molecular ions is observed. The fragmentation of the protonated methanol molecular ion (2.91 eV) has a lower energy threshold than the fragmentation of the neutral methanol molecule (3.97 eV). The threshold for the fragmentation of dimethyl ether is 3.50 eV. The fragmentation of water is not taken into account as it is not observed. The threshold is indeed much higher (5.01 eV).

2.5.2. Modelling the competition between evaporation and reactivity

The idea is to build a Monte-Carlo type simulation allowing to quantify the competition between the different relaxation channels, based on the results of the phase space theory (PST). On the one hand, the simulation is based on the time constants and KER distributions, calculated with PST for each dissociation channel and for a given internal energy value of the cluster. On the other hand, the simulation takes into account the experimental conditions: the duration for the relaxation of the cluster (168 ns in the protonated methanol dimer experiment) and the wide range of energy deposition involved.

Thus, the code allows:

- the use of the Beyer-Swinehart algorithm to calculate the density of states and the use of the PST model to calculate the time constants for a fixed internal energy as described in Chapter II,
- the choice for each cluster of an internal energy value in a given distribution. The results presented were obtained with a flat distribution from 0 to 10 eV,
- the introduction of a decision element as to the dissociation channel actually used by a cluster of given internal energy: for each dissociation channel, a time is randomly chosen from a decreasing exponential distribution whose time constant is that calculated for the internal energy value of the cluster. The shortest time designates the dissociation channel that will be recorded for that cluster. If the times are all greater than the relaxation window of the experiment (168 ns, in the case of the protonated methanol dimer), no dissociation is recorded for this cluster.

With the dissociation channel identified, a KER is randomly chosen from the KER distribution calculated for the internal energy value of the cluster with PST. Knowing the value of the KER, the internal energy for the dissociation fragments is randomly chosen from a distribution calculated from the densities of states. The procedure described above is then applied again, but this time on each reaction product, giving them the opportunity to fragment in turn, for the remaining duration of the relaxation window. Calculations are performed for a large number of clusters (typically 1000 clusters/meV) for each internal energy value in the 0-10 eV range, with a resolution of one meV. All data and results are saved in a file, keeping the information correlated, cluster by cluster. The analysis of this multiparametric file allows for quantitative comparison with experimental results.

2.5.3. Results obtained with the Phase Space Theory (PST)

The calculated results from the simulation applied to the evaporation and water removal reaction for the protonated methanol dimer are presented in Figure 27. In part (a) of Figure 27, the calculated time constants are plotted in logarithmic scale as a function of the internal energy of the cluster. All three constants decrease rapidly from the threshold energy and tend towards an asymptote of the order of 1 ns. The constants calculated for the two reaction paths TS2 and TS3, shown in blue and green respectively, merge because the calculation is based on the densities of states of the products. It can also be seen that the time constant related to the evaporation channel (orange curve) is significantly higher than those associated with the TS2 and TS3 reaction paths. A higher time constant produces a less likely channel in the simulation. This is observed in part (b) of Figure 27 where the probabilities of each channel are plotted against the internal energy of the cluster. The first grey values correspond to clusters for which all times are greater than the window duration (so-called "Nothing" events). For these events, either dissociation takes place outside the relaxation window or the internal energy is not sufficient to pass a threshold. From 1.36 eV, almost all clusters relax through the TS2 channel. However,

from the evaporation threshold onwards, evaporation is only weakly involved. Finally, from the threshold energy of the TS3 reaction path, we notice an equiprobability of events between the blue and green paths, the time constants being identical. The difference between the TS2 and TS3 reaction paths is due to a higher threshold energy (2.54 eV) for the TS3 path. The pink curve that appears around 5 eV corresponds to the fragmentation events of the protonated dimethyl ether after its formation and the fragmentation events of the neutral or protonated methanol after evaporation. These results show that, within the PST framework and the assumption of energy redistribution over all modes of the system, there is an internal energy range between 0 and 5 eV where the three channels considered here compete, without the intervention of molecular fragmentation.

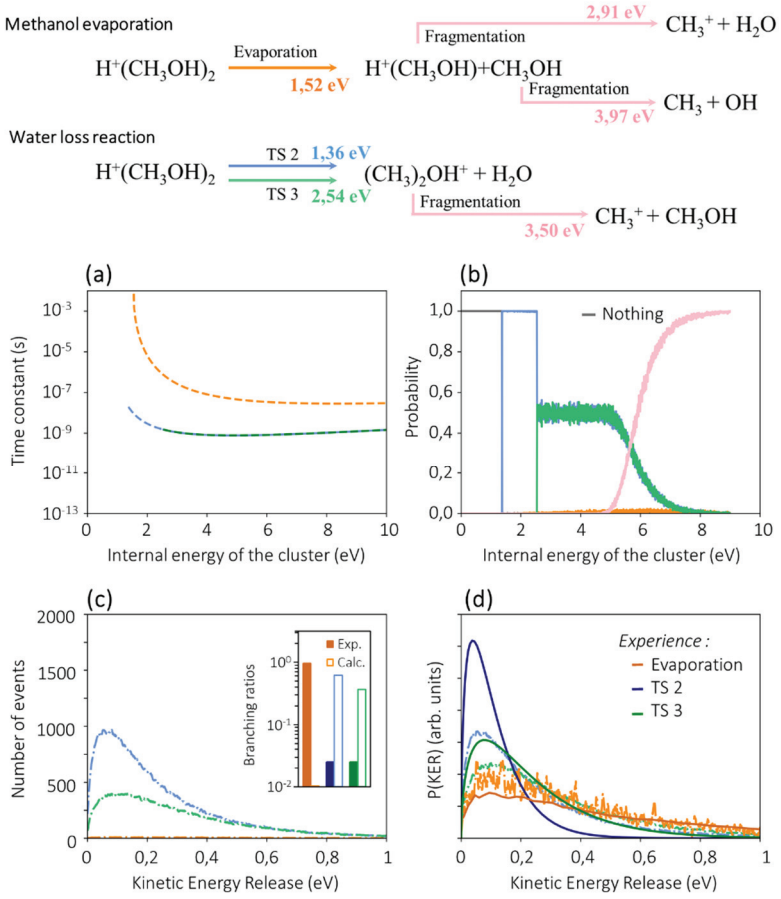

Figure 27: Phase space theory (PST) applied to the post-collisional relaxation of the protonated methanol dimer. (a): Time constant calculated as a function of the internal energy of the cluster for the dimethyl ether formation reaction for the two transition states (blue and green curves) and for the evaporation of a methanol molecule (orange). (b): Probability of observing the different relaxation channels: no dissociation (grey), the two transition states resulting in the formation of dimethyl ether and the elimination of a water molecule (TS2 and TS3), the evaporation of a methanol molecule and the fragmentation of a molecule of the cluster after evaporation (pink). For a uniform internal energy distribution between 0 and 10 eV. (c): Kinetic energy distribution released during relaxation calculated for a uniform internal energy distribution between 0 and 10 eV and comparison between experimental and model branching ratios in insert. (d):

Calculated distribution normalised to the same number of events (dashed line) and compared to the experimentally measured distribution (solid line).

Part (c) represents the distribution of the released kinetic energies, calculated for each dissociation channel. In the inset, the branching ratios calculated with this model and compared to those of the DIAM experiment are plotted. There is a significant disagreement between the experimental branching ratios and those calculated in the model. The comparison between the calculated KER distributions normalized to the same number of events with the experimental curves is presented in part (d).

Unlike the branching ratios, the KER distributions produce absolute mean values and shifts between the distributions close to the experimental values. It should also be noted that the theoretical description is constrained by the measurement of branching ratios and kinetic energy distributions released in each channel during the relaxation of the cluster in a fixed time window, after excitation by a single high-speed collision. Furthermore, the model as constructed produces information not directly accessible by experiment but showing other aspects of energy redistribution. For each relaxation channel, Figure 28 shows the correlation between the internal energy of the cluster and the released kinetic energy (a), between the internal energy of the cluster and the internal energy of the charged fragment (b) and between the internal energy of the cluster and the internal energy of the neutral fragment (c).

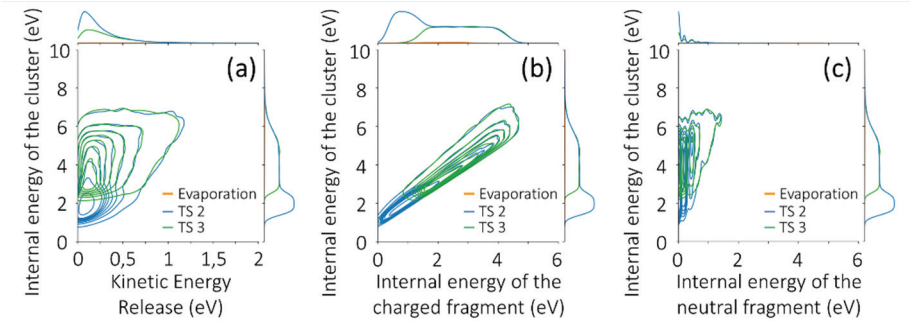

Figure 28: Correlation graphs between the internal energy of the cluster and (a) the kinetic energy released (KER), (b) the internal energy of the charged fragment, (c) the internal energy of the neutral fragment.

As expected, we observe that the KER distribution widens as the internal energy of the cluster increases. Similarly, the internal energies of the charged and neutral fragments are correlated with the internal energy in the cluster. Note that the internal energy of the neutral fragment is quantized because of the eigenmodes of the water molecule. These last two graphs show the potential of such a model, as the internal energy of the fragments released in the gas phase can be emitted, on larger time scales, as radiation. The good agreement obtained for the KER distributions led us to fit the model to the experimental results of the branching ratios by modifying only the reaction constants.

2.5.4. Results obtained with adjusted constants

We fitted the model to the experimental results by only changing the values of the time constants. We introduced a factor not depending on the internal energy on the time constants calculated for the different paths. In Figure 29 the results of the model with the adjustment are presented. The time constants have been fitted for evaporation and TS3 and are shown as solid lines in part (a) of this figure.

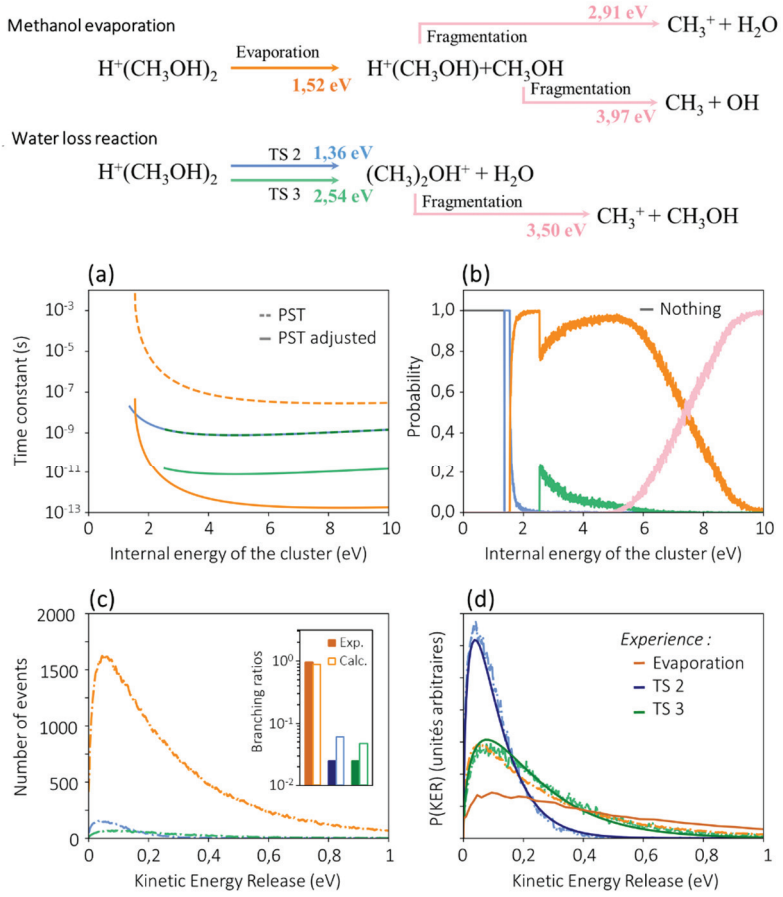

Figure 29: Phase space theory (PST) applied to the post-collisional relaxation of the protonated methanol dimer. (a) Time constant calculated as a function of the internal energy of the cluster (dotted line) and corrected time constant (solid line), (b) Probability of observing the different relaxation channels, (c) Distribution of kinetic energy released during relaxation calculated for a uniform internal energy distribution, (d) Calculated distribution normalised to the same number of events and compared to the experimentally measured distribution.

The evaporation time constant is now between 1 ns at low energy and 0.1 ps at high energy and is lower than those of the TS2 and TS3 reaction paths. As a result, the probability curve for the evaporation channel, shown in part (b) of Figure 14, is significantly steeper than in Figure 0.3, in agreement with the observed branching ratios. The KER histograms as well as the branching ratios presented in Figure 29 show good quantitative agreement with the experimental

results given the simplicity of the model. The KER distributions normalised to the same number of events, presented in part (d) of Figure 29, show a good fit for the TS2 (blue) and TS3 (green) paths. It should be noted that the decrease in the KER distribution at high KER values is related, for the blue path, to the presence of the green path and, for the green path, to the presence of evaporation. For evaporation, the experiment-model agreement is not optimal. The shape of the distribution of released kinetic energy is less broad than that measured. However, the decay of the KER distribution for large KER values for evaporation is associated with the possibility of fragmenting the molecules after evaporation. Experimental measurements show that, after evaporation, the fragmentation rates of the neutral and charged fragments are of the same order of magnitude. When calculating the probabilities, these two possible fragmentations were taken into account and the PST model favours the fragmentation of protonated methanol. To characterise the effect of these fragmentations after evaporation, we performed the calculations by imposing either the fragmentation of the protonated methanol $H^+(CH_3OH)$ or that of the neutral methanol (CH_3OH). The results are shown in Figure 30(A) and Figure 30(B), respectively. It can be seen in panel (b) of Figure 30(A) that the fragmentation event curve differs little from the model with all possible fragmentations. This shows that the fragmentation of protonated methanol after evaporation is more frequent in the model based on the complete redistribution of internal energy over all modes. In Figure 30(B), fragmentation occurs at higher energies than in Figure 30(A). This is explained by the difference in energy threshold between the fragmentation of the neutral and the fragmentation of the charged. As expected, it can be seen that the shape of the kinetic energy distribution released during evaporation without fragmentation is affected by the characteristics of the process competing for the highest internal energies.

The experiment shows that, after evaporation, the fragmentation of a neutral molecule is as important as the fragmentation of protonated methanol. However, the statistical model, which is based on the complete redistribution of energy, largely favours the fragmentation of charged methanol. Experimental observations show, therefore, that evaporation occurs before the complete redistribution of energy in the cluster and that the proton remains preferentially on the molecule that was not directly impacted during the collision.

Using the experimentally observed proportions, a velocity distribution for evaporation without fragmentation can be constructed from the results calculated above. This is 50% of the distribution obtained when considering only the fragmentation of charged methanol and 50% of the distribution obtained when considering only the fragmentation of neutral methanol. This distribution is presented as a velocity distribution in Figure 31 for direct comparison with the experimental data. A difference between the calculated and the measured velocity distribution remains. This difference can be fitted by a Gaussian and may correspond to the high velocity evaporation that is also observed for protonated methanol clusters.

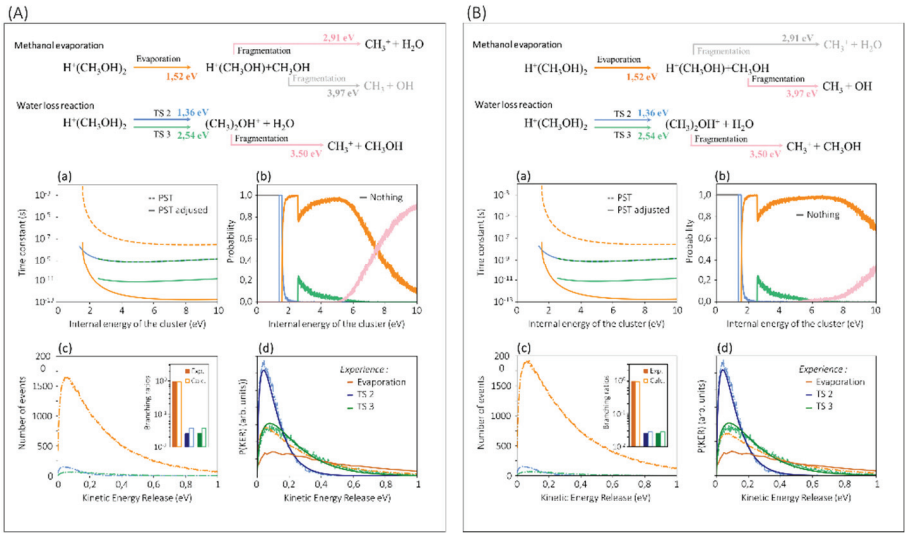

Figure 30: Phase space theory (PST) applied to the post-collisional relaxation of protonated methanol dimer. For evaporation, calculations are limited to either the fragmentation of protonated methanol H^+CH_3OH (A) or neutral methanol CH_3OH (B) For both figures: (a) Time constant calculated as a function of the internal energy of the cluster (dashed line) and corrected time constant (solid line), (b) Probability of observing the different relaxation channels; here, only the fragmentation of protonated methanol is considered for the pink curve, (c) Distribution of kinetic energy released during relaxation, calculated for a uniform internal energy distribution, (d) Calculated distribution normalised to the same number of events and compared to the experimentally measured distribution.

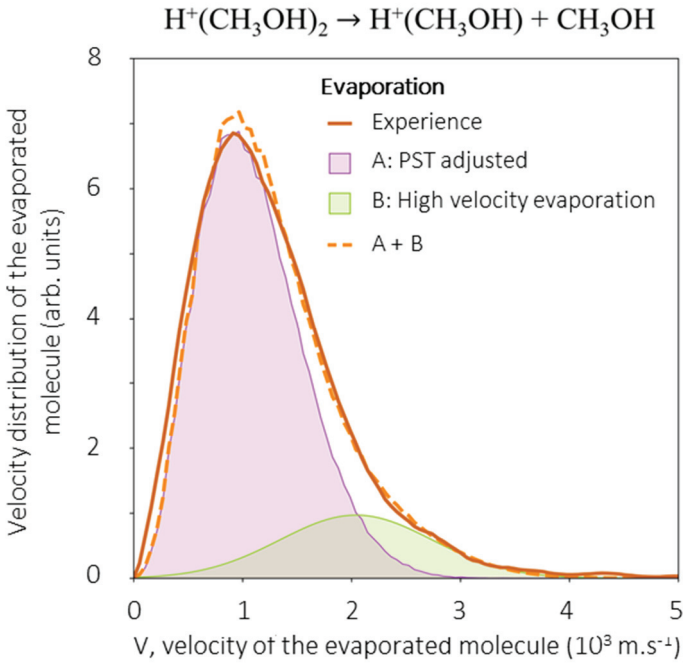

Figure 31: Velocity distribution of the evaporated molecule for the protonated methanol dimer. The experimental curve (solid line) is compared to the sum of the corrected evaporation calculated by the PST model (curve A) and the evaporation fitted by a Gaussian at high velocities (curve B).

Figure 32 shows the experimental velocity distributions for the evaporation of a methanol molecule from $H^+(CH_3OH)_{n=2-8}$ protonated methanol clusters and from $H^+(H_2O)_{n=2-8}$ protonated water clusters. The high velocity part of the distributions, associated with high velocity evaporation events, is highlighted by a vertical dashed line. This high velocity part is fitted by a Gaussian whose centre does not vary with the size of the cluster. As the number of molecules in the cluster increases, the width of the low speed peak decreases and the contribution of high velocity evaporation is clearly separated.

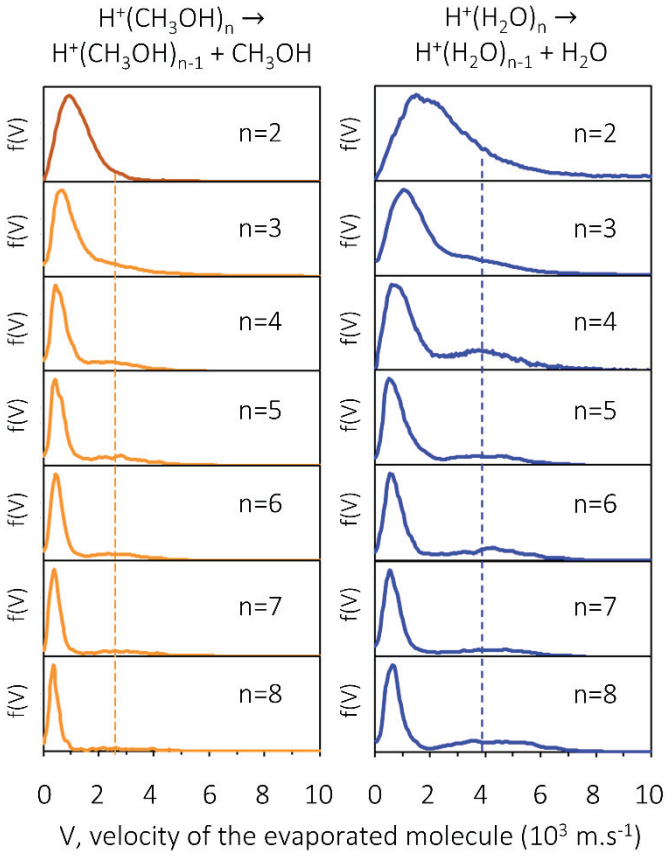

Figure 32: Velocity distributions of a single molecule evaporated from protonated methanol clusters (left) and protonated water clusters (right). The methanol dimer studied in this work is shown at the top left. Non-ergodic events are represented by the vertical dashed line.

All these results show that the PST models, associated with the complete redistribution of energy before dissociation, are not suitable but the systematic shifts observed are reference points. Specific consideration of the energy transfer time between the molecules of the cluster could be considered. The results obtained by this simple model, fitted to the experimental results, could be used in multi-scale models describing diluted media under irradiation.

3. Glycine peptide formation in a unimolecular reaction

3.1. Production of protonated molecular clusters of glycine

Glycine is the smallest of the amino acids. Amino acids are the building blocks of life and the study of the formation of peptide bonds between amino acids under abiotic conditions is a key step in the study of the conditions of the appearance of life.

Figure 33 shows the mass spectra obtained by adiabatic expansion of a glycine vapour (a) and a glycine and water vapour (b) in the DIAM device. In both spectra, with and without water, the main peak observed corresponds to the mixed dimer, composed of the protonated glycine dipeptide and a glycine molecule $H^+Gly_2(Gly)$ (208 amu). In the mass spectrum obtained from dry glycine (a), the protonated glycine dipeptide H^+Gly_2 (133 amu) is observed with a relative abundance compared to the main $H^+Gly_2(Gly)$ peak of 13%, and the mixed protonated cluster $H^+Gly_2(Gly)_2$ (283 amu) is observed with a relative abundance of 31%. Similar abundances are observed for these three protonated species when water vapour is added to glycine vapour in the cluster source (b).

In addition to the glycine-related peaks, another serie of peaks is identified in the spectrum, corresponding to the protonated water clusters (red arrows). In this spectrum, protonated water clusters containing seven water molecules $H^+(H_2O)_7$ (127 amu) up to fifteen water molecules $H^+(H_2O)_{15}$ (271 amu) are identified.

Figure 34 shows an additional mass spectrum obtained with glycine vapour with a lower precision than the previous figure but with a higher intensity. As observed in Figure 33, the main peak is associated with the mixed protonated dimer containing a glycine dipeptide and a glycine molecule $H^+Gly_2(Gly)$ (208 amu). The protonated dipeptide of glycine H^+Gly_2 (133 amu) is also present. In addition, mixed clusters containing a glycine dipeptide and n glycine molecules $H^+Gly_2(Gly)_n$ are observed, up to 4 glycine molecules. This higher intensity spectrum also reveals the presence of the pure protonated glycine dimer $H^+(Gly)_2$ (151 amu) but with a lower intensity compared to the mixed clusters. In these additional experiments, 2,5-diketopiperazine (DKP) is also observed, both in its ionised form (114 amu) and in its protonated form (115 amu). Traces of glycine polypeptides are also present, the protonated glycine tripeptide H^+Gly_3 (190 amu) and the protonated glycine tetrapeptide H^+Gly_4 (247 amu), with an intensity similar to that of the pure protonated glycine dimer. Protonated polypeptide formation has been previously observed for other amino acids, β alanine [7], tryptophan [8] and serine [9].

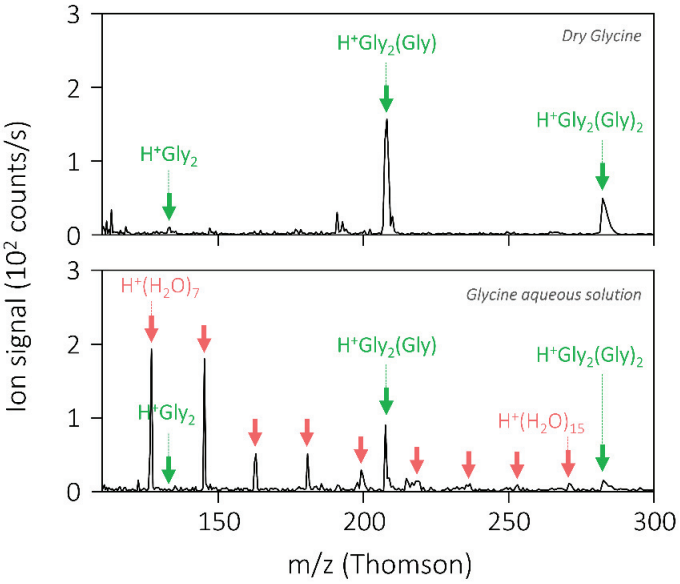

Figure 33: Protonated ions of mixed clusters after electron impact ionisation of a beam of neutral glycine clusters [glycine/water]. Mass spectrum containing the protonated ions produced by electron impact of a beam of neutral clusters after adiabatic expansion of a carrier gas containing either glycine/water vapour (upper panel) or dry glycine vapour (lower panel). The protonated glycine peptide ion H^+Gly_2 and the protonated mixed cluster ions $H^+Gly_2(Gly)_{n=1,2}$ are highlighted by green arrows. The protonated water cluster ions $H^+(H_2O)_{n=7\text{-}15}$ are highlighted with red arrows.

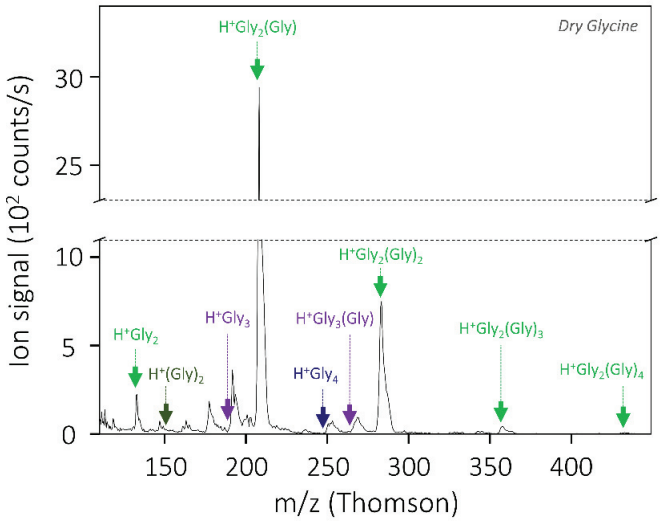

Figure 34: Proton species formed during electron impact ionisation of a dry glycine vapour. The mass spectrum (black curve) is measured under similar conditions to the spectra in Figure 14 but with a different detector, with a lower resolution than the latter. Mixed clusters containing a glycine dipeptide and n glycine $H^+Gly_2(Gly)_n$ molecules are identified by light green arrows, from n=0 to n=4. The pure protonated glycine dimer $H^+(Gly)_2$ is identified by a dark green arrow. Mixed clusters containing a glycine tripeptide and m glycine molecules $H^+Gly_3(Gly)_m$ are identified by purple arrows, from m=0 to m=1. The glycine tetrapeptide H^+Gly_4 is identified by a blue arrow.

The presence or absence of water clusters does not seem to influence the proportion between glycine-related peaks. Another interesting aspect is that mixed clusters between glycine and water were not observed. Previous work on DIAM shows the formation of mixed clusters between pyridine and water [2] [10] or with methanol and water [3].

The mass spectra obtained with the DIAM cluster source show that the device allows to produce a wide variety of species. The spectrum presented above shows that protons prefer to bind to species containing dipeptide rather than pure glycine clusters. Proton behaviour plays a crucial role in the dominant formation of these mixed proton clusters. Indeed, the study of proton affinities gives indications to help the interpretation this result. Figure 35 shows the quantum chemical calculations of the proton affinity (PA) of various species that have been studied with DIAM.

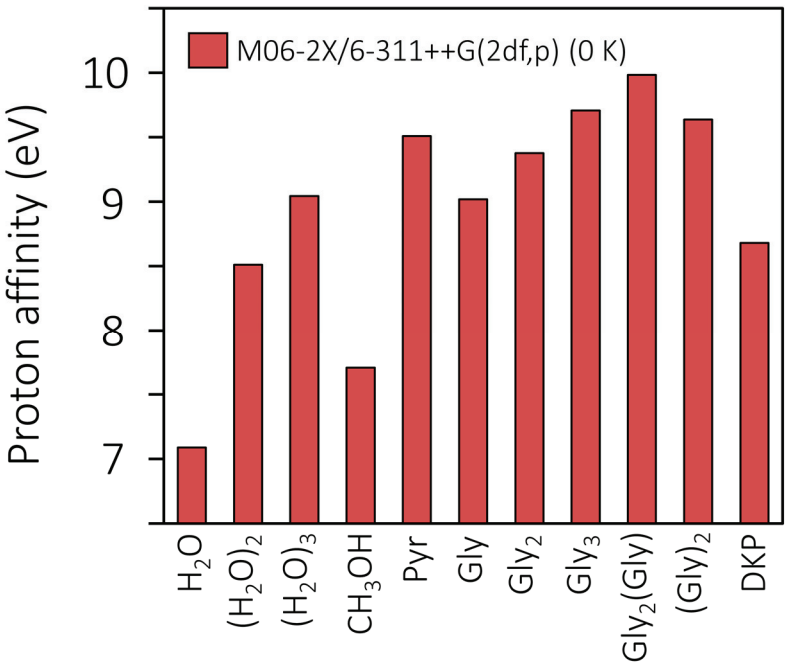

Figure 35: Proton affinity (PA) of several species of molecules studied with DIAM. The PA values were obtained using the level of theory specified in the legend.

The glycine tripeptide Gly_3, is associated with a PA value of 9.7 eV, which is higher than the dipeptide Gly_2, 9.4 eV. Both species have a higher PA value than the glycine monomer Gly, 9.0 eV. The PA of the pure protonated glycine dimer $(Gly)_2$ is 9.6 eV, and lies between Gly_2 and Gly_3. Furthermore, Figure 35 shows that the mixed dimer $Gly_2(Gly)$ has the highest PA, 10.0 eV. This is in good agreement with the results of the experimental mass spectra presented above in which the protonated mixed dimer $Gly_2(Gly)$ is dominant. It is interesting to note that the PA

of $Gly_2(Gly)$ is much higher than the PAs of other species studied with DIAM, in particular the pyridine Pyr for which the PA is 9.5 eV.

Mass spectra obtained with DIAM and proton affinity calculations show the importance of protons in the formation of molecular clusters, such as $H^+Gly_2(Gly)$ or $H^+(Gly)_2$. Compared to previous studies with DIAM, methanol or pyridine, the behaviour of glycine is different.

3.2. The pure glycine dimer $H^+(Gly)_2$

3.2.1. Evaporation, fragmentation, and reactivity

The observation of the water elimination reaction in the protonated methanol dimer paved the way for the study of post-collisional relaxation of the pure glycine cluster $H^+(Gly)_2$. Indeed, the reaction between two amino acids to form a peptide bond is also an elimination reaction of a water molecule. As for methanol, the COINTOF-VMI method allows the identification of the reaction channel by correlated detection of the reaction products, the neutral and the charged fragments, after selection in mass and energy of the parent cluster ion.

The pure protonated glycine dimer $H^+(Gly)_2$ contains two glycine Gly molecules, Gly, and a proton. The clusters are accelerated to 8 keV, and given the mass of the cluster, 151 amu, this corresponds to a velocity in the laboratory of 1.01×10^5 m.s^{-1}. The binding energy of the cluster molecules was calculated by the IPM team (M06-2X/6-311++G(2df,p)) and is around 1.33 eV, a value which is in good agreement with the calculations of Price et *al.* , 1.41 eV (MP2/3-21+G(d,p)//MP2/3-21G(d)) and also with their experimental results, 1.15 eV [11].

Figure 36 shows the COINTOF mass spectrum of the charged fragments induced by the relaxation of the pure protonated glycine dimer $H^+(Gly)_2$ after a collision with an argon atom. The experimental curve corresponds to the histogram of the arrival time difference between the charged and the neutral fragment for events with a raw multiplicity, m_d, of 2 (grey curve). In the case of the pure protonated glycine dimer $H^+(Gly)_2$, twelve main charged fragments are identified corresponding to the twelve peaks in the COINTOF mass spectra.

The peak shown in red in the mass spectrum in Figure 36, corresponding to the correlated detection of the protonated glycine dipeptide and a single neutral fragment, is the signature of the production of the dipeptide via a unimolecular reaction:

$$H^+(Gly)_2 \rightarrow H^+Gly_2 + H_2O \qquad (13)$$

Evaporation of the monomer without fragmentation of the evaporated neutral molecule, a glycine, corresponds to the blue peak in the COINTOF mass spectrum. The process associated with the evaporation of a glycine molecule without fragmentation corresponds to the following equation:

$$H^+(Gly)_2 \rightarrow H^+Gly + Gly \tag{14}$$

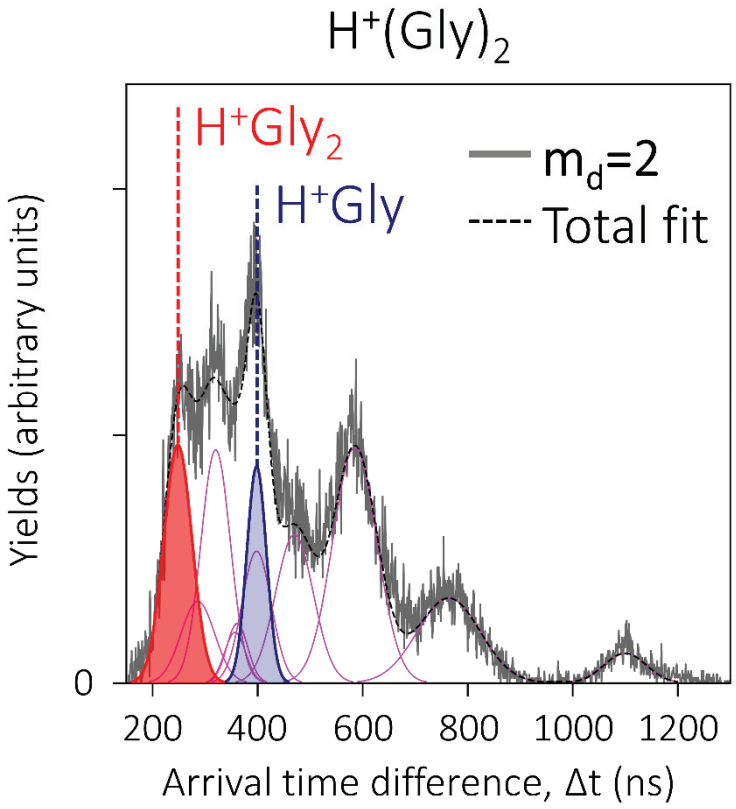

Figure 36: COINTOF mass spectrum of pure protonated glycine dimer $H^+(Gly)_2$ accelerated to 8 keV. Histogram of the arrival time difference between a neutral and charged fragment Δt_{12} (grey curve) associated with the detection of a single neutral fragment. The fit of this histogram is also drawn (black dotted line), and consists of eleven components associated with different charged fragments (coloured curves). The water loss reaction that leads to the formation of the dipeptide is highlighted (red filled curve). The blue filled curve corresponds to the monomer evaporation reaction which is associated with the correlated detection of H^+Gly and Gly. The contributions corresponding to the dissociation of the molecules are represented by purple curves. The peak associated with the detection of H^+ is also present at higher Δt values, but is not represented in this graph.

The group of magenta Gaussian functions, corresponding to the fragmentation of the protonated glycine dipeptide. The relaxation after a single collision with an argon atom of the protonated glycine dipeptide H^+Gly_2 was studied with DIAM. The protonated glycine dipeptide H^+Gly_2 is composed of a proton and a glycine dipeptide. The parent ion is accelerated to 8 keV,

and given the mass of the glycine dipeptide, 133 amu, this corresponds to a speed in the laboratory frame of 10.8×10^4 m.s^{-1}. Figure 37 shows the COINTOF mass spectrum of the charged fragments (grey curve) associated with the relaxation of the protonated glycine dipeptide. The mass spectrum presented in this figure is associated with a raw multiplicity of 2, one charged and one neutral fragment were detected. The black dashed curve corresponds to the COINTOF mass spectrum fit. Each contribution is characterised by a Gaussian function. The fitting of the spectrum reveals the presence of 10 contributions. 9 peaks are represented in the figure, the tenth observed contribution is related to H^+ detection represents only a minor proportion of the observed relaxation channels. The COINTOF mass spectrum shows that the relaxation of the protonated glycine dipeptide led to 8 different relaxation channels, related to bond fragmentation in the parent protonated glycine dipeptide: (i) formation of H^+DKP by water loss reaction, associated with a daughter ion mass of 115 amu. (iii) loss of CO and NH_3 or loss of H_2O and CO (87 amu). (iv) the formation of H^+Gly (76 amu). (v) loss of Gly (57 amu). (vi) formation of $COOH^+$ (45 amu). (vi) formation of $CH_2NH_2^+$ (30 amu). (vii) the formation of CH_3^+ (15 amu). (viii) the formation of H^+ (1 amu). The observations are in good agreement with those made by Armentrout *et al.* [12].

All charged fragments observed in the COINTOF mass spectrum of the protonated glycine dipeptide H^+Gly_2 are present in the spectrum of the pure protonated glycine dimer $H^+(Gly)_2$. The presence of these peaks indicates that the protonated glycine dipeptide can be formed and then dissociated during the relaxation window.

Thus, when considering the COINTOF spectrum obtained with the glycine dimer, the relatively large diversity of fragments can be observed in three groups: The unimolecular reaction leading to the formation of the dipeptide and a water molecule (red), evaporation without fragmentation (blue) and fragmentation of at least one molecule of the parent cluster (magenta). Table 3 shows the branching ratios of the relaxation channels observed after relaxation of the pure protonated glycine dimer. In conclusion, under the conditions of the experiment which led to a wide range of energy deposition, the evaporation without fragmentation, in other words the persistence of protonated glycine and neutral glycine, represents 7% of the events. The channels associated with the detection of characteristic fragments of the protonated dipeptide represent 82% of the events. The water loss reaction associated with the formation of a new peptide bond accounts for 11% of events.

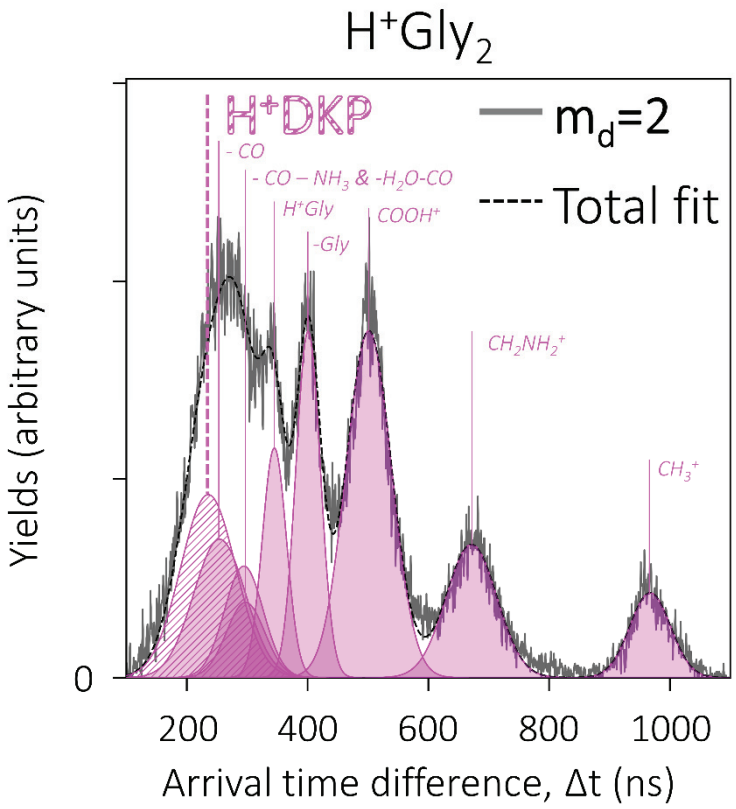

Figure 37: COINTOF mass spectrum of protonated diglycine H^+Gly_2 accelerated to 8 keV. Histogram of the arrival time difference between a neutral and charged fragment Δt_{12} (grey curve) associated with the detection of a charged and a neutral fragment. The fit of this histogram is also drawn (black dotted line), and consists of 9 components associated with different charged fragments (purple filled curves). The contribution associated with the detection of H^+DKP is hatched. The observations are in agreement with those made by Armentrout et *al.* [12]. The peak associated with the detection of H^+ is also present at higher Δt values, but is not shown in this plot.

$H^+(Gly)_2$

Relaxation channel	Water loss reaction	Evaporation without fragmentation	Fragmentation
Ratio	0,11 ± 0,03	0,07 ± 0,02	0,82 ± 0,04

Table 3: Branching ratios between the relaxation channels of the pure protonated dimer of glycine.

3.2.2. The velocity distribution of the eliminated water molecule

The formation of the protonated glycine dipeptide from the pure protonated glycine dimer is a crucial reaction. Indeed, the starting point, the protonated dimer, corresponds to a weakly bound system composed of two distinct glycine molecules without peptide bond. The COINTOF-VMI method, as explained in Chapter II, allows us to measure the velocity distribution of neutral fragments. In the case of the water loss reaction, it is possible to measure the velocity distribution of the eliminated water molecule. Figure 38 shows the measured velocity distribution of the eliminated water molecule (solid red curve) during the water loss reaction that leads to the formation of the protonated glycine dipeptide H^+Gly_2 in the glycine dimer $H^+(Gly)_2$.

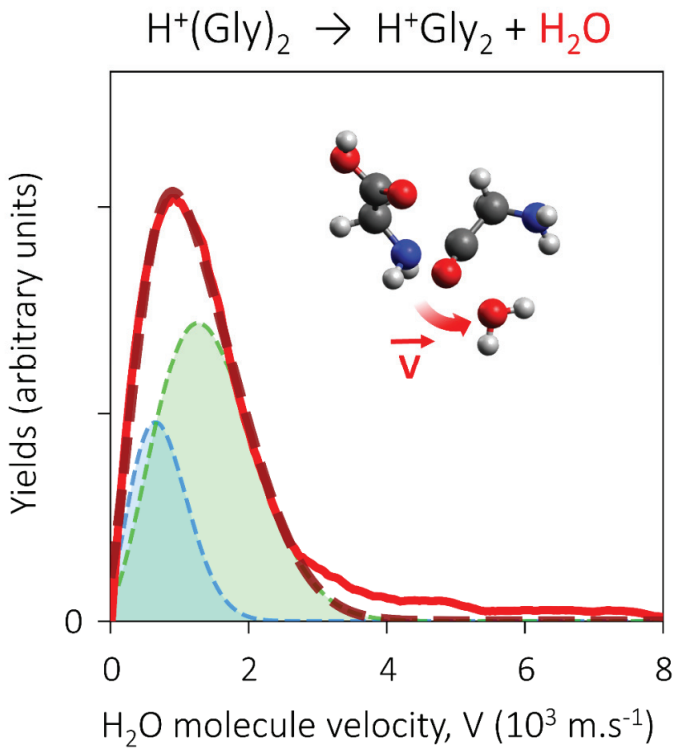

Figure 38: Experimental velocity distribution (red solid line) of the water molecule eliminated by the pure protonated glycine dimer (8 keV), after a collision with an argon atom. The fit of the experimental distribution is also drawn (red dotted line) and consists of two Maxwell-Boltzmann distributions (blue and green dotted lines).

The velocity distribution of the water molecule is mainly composed of a contribution that lies between 0 and 3×10^3 m.s^{-1}. The maximum of this contribution is located at about 1.1×10^3 m.s^{-1}. The experimental distribution of the water molecule is composed of two Maxwell Boltzmann distributions (blue area and green area). The lower Maxwell Boltzmann distribution (blue area) is associated with an average velocity of 7.7×10^2 m.s^{-1}. The higher Maxwell Boltzmann (green area) is associated with an average velocity of 1.5×10^3 m.s^{-1}. The presence of these two

Maxwell Boltzmann contributions underlines the existence of two different ways of carrying out the water loss reaction in the pure protonated dimer and motivates the study of the transition states for this water loss reaction in the pure glycine dimer $H^+(Gly)_2$.

3.2.3. Reaction pathways associated with the formation of the protonated dipeptide H^+Gly_2

A study of peptide bond formation from ion molecule reactions in the gas phase was carried out by Redondo *et al.* [13]. They considered the reaction between protonated glycine and neutral glycine, as well as the reaction between two neutral glycine molecules. Two different mechanisms, "concerted" and "stepwise", were studied. Both mechanisms show significantly higher energy barriers for the reaction between neutral molecules. The barriers are different for the glycine protonation sites and, depending on the mechanism, the protonation site of the glycine dipeptide produced is different.

We have studied the reaction pathways based on the structures of the two transition states proposed by Redondo *et al.* for the reaction between glycine and protonated glycine. The results are shown in Figure 39. The Intrinsic Reaction Coordinate (IRC) was performed at the HF/6 21G level. The transition state structures and minima are optimised at the M06-2X/6-311G++(2df,p) level of theory. For each structure, eigenfrequencies were calculated to ensure that it was a minimum on the potential energy surface or a transition state. The energy levels contain the Zero Point Energy (ZPE), corrected by the factor corresponding to the theory used (in this case, 0.9663 [14]). The whole of the conformer space has not been explored in detail in the reaction paths. The article of Paizs *et al.* [15] presents a study of proton mobility and conformational changes in the glycine dipeptide, and it shows that such processes require small amount of energy (typically less than one eV for proton transfer between the nitrogen atoms).

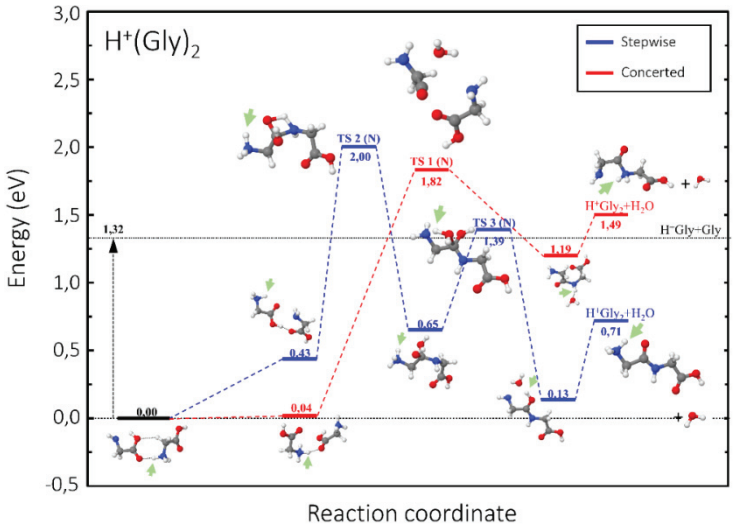

Figure 39: Energy diagram calculated via different quantum chemical methods and compared to the results of Redondo *et al.* [13] for the formation of the glycine dipeptide from a pure glycine cluster. The calculations initially obtained in HF/6-21G (black) are optimised in M06-2X/6-311G++(2df,p) (red). Redondo's calculations in CCSD(T)/6-311++G(d,p)//B3LYP/6-311+G(d,p) (blue) are compared with our calculations in CCSD(T)/6-311++G(2df,p)//M06-2X/6-311++G(2df,p) (green). The structure before the transition state (TS) is different in our calculations (red and black) and in the Redondo calculations (blue). GS denotes the ground state of the protonated glycine dimer. The energy reference corresponds to the separated molecules H+Gly+Gly (0.00 eV).

The presence of the proton on the peptide bond formation site lowers the energy barrier required to form the dipeptide. Furthermore, the two reaction paths produce different dipeptide conformers. The energy difference between the transition states and the products, for the blue pathway (1.29 eV), is much larger than that for the red pathway (0.33 eV). The energy available for redistribution is lower when the water molecule is eliminated via the red pathway than via the blue one. The presence of these two transition states is in qualitative agreement with the presence of two Maxwell Boltzmann distributions in the velocity distribution of the eliminated water molecule. The difference in reaction threshold between the two paths is smaller compared to the methanol case, but the reaction products are significantly lower in energy for the TS2(N) path, opening up the possibility of higher KER values for this path. The development of the statistical model describing the competition between several reaction paths could allow the establishment of a quantitative link between the DFT results and the measured KER distributions.

3.3. The mixed dimer $H^+Gly_2(Gly)_2$

3.3.1. The branching ratios between channels

The mixed protonated glycine dimer $H^+Gly_2(Gly)$ contains a proton, a glycine molecule and a glycine dipeptide. The clusters are accelerated to 8 keV, and given the mass of the cluster, 208 amu, this corresponds to a velocity in the laboratory of 8.62×10^4 m.s^{-1}. The binding energy of the molecules in the cluster is about 1.30 eV. This value was calculated during this work, to our knowledge for the first time in the case of the mixed dimer.

Figure 40 shows the COINTOF mass spectrum of the mixed protonated dimer $H^+Gly_2(Gly)$ obtained after a single collision with an argon atom at high speed (8 keV). The mass spectrum presented in this figure is associated with a raw multiplicity of 2, and is then associated with events in which one charged and one neutral fragment were detected. The dashed black curve corresponds to the COINTOF mass spectrum fit. The fitting of the spectrum reveals the presence of 14 contributions, only 13 are shown in the figure, the last one corresponds to the detection of H^+ and represents only a minor proportion of the observed relaxation channels. Each contribution is represented by a Gaussian function.

The fit shows the presence of three different types of relaxation channels. The first is associated with magenta contributions in which the initial peptide chain is broken. These correspond to the molecular fragmentation events that lead to the detection of charged fragments already identified in the COINTOF mass spectrum of the protonated glycine dipeptide H^+Gly_2. These contributions seem to be mainly due to the fragmentation of the protonated glycine dipeptide, but some of them could also be related to the fragmentation of protonated glycine or protonated triglycine.

In addition to fragmentation events, the other type of relaxation is associated with dissociation of the parent cluster ion for which the initial peptide chain is preserved. In the case of $H^+Gly_2(Gly)$, these events are associated with the detection of either H^+Gly_2 or H^+Gly, depending on which molecule of the cluster the proton is in during dissociation. Equations (15) and (16) show the reactions that can be associated with the detection of H^+Gly_2 and H^+Gly, respectively. The detection of H^+Gly_2 can be associated with events with a multiplicity of 2 (dark blue line), i.e. without fragmentation of the evaporated glycine, and also with events with a multiplicity greater than 2 (cyan line) in which the charged fragment can be detected in correlation with at least two other neutral fragments. In both cases, the original peptide chain is preserved. In the case of H^+Gly detection, the evaporated glycine dipeptide Gly_2 can also be fragmented or not, but only the second case is highlighted here (cyan line). Indeed, the initial peptide chain is only preserved if the evaporated dipeptide is intact.

$$H^+(Gly)_2(Gly) \rightarrow H^+Gly_2 + Gly \quad (15)$$

$$H^+(Gly)_2(Gly) \rightarrow H^+Gly + Gly_2 \quad (16)$$

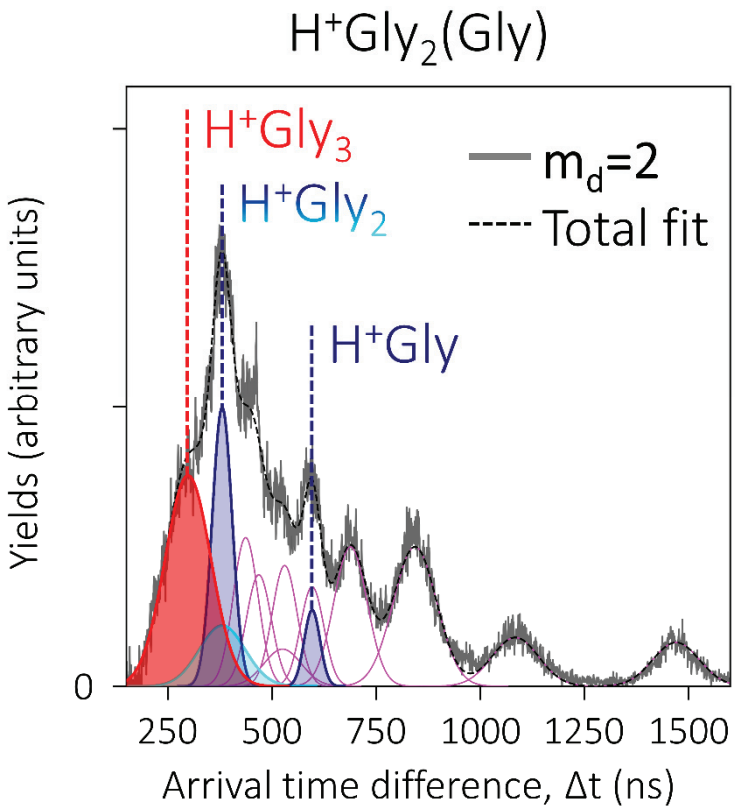

Figure 40: COINTOF mass spectrum of the mixed protonated $H^+Gly_2(Gly)$ dimer accelerated to 8 keV. Histogram of the arrival time difference between a neutral fragment and the charged fragment Δt_{12} (grey curve) associated with the detection of a single neutral fragment. The fit of this histogram is also drawn (black dotted line), and consists of thirteen components associated with different charged fragments (coloured curves). The water loss reaction that leads to the formation of the protonated glycine tripeptide is highlighted (red filled curve). The blue-filled curves correspond to relaxation pathways in which the initial peptide bond is not broken. The dark blue curves are associated with events with a multiplicity of 2, the light blue curve is associated with events with a multiplicity greater than 2 and corresponds to events in which the evaporated glycine is broken. The contributions corresponding to the dissociation of the molecules, with the exception of the fragmentation of the evaporated glycine (light blue curve) are represented by purple curves.

As in the case of the methanol dimer and the glycine dimer, in Figure 40 the red peak results from the correlated detection of the protonated glycine tripeptide and a single neutral fragment. This is the signature of peptide chain elongation via a unimolecular reaction:

$$H^+(Gly)_2(Gly) \rightarrow H^+Gly_3 + H_2O \quad (17)$$

Table 4 shows the branching ratios between the relaxation channels of the mixed $H^+Gly_2(Gly)$ dimer after a single collision with an argon atom. The persistence of the initial peptide chain represents 17% of the observed events. The fragmentation of the molecules represents 66% of the cases. And the water loss reaction which corresponds to a growth in molecular complexity represents 17% of the events. It is interesting to note that 30% of the reactions according to Equation (15) are associated with the dissociation of the evaporated glycine molecule.

$H^+Gly_2(Gly)$

Relaxation channel	Water loss reaction	Persistence of the initial peptide chain	Fragmentation
Ratio	0,17 ± 0,05	0,17 ± 0,06	0,66 ± 0,08

Table 4: Branching ratios between the relaxation channels of the protonated mixed dimer containing a dipeptide and a glycine.

3.3.2. The velocity distribution of the eliminated water molecule

The formation of the protonated glycine tripeptide H^+Gly_3, from the mixed protonated glycine dimer $H^+Gly_2(Gly)$, is a key point in the study of the growth of peptide chains. Indeed, the parent cluster ion contains a peptide bond with the dipeptide, and the relaxation can lead to the formation of a tripeptide with two peptide bonds. The water loss reaction is then associated with the growth of the peptide chain, which is crucial in prebiotic chemistry to understand how the building blocks of life can appear and develop.

The COINTOF-VMI method, as explained in Chapter II, allows us to measure the velocity distribution of neutral fragments. In the case of the water loss reaction, it is possible to measure the velocity distribution of the lost water molecule. Figure 41 shows the measured velocity distribution of the eliminated water molecule (red solid curve) during the water loss reaction.

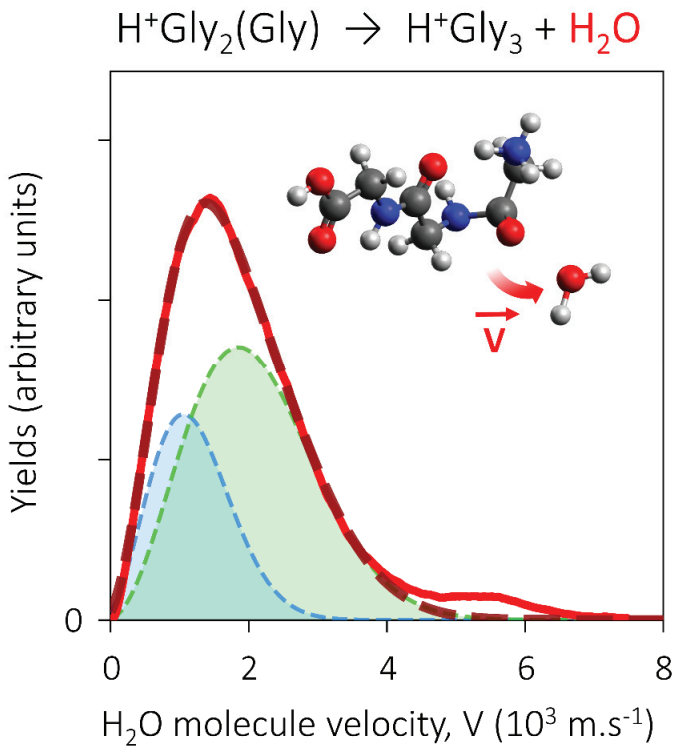

Figure 41: Measured velocity distribution (red solid line) of the water molecule eliminated by the mixed protonated glycine dimer (8 keV), after a collision with an argon atom. The fit of the experimental distribution is also drawn (red dotted line) and consists of two Maxwell-Boltzmann distributions (blue and green dotted lines).

The velocity distribution of the water molecule is mainly composed of a contribution that lies between 0 and 4×10^3 m.s^{-1}. The maximum of this contribution is located at about 1.8×10^3 m.s^{-1}. The experimental distribution of the water molecule is composed of two Maxwell Boltzmann distributions (blue area and green area). The lower Maxwell Boltzmann (blue area) is associated with an average velocity of 1.2×10^3 m.s^{-1}. The higher Maxwell Boltzmann (green area) is associated with an average velocity of 2.1×10^3 m.s^{-1}. The presence of these two Maxwell Boltzmann contributions in the experimental velocity distribution underlines the existence of at least two different ways of carrying out the water loss reaction in the protonated mixed dimer.

3.3.3. Reaction pathways associated with the formation of the protonated tripeptide H^+Gly_3

The search for the transition states for the tripeptide formation reaction in the mixed glycine-dipeptide protonated cluster was built from a reflection on the place of the proton and its role in the reaction. The calculations were oriented along two axes: the location of the proton in the starting conformer (on the glycine or on the dipeptide) and the location of the proton at or away from the reaction site. Figure 42 shows two calculated M06-2X reaction paths for the formation of the glycine tripeptide from the mixed glycine dimer.

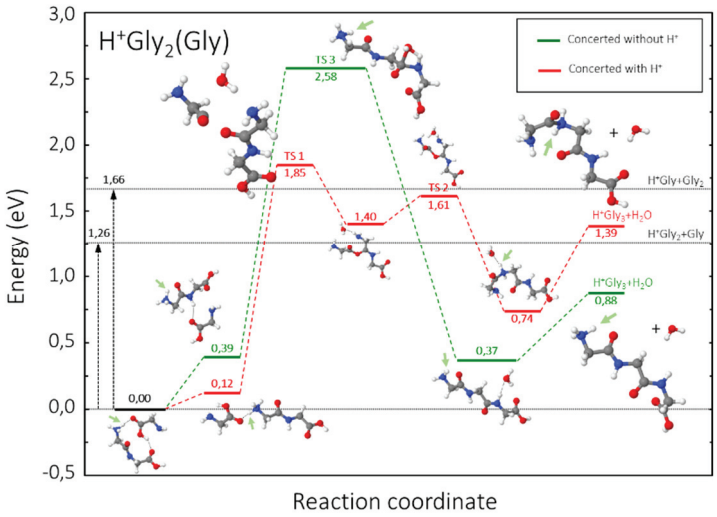

Figure 42: Energy diagram at 0 K calculated in DFT (M06-2X/6-311G++(2df,p)) for the formation of the glycine tripeptide from a mixed glycine cluster, in the case where the proton is on the glycine dipeptide $H^+Gly_2(Gly)$, with (red) and without (green) the presence of the proton at the peptide bond formation site. The calculated energies include the zero-point energy. The structures associated with the energies are shown in the figure and the green arrow indicates the position of the proton. The energy reference (0 eV) corresponds to the ground state energy of the $H^+Gly_2(Gly)$ cluster. The vertical black arrows indicate the evaporation process of a glycine molecule or a glycine dipeptide molecule from the cluster.

The pathway shown in red, whose threshold is given by the transition state TS1, shows the formation of the peptide bond from the reaction between the protonated amine group and the acid group. For the green pathway, associated with the transition state TS2, the reaction takes place between the neutral amine group and the acid group. According to the denomination of Redondo *et al.* [13] these two paths resemble "concerted" type mechanisms calculated for the reaction between two molecules. In our calculations, initially, for both paths, the proton is on the glycine dipeptide. However, the proton is far from the reaction site in the case of the green pathway, whereas the proton is at the reaction site for the red pathway and participates in a hydrogen bond. The TS1 transition state resembles that obtained by Redondo et al. for the reaction between a glycine molecule and a protonated glycine. The IRC calculations (HF/6-21G) show an intermediate potential where a water molecule would oscillate between the two nitrogen atoms, and a second transition state denoted TS2, lower in energy than the TS1 transition state. The glycine tripeptide formed by this reaction path is protonated on the nitrogen of the peptide bond. The second pathway associated with the TS3 transition state leads to the formation of the peptide bond without the involvement of the proton. The tripeptide thus formed is protonated on the terminal amine group. This second higher threshold energy pathway resembles that obtained by Redondo *et al.* [13] for the reaction between two neutral glycine molecules. Thus, by comparing the two paths, it can be seen that the presence of the proton at the bond formation site produces a lower transition state (1.85 eV) than when the proton is absent (2.58 eV). On

the other hand, the presence of the proton at the binding site implies the formation of a less bound glycine tripeptide conformer (1.39 eV), compared to that formed when the proton is away from the reaction site (0.88 eV).

Figure 43 shows two other reaction paths. They were obtained with another mixed dimer conformer as the starting point, where the proton is initially on glycine. The green pathway is associated with the TS4 transition state and represents a pathway where the proton is distant from the sites where the bond is formed. Note that it participates in the bonding in the structure of the starting conformer and that this bonding, which does not involve the reaction sites, will remain along the path. The glycine tripeptide conformer thus formed is protonated on the terminal nitrogen. The red path associated with the TS5 transition state shows a mechanism where the proton is located at the reaction site. This mechanism is close to that obtained with the protonated glycine dimer. The glycine tripeptide conformer thus formed keeps the proton close to the peptide bond and its energy is higher than for the previous path.

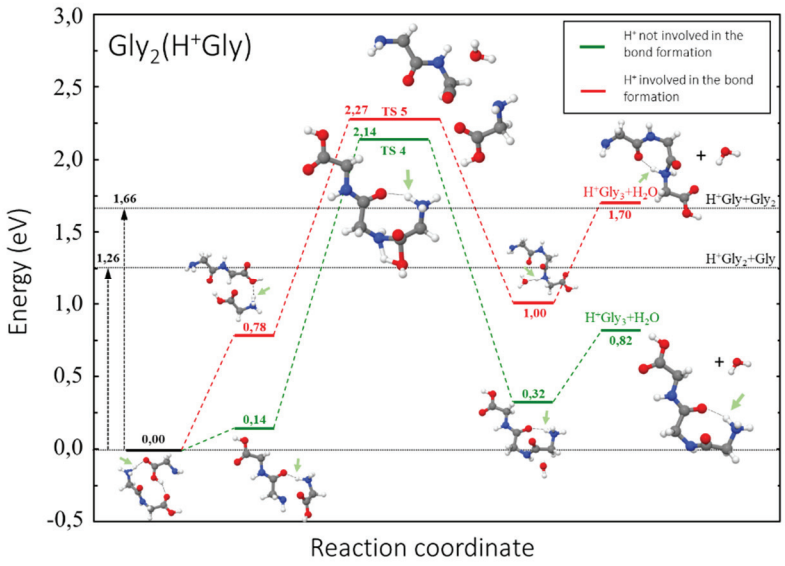

Figure 43: Energy diagram at 0 K calculated in DFT (M06-2X/6-311G++(2df,p)) for the formation of the glycine tripeptide from a mixed glycine cluster, in the case where the proton is on the glycine $Gly_2(H^+Gly)$, with (red) and without (green) the presence of the proton at the peptide bond formation site. The calculated energies include the zero-point energy. The structures associated with the energies are shown in the figure and the green arrow indicates the position of the proton. The energy reference (0 eV) corresponds to the ground state energy of the $H^+Gly_2(Gly)$ cluster. The vertical black arrows indicate the evaporation process of a glycine molecule or a glycine dipeptide molecule from the cluster.

In Figure 43, the barrier for peptide bond formation without direct proton involvement (2.14 eV) is slightly lower than that with direct proton involvement (2.27 eV). This contrasts with the calculations made when the proton is on the glycine dipeptide. Structural analysis shows that the small size of the glycine makes the proton available to create a stabilising bond with the

glycine dipeptide during polymerisation. As with the pathways presented above, these other two pathways also correspond to “concerted” mechanisms, as described by Redondo *et al.* [13].

Two “stepwise” mechanisms have been studied and are presented in Figure 44. One pathway is studied from a starting conformer where the proton is on the glycine dipeptide (blue). This pathway has two transition states, the highest of which is TS9. The mechanism has several steps, one of which (TS8) can be compared to the reaction between neutral molecules described by Redondo et al. while the TS9 step is similar to the reaction between a neutral and a protonated molecule. The glycine tripeptide thus formed is protonated on an oxygen. A second pathway (in pink) is studied with the proton on glycine at the start. The reaction threshold is given by the TS6 transition state. The proton stabilises TS6 by forming a hydrogen bond. The glycine tripeptide formed by this pathway is also protonated on the oxygen.

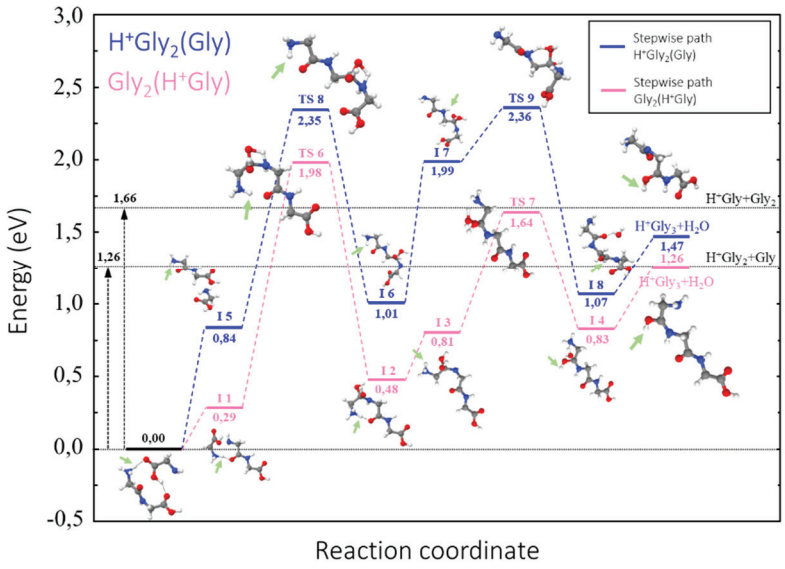

Figure 44: Energy diagram at 0 K calculated in DFT (M06-2X/6-311G++(2df,p)) for the formation of the glycine tripeptide from a mixed glycine cluster via a 'stepwise' pathway with intermediate complex formation and in the case where the proton is on the glycine $Gly_2(H^+Gly)$ (pink) or on the glycine dipeptide $H^+Gly_2(Gly)$ (blue) The calculated energies include the zero-point energy. The structures associated with the energies are shown in the figure and the green arrow indicates the position of the proton. The energy reference (0 eV) corresponds to the ground state energy of the $H^+Gly_2(Gly)$ cluster. The vertical black arrows indicate the evaporation process of a glycine molecule or a glycine dipeptide molecule from the cluster.

In Figure 44, the energy barrier for the path where the proton is initially on the glycine dipeptide is greater (2.36 eV) than when the proton is on glycine (1.98 eV). It can be seen from the structural analysis that this results from the formation of a hydrogen bond by the proton when it is on glycine. Thus, without being directly present at the site of bond formation, it has an influence on the energy of the transition state.

Figure 45 shows the different reaction paths studied in a simplified presentation. For all six mechanisms, we have shown the conformers of the protonated mixed dimer, the transition state that indicates the threshold of the reaction, and the glycine tripeptide conformer formed.

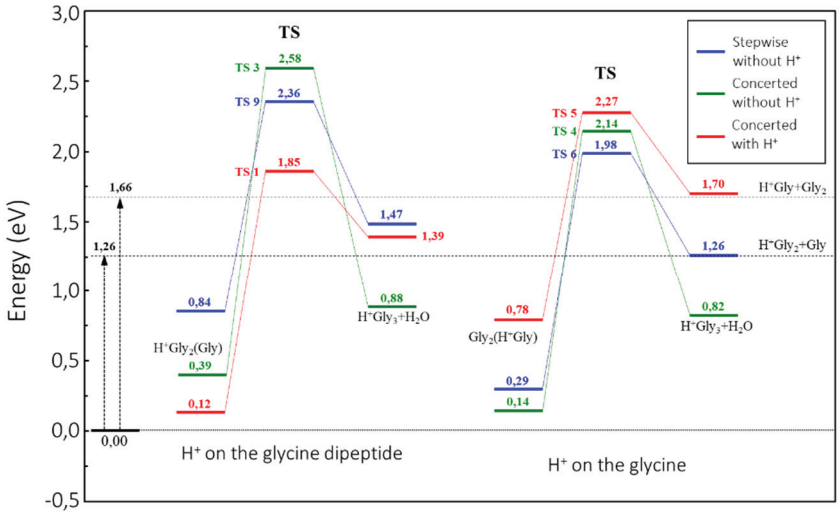

Figure 45: Energy diagram summarising the pathways leading to the formation of the glycine tripeptide in the case where the proton is on the glycine dipeptide during the reaction (left) or on glycine (right). Only the energies of the initial state, transition state, and final state are shown.

When considering these results against the KER measurements, it is necessary to consider the reaction threshold but also the minimum energy of the resulting conformer. Seen in this light, the TS1 pathway has the lowest threshold and the difference in energy between the threshold and that of the conformer formed is the lowest (0.46 eV). This reaction path can produce a distribution with lower KER values than the other paths. As the internal energy in the cluster increases, the other paths compete successively. The difference between the threshold and conformer energy is greater for these other paths (0.57, 0.72, 0.89 eV for TS5, TS6, TS9, respectively) and as the threshold is higher, the associated KER distribution will be shifted towards higher KER values compared to the contribution of the TS1 path. Paths TS4 and TS3 are singled out by the particularly high value between the barrier and the energy of the produced conformer (1.32 and 1.70 eV for TS4 and TS3, respectively). The threshold of the TS3 path is particularly high. This path could compete with the fragmentation of the molecules. However, when compared with the values obtained for methanol, the threshold values and energy difference values of the reaction products obtained here are similar and thus the TS4 and TS3 paths can contribute as can the TS5, TS6 and TS9 paths. The TS1 pathway and this pathway group could be the source of the two contributions observed in the KER distribution.

As with the protonated glycine dimer, the lowest barrier for carrying out the reaction (1.85 eV) is higher than the barrier associated to evaporation of glycine molecule (1.26 eV) and to evaporation of glycine dipeptide (1.66 eV). This is in contrast to the situation with the methanol dimer. Thus, in glycine dimers, evaporation versus reaction competition occurs at lower internal energy values and this could be the reason for the overall higher KER values observed with glycine. However, this qualitative reasoning is based on a PST-like description, based on the complete redistribution of energy in the reactant before the separation of the reaction products. Furthermore, as the size of the molecules increases, the number of conformers and reaction paths increases, which increases the complexity of DFT studies.

Bibliography

[1] G. Bruny, "Production et caractérisation d'agrégats moléculaires protonés contenant un nombre donné de molécules d'eau auprès de dispositif DIAM," Université Claude Bernard Lyon 1, Ph.D. dissertation 2010. [Online]. theses.fr/2010LYO10270

[2] F. Berthias et al., "Proton Migration in Clusters Consisting of Protonated Pyridine Solvated by Water Molecules," *ChemPhysChem*, vol. 16, pp. 3151–3155, September 2015.

[3] T. Salbaing, "Thermalisation dans une nanogoutte : évaporation versus réactivité," Université Claude Bernard Lyon 1, Ph.D. dissertation 2019. [Online]. theses.fr/2019LYSE1163

[4] S. T. Graul and R. R. Squires, "A flowing afterglow-triple quadrupole study of the mechanisms and intermediates in the gas-phase reactions of CH3OH+ with CH3OH," *IJMS*, vol. 81, pp. 183–202, December 1987.

[5] G. Bouchoux and N. Choret, "Reactions between protonated and neutral methanol in the gas-phase: anab initio molecular orbital study," *RCM*, vol. 11, pp. 1799–1807, October 1997.

[6] Yao-Lun Yang et al., "The Perseus ALMA Chemistry Survey (PEACHES). I. The Complex Organic Molecules in Perseus Embedded Protostars," *ApJ*, vol. 910, p. 20, March 2021.

[7] P. Rousseau et al., "Polypeptide formation in clusters of beta-alanine amino acids by single ion impact," *Nat. Commun.*, vol. 11, July 2020.

[8] L. Tiefenthaler, J. Kočišek, and P. Scheier, "Cluster ion polymerization of serine and tryptophan, the water loss channel," *Eur. Phys. J. D*, vol. 74, May 2020.

[9] M. Nihamkin, A. Isaak, A. Albeck, Y. Mastai, and Y. Toker, "Gas Phase Bond Formation in Dipeptide Clusters," *JPCL*, vol. 11, pp. 10100–10105, November 2020.

[10] P. Bertier et al., "Energy Dispersion in Pyridinium-Water Nanodroplets upon Irradiation," *ACS Omega*, vol. 7, pp. 10235–10242, March 2022.

[11] William D. Price, Paul D. Schnier, and Evan R. Williams, "Binding Energies of the Proton-Bound Amino Acid Dimers Gly.Gly, Ala.Ala, Gly.Ala, and Lys.Lys Measured by Blackbody Infrared Radiative Dissociation," *The Journal of Physical Chemistry B*, vol. 101, pp. 664–673, January 1997.

[12] P. B. Armentrout and A. L. Heaton, "Thermodynamics and Mechanisms of Protonated Diglycine Decomposition: A Guided Ion Beam Study," *JASMS*, vol. 23, pp. 632–643, August 2011.

[13] P. Redondo, H. Martínez, Á. Cimas, C. Barrientos, and A. Largo, "Computational study of peptide bond formation in the gas phase through ion–molecule reactions," *PCCP*, 2013.

[14] J. P. Merrick, D. Moran, and L. Radom, "An Evaluation of Harmonic Vibrational Frequency Scale Factors," *JPCA*, 2007.

[15] B. Paizs, I. P. Csonka, G. Lendvay, and S. Suhai, "Proton mobility in protonated glycylglycine and N-formylglycylglycinamide: a combined quantum chemical and RKKM study," *RCM*, 2001.

General conclusion

The molecular cluster irradiation device (*Dispositif d'Irradiation d'Agrégats Moléculaires* – DIAM) of the IP2I in Lyon allows to statistically observe the post-collisional relaxation of molecular clusters previously selected in mass and energy. A single high-speed collision allows to quantitatively observe the consequences of the energy redistribution in small clusters. The deposition of energy during the collision takes place over a short time (a few femtoseconds) compared to the dynamics of the nuclei. The energy is deposited in the cluster by electronic excitation and thus the energy deposition is localized in one of the molecules of the cluster. This type of energy deposition, characteristic of irradiation by electromagnetic radiation or by interaction with a fast and charged particle, occurs in many fields. This situation is different from the activation of a chemical reaction in liquid phase by temperature rise. Indeed, in liquid phase, the internal energy of the molecules is modified progressively by a succession of collisions. Here, the energy is deposited over a short time in one of the molecules of the cluster, placing it suddenly in a situation far from equilibrium. The dynamics in the presence of excess internal energy has both quantum and statistical aspects. The different ways of redistributing energy in these small molecular clusters are involved in the competition between the different relaxation channels: evaporation of a molecule, fragmentation of a molecule, and reactivity between molecules.

The pyridine dimer $H^+(Pyr)_2$, studied here, is an example of an organic molecules dimer for which there is no reactivity between the molecules. The study of the multiparametric data set obtained with the COINTOF VMI method, allowed the determination of the branching ratios between the three relaxation processes observed after fragment analysis, 262 ns after collisional excitation: evaporation without fragmentation, fragmentation of the pyridinium ion and fragmentation of the neutral molecule. The evaporation without fragmentation, i.e. the pyridine molecule and the pyridinium ion remain intact, represents 14% of the observed events. The fragmentation of the pyridinium ion represents 30%, and the fragmentation of the neutral molecule 56%. During the fragmentation of the H^+Pyr molecular ion, the production of the $C_4H_4H^+$ ion represents 46% of the events, that of $C_3H_3^+$ corresponds to 31% of the events, $HCNH^+$ corresponds to 20%, CH^+ to 3%, and H^+ to less than 1%. It should be noted that the H^+ proton is observed in 0.1% of all the events and the analysis of the spectra shows that, in this case, the two pyridine molecules are not fragmented.

The study of the post-collisional relaxation of the protonated methanol dimer $H^+(CH_3OH)_2$ highlights the competition between the evaporation of a methanol molecule and the unimolecular reaction of dimethyl ether formation. The experiment allowed the measurement of branching ratios between the three competing processes: the evaporation of a methanol molecule

and the two mechanisms identified by Density Functional Theory (DFT) for the water elimination reaction. A Monte-Carlo simulation was developed to quantify the competition between these different relaxation channels based on Phase Space Theory (PST). Comparison of the experimental results — branching ratios and Kinetic Energy Release (KER) distributions — with those of the simulation shows a significant disagreement for the branching ratios. However, the KER distributions produce absolute mean values and shifts between the distributions, close to the experimental values. The model was fitted to the experimental results by changing only the values of the time constants. Good agreement with the experimental results is obtained and the difference between the calculated and measured velocity distributions shows the high velocity evaporation process, that is observed for protonated methanol clusters containing a larger number of molecules.

These results show that the theoretical description is constrained by the measurement of branching ratios and KER distributions for each channel, upon relaxation of the cluster within a fixed time window, after excitation by a single high-speed collision. It appears that the PST model, associated with the complete redistribution of energy before dissociation, cannot fit; but a global shift of the time constants gives a good agreement with the experimental data. The specific consideration of the energy transfer time between the molecules of the cluster could be considered. The results obtained by this simple model, fitted to the experimental results, are a step towards the implementation of models that can be integrated in multiscale models describing diluted media under irradiation. Notably, in the astrophysical context, the presence of methanol and dimethyl ether have been observed in a correlated manner in several star-forming regions. The observation of two young stars located in the star-forming region LH1 120-N 113 in the Large Magellanic Cloud by the ALMA radio telescopes reveals the presence of methanol CH_3OH and dimethyl ether CH_3OCH_3. In our galaxy, the presence of methanol has been observed in 56% of the protostars located in the Perseus molecular cloud.

The study of post-collisional relaxation in pure glycine $H^+(Gly)_2$ clusters and in mixed glycine $H^+Gly_2(Gly)$ clusters allowed the evidence of glycine dipeptide formation on the one hand, and of peptide chain elongation on the other hand. As observed with methanol, the COINTOF VMI method allows the identification of the reaction channel by correlated detection of the two reaction products, the neutral and the charged, after selection in mass and energy of the parent cluster. The measured distributions are very well fitted by the sum of two Maxwell-Boltzmann distributions, leading to studies of the transition states for the water elimination reaction in the protonated glycine dimer and in the mixed dimer. The results of these studies show the presence of several mechanisms in which the proton is involved in different ways. The development of the statistical model to describe the competition between several reaction pathways could allow for a quantitative link between the DFT results and the KER distribution measurements.

All of these studies, developed around protonated molecular clusters and in particular around glycine clusters, show that glycine dipeptide formation and peptide chain elongation are observed in a unimolecular reaction that constitutes a new pathway for peptide chain formation under abiotic conditions. This result, together with the marked abundance of production of the mixed dipeptide and glycine cluster, shows that tripeptide formation is favoured over dipeptide production alone by unimolecular reaction in a small protonated cluster.

Recent observations show a linear correlation between the abundance of different molecules observed on the one hand with ALMA in a hot core and on the other hand with Rosina at the comet 67P/ChuryumovGerasimenko. Glycine is observed on the surface of the comet and the correlation of abundances shows that the presence of glycine in the hot core is not excluded by the current spectroscopic measurements. Advances in astrochemical modeling and observations of molecular clouds and star-forming regions have revealed similar molecular abundances for several complex molecules to those observed in comets, suggesting a similar origin. Molecular dimer formation is a binary process, like the collisions between atoms that constitute one of the elements of our current knowledge of molecule formation in the gas phase. The formation of molecular dimers, an essential step in the cooling process, is favoured by the presence of protons. The unimolecular reaction highlighted in this work appears to be an abiotic pathway that can contribute to the formation of peptide chains under astrophysical conditions.